Plant Derived Cellulose Scaffolds as a Novel Biomaterial for 3D Cell Culture and Tissue Regeneration

Daniel Modulevsky

A thesis submitted in partial fulfillment of the requirements for the
Doctorate in Philosophy degree in Biology

Supervisor: Dr. Andrew Pelling

Department of Biology
Faculty of Science
University of Ottawa

Abstract

This work presents an alternative approach to the production of cellulose-based biomaterials. Instead of extracting, processing and regenerating plant and or bacteria-derived cellulose into a biomaterial, my work established a decellularization protocol to remove cellular plant content from plant tissue resulting in a scaffold composed of cellulose with the evolved architecture of the plant cell wall. Tracheophyte plants, including clubmosses, horsetails, and ferns, gymnosperms and angiosperms, have evolved distinct vascular structures that support the transport of water and nutrients in xylem and phloem that form the vascular bundles (VBs)[1]. This thesis took it's inspiration from the dense, linearly arranged, parallel microchannels which include (VBs) in the stalks of *Asparagus officinalis* possess an architecture with striking similarities to biomaterial scaffolds intended to repair damaged tissue. My work demonstrated that the plant cell wall contains many of the ideal characteristics of a medical biomaterial. The scaffold is biocompatible with mammalian cells and maintains high viability even with cell densities comparable to commercially available scaffolds. The cellulose scaffold could be biochemically functionalized or cross-linked to control the scaffolds' surface biochemistry and mechanical properties. My *in vivo* model demonstrated that the lignocellulose scaffold did not elicit a foreign body response. The scaffold was permissive to host cell invasion, including active host fibroblast, leading to the deposition of host collagen extracellular matrix. Importantly, active blood vessels formed within the scaffold to support the population of host cells. The scaffold retained much of its original shape and provided an inert, pro-vascular long-term environment for host cells to invade. Taken together, this led to the hypothesis that the innate plant cell wall architecture could restore the function of injured tissue, specifically that the vascular bundles could be used to promote axonal regeneration in spinal cord injuries. Rats with complete spinal cord transection were implanted with cellulose scaffolds with

vascular bundles. Animals that received plant-derived scaffolds demonstrated a significant improvement in motor function. This thesis defines a novel and parallel route for exploiting naturally occurring plant microarchitectures of the underlying crystalline cellulose scaffold.

Statement of Originality

The work presented here is entirely original and describes applying plant cell wall architecture to develop novel approaches to mammalian cell culture and treat specific human pathologies. This research and corresponding manuscripts were done under the supervision of Dr. Andrew E Pelling. Dr. Pelling is cross-appointed in both the Departments of Physics and Biology at the University of Ottawa. This thesis consists of three experimental research manuscripts (Chapters 2-4) that have been published and submitted to peer-reviewed scientific journals. The co-authors' contributions are highlighted at the start of each chapter with the motivation, hypothesis, and objective. Chapter 5 discusses the possible future direction of this work, and Finally, the appendix, chapter 6, outlines the surgical and microscopy protocols that had to be established in this thesis.

Manuscripts included in this thesis:

- Modulevsky, D. J., Lefebvre, C., Haase, K., Al-Rekabi, Z., & Pelling, A. E. (2014). Apple Derived Cellulose Scaffolds for 3D Mammalian Cell Culture. *PLoS ONE*, *9*(5)
- Modulevsky, D. J., Cuerrier, C. M., & Pelling, A. E. (2016). Biocompatibility of Subcutaneously Implanted Plant-Derived Cellulose Biomaterials. *PLoS ONE*, *11*(6),
- Modulevsky, D. J., Cuerrier, C.M., Leblanc, M.L,Hickey, R.J, , Obhi, R.J., Shore, I, Galuta, A Walker[5], K., Tsai, E.C., & Pelling, A.E. (2020) Plant Scaffolds Support Motor Recovery and Regeneration in Rat Spinal Cord Injury

This work has also been presented at the following conferences and workshops:

- Modulevsky, D.J., et al. Apple Derived Cellulose Scaffolds for 3D Mammalian Cell Culture, Ottawa Carleton Institute of Biology, Ottawa, Ontario, May, 2015.
- Modulevsky, D.J., et al Apple Derived Cellulose Scaffolds for 3D Mammalian Cell Culture. Cell Dynamic workshop, Elmhirst, Ontario, May, 2014.

Statement of Contributions

I, Daniel Modulevsky, contributed to the majority of the work presented in this thesis. I established the protocols used to decellularize plant tissue for mammalian cell culture (in vitro), implantable biomaterial (in vivo), and the development of plant-based biomaterials with vascular bundle channels use of complete transection spinal cord injury model. Additionally, I did the vast majority of the experimental work within the research projects; cell culture, confocal microscopy, brightfield slide scanning, animal surgeries subcutaneous, spinal cord transection, tracer transections, animal care, image and data analysis, and participated in the writing of the scientific manuscripts presented in this thesis.

Other Contributions

While completing the Ph.D. thesis work, I also participated in the work and preparation of several other first author publications and contributed to research conducted by other Pelling Lab colleagues; additionally, this manuscript's work led to the submission of an international patent. All contributions to other manuscripts and patent details are listed below. The work outlined in this thesis also lead to the founding of biomaterial startup Spiderwort Inc, with Dr. Charles Cuerrier and Dr. Andrew E. Pelling.

Contributions to other manuscripts (not presented in this thesis):

- Hickey, R. J., Modulevsky, D. J., Cuerrier, C. M., & Pelling, A. E. (2018). Customizing the Shape and Microenvironment Biochemistry of Biocompatible Macroscopic Plant-Derived Cellulose Scaffolds. *ACS Biomaterials Science & Engineering*, *4*(11)

- WhiteFeather H, Modulevsky DJ, Pelling AE. Silk Textile Weaving for Mammalian cell culture (In preparation)

- Modulevsky DJ, Cuerrier CM, Pelling AE. Open Source Biomaterials for regenerative Medicine, Biocoder.2015

- Modulevsky DJ, Cuerrier CM, Pelling AE. DIY Open Source Biomaterials, Biocoder. 2015

- Modulevsky DJ, Haase K, Bukoreshtliev NV, Pelling AE. Calcium Release Response in Epithelial HeLa cells to Local Nanomechanical Shear Stress Delivered by an AFM Tip, Cytoskeleton (in preparation)

- Modulevsky, D. J., Tremblay, D., Gullekson, C., Bukoresthliev, N. V, & Pelling, A. E. (2012). The Physical Interaction of Myoblasts with the Microenvironment during Remodeling of the Cytoarchitecture. *PloS One*, *7*(9),

Contribution to patents:

- Pelling, A. E., Cuerrier, C. M., Modulevsky, D. J. & Hickey, R. J. Decellularised cell wall structures from plants and fungus and use thereof as scaffold materials. *PCT Int. Appl.* 143pp. (2017).

Acknowledgments

I want to thank Dr. Andrew Pelling and Dr. Charles Cuerrier for their contribution to this thesis; if not for their mentorship, consideration, support and empathy, I would not have gotten to this point. Dr. Eve Tsai was instrumental in developing the protocols needed in my thesis's final research chapter and the histological data interpretations. I would also like to thank Dr. Kristina Haase, Dr. Delphine Gourdon, Dr. Bela Joos, Dr. Tuan Bui, Dr. Vance Trudeau and Dr. Sean Kennedy for their support and help throughout my Ph.D. I would also like to thank all my fellow Pelling lab students, both past and present, who have put up with me in the lab and the office.

A very special thank you to my family, Yury, Irene, Isaac, Mira and Ilana, who would never fail to ask when I would be done and why it was taking this long.

To Meghan: Thank you for the support and kindness. When we first met, I told you I was pretty much done with my Ph.D.- today, that almost becomes true. I cannot wait to spend the rest of my life with you

List of Abbreviations

AFM	Atomic Force Microscopy
ATCC	American Type Culture Collection
BBB	Basso, Beattie, Bresnahan Locomotor Rating Scale
BC	Before Christ
BDNF	Brain-Derived Neurotrophic Factor
CAM	Cellular Adhesion Molecule
CPD	Critical Point Dryer
CNS	Central Nervous System
CNTF	Ciliary Neurotrophic Factor
Coll	Collagen
CTRL	Control
DAPI	4',6-Diamidino-2-Phenylindole,fluorescent nuclear stain
DMEM	Dulbecco's Modified Eagle Medium
DNA	Deoxyribonucleic Acid
DP	Degree of Polymerization
ECM	Extracellular Matrix
EM	Electron Microscopy
FA	Focal Adhesion
FAK	Focal Adhesion Kinase
FBR	Foreign Body Response
FDA	Food and Drug Administration
FG	Fluorogold
GA	Glutaraldehyde
GFAP	Glial Fibrillary Acidic Protein
GDNF	Glial cell Derived Neurotrophic Factor
HA	Hydroxyapatite
HBSS	Hank's Balanced Salt Solution

HCL	Hydrochloric acid
HEMA	2-Hydroxyethyl Methacrylate
HEPES	Hydroxyethyl Piperazineethanesulfonic acid
IGF	Insulin Growth Factor
IP	Intraperitoneal Injection
MMPs	Matrix Metalloproteinases
MRI	Magnetic Resonance Imaging
MSC	Mesenchymal stem cells
NGF	Nerve Growth Factor
NSC	Neural Stem Cell
PBS	Phosphate Buffered Solution
PDMS	Polydimethylsiloxane
PFA	Paraformaldehyde
PEG	Poly(ethylene Glycol)
PGA	Polyglycolic Acid
PI	Propidium Iodide
PKC	Protein Kinase C
PLGA	Poly(lactic-co-glycolic)
PMN	Polymorphonuclear
RBC	Red Blood Cells
RGD	Arginine(R)-Glycine(G)-Aspartic acid(D)
ROI	Region of Interest
ROCK	Rho-associated Protein Kinase
RPM	Rotation Per Minute
RPTP-α	Protein-Tyrosine Phosphatase alpha
SC	Scaffold
SCI	Spinal Cord Injury
SDS	Sodium Dodecyl Sulfate

SEM	Scanning Electron Microscopy
USD	United State Dollars
UTI	Urinary Tract Information
UV	Ultraviolet
WGA	Wheat Germ Agglutinin
WWII	World War two
VBs	Vascular Bundles

LIST OF FIGURE AND TABLES

TABLE OF CONTENTS

Introduction to biomaterials emergence of plant-based biomaterials

Daniel J. Modulevsky

1.1 Forward and General Introduction

A biomaterial is a material designed to interact with a biological system for either medical intervention or body augmentation[2]. In comparison, a biological material is of natural origin produced from plant or animal[2]. The two interrelated fields of study are distinct: the field of biological materials studies the evolved and adaptive mechanisms and architecture that allow it to perform its intended function, whereas the field of biomaterial science works to create material scaffolds that mimic biological tissues 'desirable characteristics with the goal of, ultimately, replacing the damaged tissue. This thesis presents a novel parallel approach that combines elements from both fields, demonstrating how plant-derived biological material with their underlying architectural and micro-structures can be adapted to create biomaterials with extended use in tissue engineering applications.

This work presents an alternative approach to the production of cellulose biomaterials. Instead of extracting and regenerating plant cellulose, we decellularized plant tissue and used the natural lignocellulose form combined with the plant cell wall's organic architecture. In attempting to create a novel scaffold that better mimics an *in vivo* environment for *in vitro* research, this work demonstrated that the plant cell wall contains many engineered medical biomaterials' ideal characteristics. Here we successfully demonstrated that apple-derived crystalline cellulose is biocompatible with mammalian cells and can maintain high viability, even after 12 continuous weeks of culture, and achieved cell densities comparable with other natural and synthetic scaffold materials[3,4].

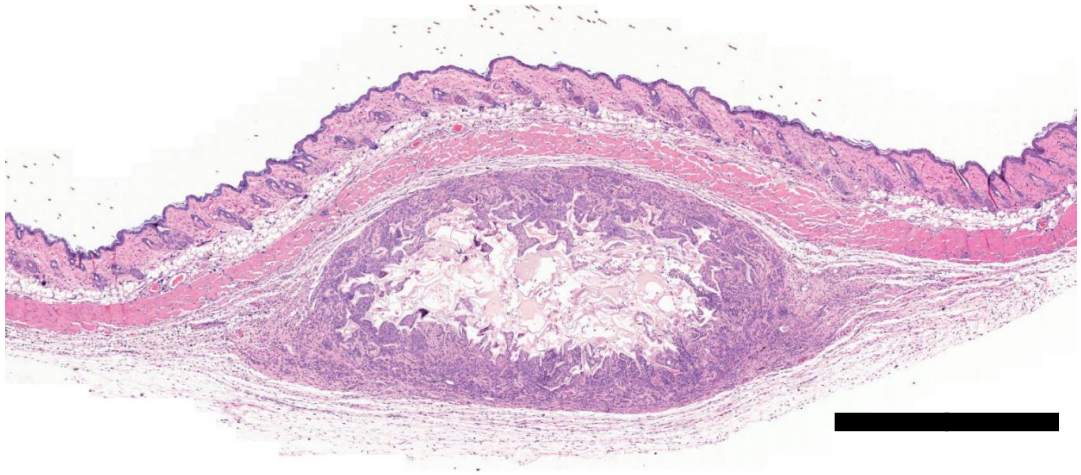

Figure 1.1. Subcutaneous implanted decellularized cellulose apple scaffolds Apple derived scaffolds implanted under the skin of mice for 1 week. The scaffold was sectioned and stained with H&E; nuclei are dark purple. Low latent acute and chronic inflammation are observed following 1 week of implantation surgery. Cell infiltration are migrating towards the apple scaffold's interior Scale bar = 1000 µm

In addition, biochemical functionalization or chemical cross-linking can control the scaffold's surface biochemistry and mechanical properties to provide researchers with a comparable biomaterial that is quickly produced, inexpensive and originates from a renewable source. In the *in vivo* model, the apple-derived scaffold did not elicit a significant foreign body response (FBR) in the surrounding dermis tissue, ultimately leading to stable implantation as with First-Generation biomaterials. The biomaterial was observed to have active fibroblast migration within the cellulose scaffold; this was simultaneous with a new collagen extracellular matrix deposition. Importantly, active blood vessel formation within the scaffold was observed throughout the biomaterial, together as early as 4 weeks. (Figure 1.1).

Furthermore, the scaffold retained much of its original shape, even after 8-week implantation, and therefore capable of providing a stable long-term environment to restore injured tissue function. The apple-derived cellulose scaffold appeared as an extension to the native tissue that had yet to be invaded with host cells (Figure 1.1).

Like more advanced Second-Generation biomaterials, the plant-derived biomaterials achieved host integration but did not have to degrade into harmful oxidative by-products, such as lactic acid and or glycolic acid within implanted PLGA scaffolds have caused further damage to the already prone-to-injury tissue post-injury or surgery[5]. Finally, we demonstrated that scaffolds containing vascular bundles (VBs), a microscale channel tasked in the plant to transport water and nutrients, could support neuro-regeneration in a spinal cord injury (SCI) rat model. Rats were implanted with scaffolds containing VBs with a complete spinal cord transection at the T8-T9 vertebrae. Over six months, animals that received plant-derived scaffolds alone, with no therapeutic stem cells, growth factors, pharmaceuticals, or electrical stimulation, demonstrated a significant motor function improvement. Together, the work defines an entirely novel route for exploiting naturally occurring

plant microarchitectures to promote motor recovery and the regeneration of functional spinal cord tissues. The work done in this thesis has inspired labs worldwide to develop similar techniques to develop their plant-based biomaterials and methodologies that can further promote this new field of biomaterials and novel cellular meat industry [6–13].

1.2 History of Biomaterials

The use of plant tissue as biomaterials in humans dates back to 3000 BC. Historians and archeologists have uncovered evidence that ancient Egyptian physicians used coconut shells to repair fractures and defects in patient skulls[14]. From antiquity to the industrial revolution of the 19th century, plant biomaterials have routinely been the material of choice to fabricate external prosthetics[15]. The priority was on materials that could withstand the physical requirements of the external replaced tissue. For example, wood prosthetics replaced bone and ivory or gold replaced teeth[15,16]. With a lack of anesthetics limiting the complexity of surgeries that could be conducted, little attention was given to the use of internal biomaterials. The field of biomaterials experienced a shift in the 20th century with the foundation of material science. It was then that researchers first began looking at the biomaterials' internal microarchitecture to understand the importance of biomaterial-tissue interface at the cellular level[15].

1.2.1 First-generation of biomaterials

The first scientific breakthrough in the field of biomaterials was during World War II when army surgeon and ophthalmologist Dr. Harold Ridley treated a pilot whose aircraft canopy was hit with machine-gun fire, sending polymethacrylate shards into his eyes. Dr. Ridley discovered that acrylic shards did not affect the pilot’s vision, and surprisingly, there was no host response to the synthetic foreign material lodged into his eyes. That lead Dr. Ridley to develop the first artificial intraocular

lens to replace a patient's entire natural lens in 1950 [17,18]. After finally being approved by the U.S Food and Drug Administration (FDA) in 1981, intraocular lens replacement became one of the most common surgeries worldwide[19]

Several other unique internal biomaterials were developed with the emergence of the material science field, creating the foundation for the first generation of internal prostheses sourced from various biomaterials in the 1960s to 1980s [20]. The underlying principle of these first-generation biomaterials was to reduce the host's biological response to the foreign material to create bioinert scaffolds. The hypothesis was that a biomaterial that did not elicit a chronic FBR would not form the fibrous capsule between the implanted biomaterial and the host, which ultimately results in implant failure and the rejection of the biomaterial[20]. The first generation of biomaterials was synthesized of the highest quality pure material to limit corrosion and toxin within the patient. Nonetheless, long-term implantation of such biomaterials would ultimately lead to excessive absorption of host proteins and eventually implant failure, leaving patients prone to severe infection and, in the most severe cases, necessitate additional surgery to remove the failed implant.

1.2.2 Foreign Body Response to Biomaterials

FBR is an immunologic reaction to a biomaterial characterized by chronic inflammation, foreign body giant cell formation and the final stage of fibrotic capsule formation around the implanted biomaterial. FBR was particularly evident in the first generation of biomaterials which led the researcher to develop the second generation of biomaterials to overcome FBR through host degradation and surface modifications. FBR is initially the mammalian wound healing response whose progress is interrupted by a non-degradable biomaterial within the active injury wound. Typically, an injury severe enough to cause bleeding would trigger a cellular cascade, activate inflammation, and initiate the wound healing response. Wound healing occurs through overlapping

phases of inflammation, vascular proliferation and finally, tissue remodelling through the deposition of granulation tissue and scar formation. When implanting a biomaterial, a wound is created that results in host bleeding. The bleeding will result in the deposition of blood proteins and thrombotic agents onto the biomaterial's surface. This process of blood agents absorbing onto the biomaterial to form a provisional matrix around the biomaterial is biofouling[21]. The provisional matrix comprises the elements found within blood serum and contains fibrinogen, chemokines and cytokines, activated platelets, inflammatory cells, and endothelial cells[21]. Fibrinogen is a glycoprotein complex that constitutes within the blood. Tissue injury causes thrombin to enzymatically converted fibrinogen into the active fibrin form. Fibrin molecules then can self-adhere to form a blood blot that occludes bleeding[22] The accumulation of fibrinogen onto the biomaterial surface recruits inflammatory cells and the phagocytes to the biomaterial[21]. The platelets and thrombolytic agents on the absorbed provisional matrix further recruit macrophage cells to the biomaterial's perimeter through the release of transforming growth factors (transforming growth factor-β, platelet-derived growth factor, chemokine ligand 4, leukotriene, and interleukin-1). The macrophage within the scaffold further recruits surrounding macrophages within the host tissue and blood via chemotactic cytokines' secretion. Phagocytic cells are recruited to the implant site through the release of C3b from the provisional matrix. Macrophages surrounding the provisional matrix migrate into the provisional matrix/biomaterial through adherence via phagocyte surface integrins; Mac-1 (CD11b/CD18); fibrinogen ligands. immunoglobulin G, and iC3b[21]. Activated macrophages have two phenotypes M1 or M2. The M1 pro-inflammatory phenotype is associated with pathogen clearing and enhanced endocytosis. In contrast, the M2 anti-inflammatory is characterized by the resolution of the inflammatory process and suppression of intracellular killing capabilities and reduced antigen uptake[21]. The distribution

of M1 and M2 macrophages throughout the biomaterial interface distinguishes between proinflammatory response and noninflammatory response[21]. Activated macrophages within the provisional matrix will begin to fuse into foreign body giant cells when they can not absorb the entire biomaterial via phagocytosis. The macrophages become frustrated and begin fusing with other macrophages to create giant cells. The giant cells release reactive species in an attempt to break down the foreign material. As with macrophages, the foreign body giant cells secrete inflammatory cytokines , TGF- β1, that promote the activation of fibroblasts to deposit a layer of collagen around the foreign biomaterial to create a fibrotic capsule in an attempt to isolate the material from the host[21]. Together, macrophages and foreign body giant cells secrete cytokines and proteolytic enzymes that influence the forming fibrotic capsule's activity. Matrix metalloproteinases (MMPs) have been shown to degrade the ECM components and been shown as a regulator of post wound angiogenesis and fibrosis[21].

Within implantable biomaterial, the fibrotic capsule is functional to stabilize the implant to the injury site to limit the implant's movement. However, excessive fibrosis can lead to implant failure through implant deformity and implant extrusion in the most severe cases[21]. The adaption of biomaterials to FBR leads to the foundation of the second generation of biomaterials.

1.3 The second generation of biomaterials

Researchers sought to eliminate the risk of implant failure and multiple surgeries by developing biomaterials that decompose within the implanted host[20]. This new generation of biomaterials were designed to contain a three-dimensional structure that promoted host cell integration[23]. The second generation of biomaterials' driving hypothesis was that the material would slowly degrade to be

replaced with host tissue, mitigating the risk of secondary surgeries, and the host phagocyte cells would clear any by-product fragments[20]. This generation of biomaterials was developed to be bioactive to facilitate decomposition and minimize the actual footprint of the biomaterial[20]. Unfortunately, biomaterials such as PLGA constant release of by-products lactic acid and glycolic acid have caused further damage to the already prone-to-injury tissue post-injury or surgery by lowering the local pH levels and further inducing an inflammatory response[5]. Additionally, lower pH levels hasten the polymer's degradation, which ultimately leads to the premature mechanical failure of the biomaterial[5].

1.3.1 Dawn of Modern Era (Designed Biomaterials)

From 1935-1978, researchers focused on producing synthetic biomaterials with specific characteristics to replace the naturally derived biomaterials[24]. The synthetic polymers defined in this era of biomaterials saw the formation of synthetic polymers, silicones, ceramics, hydrogels, metal alloys, polyurethanes, teflon, poly(Ethylene Glycol), poly(Lactic-Glycolic acid), hydroxyapatite, titanium and bioglass[24].

1.3.2 Silicones

Silicones have been used in the medical field for over 60 years and are employed in many different medical applications due to several desirable chemical and physical properties, including stability, low surface tension, and general lack of toxicity[25]. (Figure 1.2a) Silicone polymers can be conjugated with various pharmaceuticals and used as a vector to deliver the active ingredients to the injury site. However, as with other hydrophobic biomaterials, silicone surfaces become coated with serum proteins when in contact with tissue serum. This coating of serum proteins initiates

many signals that ultimately lead to FBR scar encapsulation surrounding the implant before rejection [21,25].

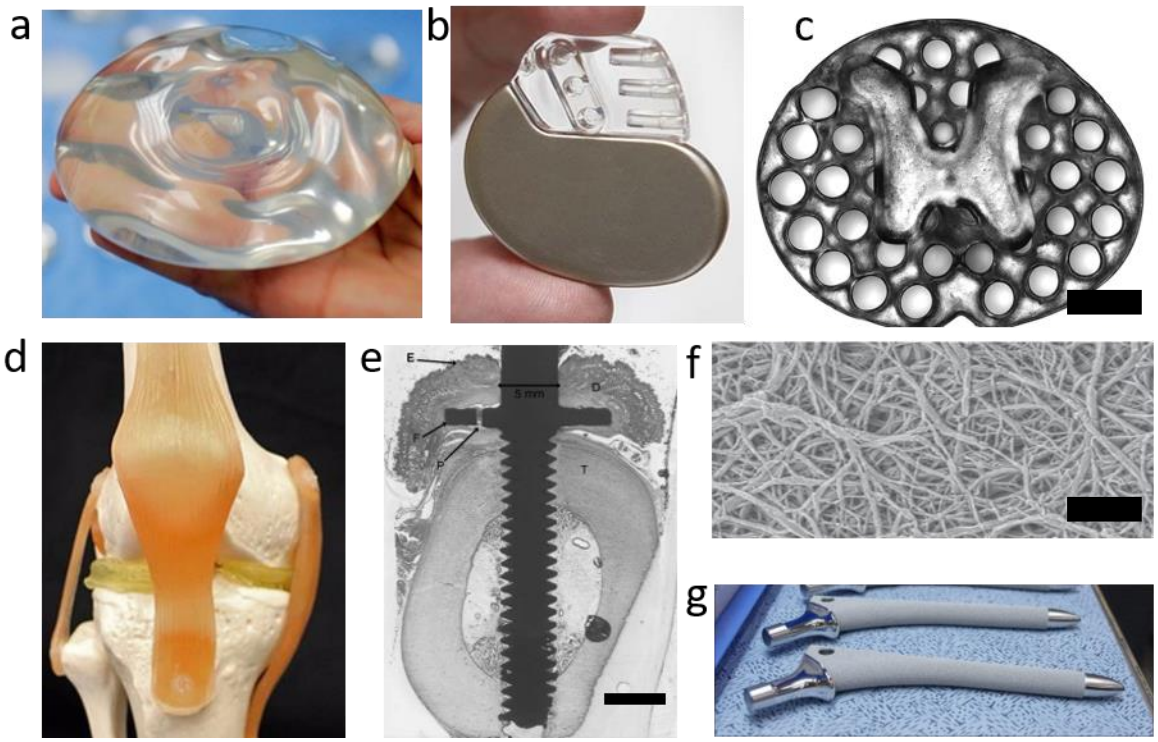

Figure 1.2 Various biomaterials and their intended medical applications. a) Silicone gel breast implants before implantation b) Polyurethane in a Lubrizol cardiac pacemaker c) Microscale continuous projection printing of PEG spinal cord scaffolds for rats[26]. (Scale bar = 0.5 mm) d) Hydrogel derivative used to create cartilage-mimicking material[27] e) Titanium bone implants with Hydroxyapatite surface treatment. (Scale bar = 5mm) f) Poly(Lactic-Glycolic Acid) nanoporous composite used in bone tissue scaffolds. (Scale bar = 5 µm) g) Bioglass surface medication to femur implants.

1.3.3 Polyurethanes

Polyurethanes were first synthesized in the 1930s by Du Pont and are still used as biomaterials in various medical devices in contact with blood, including; pacemakers and artificial hearts [28] (Figure 1.2 b). Polyurethane's mechanical properties, including the resistance to fluid shear and biocompatibility, are why polyurethanes are the material of choice for applications under constant shear and contact with blood flow[28].

1.3.4 Teflon

As with polyurethanes, Teflon originated in the DuPont labs by husband and wife scientists William and Genevieve Gore. When Teflon was heated and stretched, the biomaterial formed a porous membrane that was thought to be ideal for the vascular prosthesis. Like many other ideas for biomaterial applications, the idea for Teflon's initial medical use originated by chance. Reportedly, William Gore got the idea from conversing with a physician while riding a ski lift together on vacation[29].

1.3.5 Hydrogels

Hydrogels are derivatives of their natural forms found within bacterial biofilms, hydrated extracellular matrices (ECM), and plant structures[30] (Figure 1.2 d). Hydrogels are a three-dimensional network of chemically or physically cross-linked hydrophilic polymers with H_2O contributing to at least 10% of the total weight[31]. In 1960, DuPont researchers Wichterle and Lim published a paper in Nature that described a technique to polymerize HEMA monomer hydrated with water and a cross-linker. Wichterle created a device (out of the toy Mechanix) that could cast the hydrogel into soft contact lens prototypes[29].

1.3.6 Poly(Ethylene Glycol)

Poly(Ethylene Glycol) (PEG) was first discovered as a potential inert vehicle for controlled intravenous injections of fat-soluble hormones[29]. Dr. Frank Davis noticed that pharmaceutical recombinant enzymes loaded with hydrophobic PEG protein polymers elicit a lower FBR response within the host, allowing for a longer active pharmaceutical lifespan of the enzyme.[32] The biocompatibility and customization of PEG have led to various techniques ranging from dermal implants to spinal cord repair (Figure 1.2 c). It has received extensive attention from researchers leading to a multitude of research published on PEG[26,33–55].

1.3.7 Poly(Lactic-Glycolic Acid)

Poly(Lactic-Glycolic Acid) (PLGA) was first designed to be a monomer to mimic Dacron textiles' mechanical properties. PLGA was first developed as a medical suture as PLGA demonstrated biocompatibility and slow degradation within host[56]. Since then, PLGA has been FDA approved to be used within a broad array of medical applications, including drug delivery, diagnostics, vaccines, bone tissue engineering, and *in vitro* as 3D tissue culture scaffolds for cardiovascular and cancer models disease[57] (Figure 1.2 f). Recently, PLGA has been adapted for nanotechnology in medicine-related applications. Its fine-degradation properties are ideal for releasing pharmaceuticals, proteins, and imaging compounds[57]

1.3.8 Hydroxyapatite

Hydroxyapatite (HA) is a naturally occurring biomaterial that accounts for 50- 70 % of the bone's mineral components. As with other biological biomaterials, HA can be both synthetically produced or extracted from a natural source[58]. HA is an additive coating to biomaterial implants that interact with bones to ensure stable integration of the biomaterial[58]. HA itself has not been utilized in load-bearing applications as pure HA in crystalline form does not contain the mechanical properties required for load-bearing devices[58] (Figure 1.2 e).

1.3.9 Titanium

The science of the synthesis and manufacturing of titanium was accelerated to meet the increasing demands for metals during WWII. Due to its load-bearing properties, Titanium was used as an implant to treat bone defects and injuries[29]. The use of titanium for bone implants precipitated the need to understand the mechanisms of what was later coined osseointegration by Dr. Branemark. His works were the first to establish the need for a stable integration between the material and bone that ultimately determined a bone biomaterial[29] (Figure 1.2 e).

1.3.10 Bioglass

Bioglass, as with titanium, also owes its existence to the military complex of WWII. Dr. Larry Hench was investigating the interaction of glass materials when exposed to nuclear radiation. A chance encounter during a conference triggered Dr. Hench and his team to modify silicate-based glass to have higher calcium and phosphorus levels needed for bone integration. The Bioglass samples were sent to an orthopedical surgeon, who then implanted them on rat femurs. Six weeks later, the Bioglass was integrated with the bone to a point where the surgeon could not remove the silicate glass from the femur[29] (Figure 1.2 g).

1.4 Modern Era of Biomaterials

As we highlighted in the previous section, the first-generation biomaterials had a robust function-only approach during the initial development of biomaterials. The researchers' goal was to replace the displaced tissue's functionality within the host with little understanding of the importance of the surrounding host's response to the biomaterial. This function's first approach is understandable as the researchers worked on the bleeding edge and developed the foundations of biomaterial science. This first wave of biomaterials coincided with the emergence of material science, and as such, the vast majority of first-generation biomaterials were developed from existing industrial materials. In the following sections, I will outline the emergence of the second and modern generation of biomaterials that were designed to elicit a controlled response within the injured tissue to achieve a desired therapeutic effect, as researchers started to develop biomaterials with customizable degradable properties. A degradable biomaterial allowed researchers to create a temporary host tissue interface that facilitated foreign biomaterial to be degraded into byproducts. Researchers began to modify degradable biomaterials to enhance needed properties such as strength and flexibility. The degree of programmable control over the biomaterials allowed researchers to use the emerging biomaterials to introduce pharmacological molecules for controlled drug delivery and gene therapy. Additionally, researchers decided to design the biomaterials' chemical composition to best comply with the intended replacement tissue's cellular microenvironment.

1.4.1 Smart Polymers

Polymers have been extensively used in biomaterials application[59]. In the previous sections, we have discussed several of the more popular polymers. Researchers have recently turned to use polymers as a novel therapeutic delivery system as they have developed polymers that can respond

to various stimuli deliver therapeutic agents while limiting any adverse effects effectively[60]. These smart polymers are designed to release their compounds in response to various internal and external triggers, including chemical, physical, and biological[60]. Thus, the smart polymer can be designed to release a drug only when responding to a set trigger, including internal stimuli such as activation by a host enzyme or even changes in the local pH. Similarly, external stimuli can include activation via electromagnetic, light or acoustic energy[60]. Together, this allows researchers to design smart polymers loaded with a drug to directly release the compound into the surrounding tissue without raising the compound's baseline levels in the patients.

1.4.2 Natural Inspired Biomaterials

Natural biomaterials derived from endogenous proteins have been used as a delivery vector for various therapeutics forms as endogenous protein-based materials can be enzymatically or hydrolytically degraded by the host[61]. A typical immunogenic response occurs with allogenic protein or tissue that are derived from animal sources [61]. Interestingly, natural materials based on polysaccharides, especially cellulose, have historically demonstrated biocompatibility when implanted in various models[61–73].

1.5 History of Cellulose

The French chemist, Anselme Payen, was the first to isolate cellulose from plant tissue in 1838 [74]. Through elemental analysis, he characterized the fibrous solid extracted from plants and determined the molecular formula of $C_6H_{10}O_5$. The term cellulose was coined and first appeared at the French Payen Academy of science in 1839 [74]. Even though cellulose was first isolated in 1839, plant cellulose has been used as a biomaterial and other applications throughout history and remains one of the most used natural polymers. Currently, the global cellulose fibre market is

worth more than 220 billion USD in 2018 [75]. With annual biomass production of $1.5X10^{12}$ tons of biomass, cellulose is the most common organic polymer and is considered a renewable raw material[74].

1.5.1 Hierarchical molecular structure of Cellulose

The organized crystalline structure of cellulose found in native plant tissue is hierarchical. Cellulose polymers protofibrils are linked together, forming microfibrils bundled to make fibrils that comprise the fundamental elements of the plant cell wall[68]. Each level of filament contributes to the overall properties of the cellulose material. At the most basic unit, the cellulose polymers are linear syndiotactic polysaccharides of D-glucose molecules linked through β(1→4) glycosidic bonds (Figure 1.3). These distinct β (1→4) glycosidic bonds are responsible for the polymer's straight-chain conformation [76]. The β(1→4) glycosidic bonds result in the subsequent D-glucose units rotating 180 degrees along the glycosidic bond axis. The transposition of the methanol group of carbon-5 provides the equatorial conformation that gives the polymer the rigid, stiff-like conformation[76]. Most vertebrates do not directly express the cellulase enzymes required to break down the β(1→4) glycosidic bonds, and as such, cellulose provides very little nutritional energy [77]. A polymer such as starch and glycogen are also composed of D-glucose units but are linked via α(1→4) glycosidic bonds that result in aligned glucose units ensuing in polymers that branch and are digestible by vertebrates. The length of the elementary fibrils cellulose polymers (degree of polymerization, DP) varies from the plant source, with wood pulp ranging from 300-1700 DP, while cellulose sourced from cotton typically have DP of 800-10, 000[74] (Figure 1.3). The straight conformation of cellulose polymers and the hydroxyl groups drives the cellulose elementary fibrils' formation to form the microfibrils through the intrachain, interchain, and intersheet hydrogen bonding and van der Waals interactions[68,74]. Within plant tissue, the microfibrils form Cellulose-1

conformations that have elementary polymers aligned in parallel conformation in a twofold screw axis[78]. Cellulose-1 has two distinct crystallized structures that differ in the arrangement and stacking of hydrogen-bonded layers[79]. Cellulose 1α crystals have polymer layers offset from the molecular axis by +c/4; conversely, 1β crystal alternates between +c/4 and −c/4 displacement [79]. Both crystal microfibrils are native in plant tissue, but 1β is the predominant form in higher plants, while cellulose Iα is associated with bacterial and algal cellulose-producing organisms[68]. Cellulose-2 and 3 are alternate crystal unit variations of microfibrils but can only occur via synthetic production[68,74]. Cellulose fibrils are composed of multiple linear arranged microfibrils with strong networks of complex hydrogen bonds between the hydroxyl groups of the D-glucose, resulting in long fibril formation of crystalline rods along the microfibril axis (Figure 1.3). Cellulose fibres are the cell wall's building block and are composed of cellulose fibrils with lignin, hemicellulose, and other non-structural components like waxes and pectin inorganic salts and nitrogenous salts [76]. The plant cell wall has an extracytoplasmic heterogeneous membrane that forms a complex structure. The cell wall comprises several layers: the thin primary wall encapsulated by the much thicker secondary cell wall. The secondary cell wall maintains the plant's shape, rigidity, strength and composes the significant component of vascular tissue plants. The secondary cell only begins to develop after the plant cell has divided; thus, microfibrils' direction differs between the secondary cell wall levels[76].

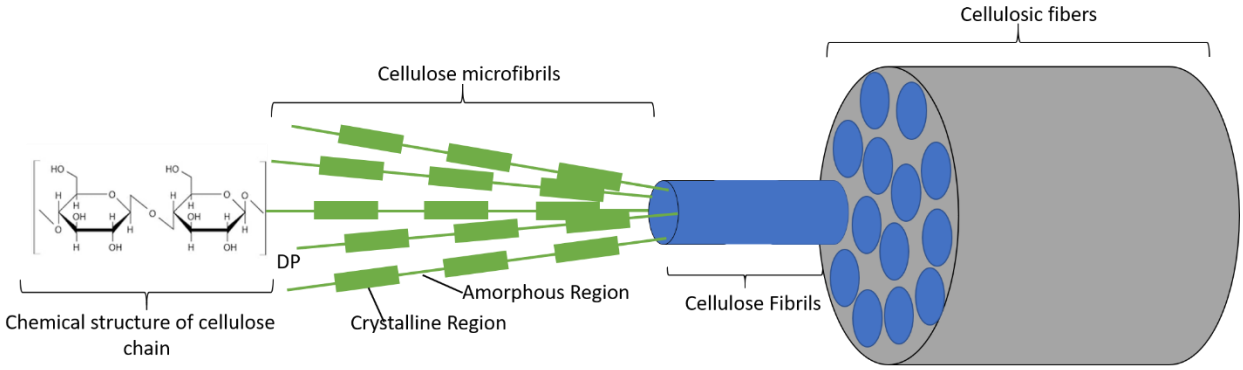

Figure 1.3 Cartoon schematics of the hierarchical cellulose fibres The hierarchical structure of cellulose from a plant source. The chemical structure of a single cellulose polymer of D-glucose molecules linked through β(1→4) glycosidic bonds. DP is the degree of polymerization that varies between plant sources. The straight conformation of cellulose polymers and the hydroxyl groups lend the cellulose elementary fibrils to form the microfibrils by intrachain, interchain and intersheet hydrogen bonding and van der Waals interaction. Cellulose fibrils are composed of multiple linear arranged microfibrils with strong networks of complex hydrogen bonds between the D-glucose hydroxyl groups, resulting in long fibrils. Cellulose fibres are the cell wall's building block and are composed of cellulose fibrils with lignin, hemicellulose, and other non-structural components like waxes and pectin inorganic salts and nitrogenous salts. Created in Biorender.com

1.5.2 Cellular Adhesion to Cellulose

Animal cells *in vivo* are incorporated within the extracellular matrix (ECM) of their respective tissue[80–82]. The ECM is a three-dimensional composition of macromolecules' interwoven network of proteins and enzymes, with an analogous role to the plant cell wall. The ECM provides structural and biochemical support for cells while behaving as a stress buffer or transmitter for externally applied forces[80–82]. ECM composition is unique for each tissue, allowing for cell adhesion and integration via integrin attachment to the Arg-Gly-Asp (RGD) via matrix motifs [80–82]. Plant cell walls do not contain proteins with the RGD motifs, nor do mammalian cells express native cellulose-binding domains. As such, mammalian cells do not readily adhere to cellulose surfaces [83]. However, cellulose scaffolds are particularly adept at the absorption to ECM ligands, growth factors (GFs) that are present in mammalian cell culture growth medium and as such can be easily

treated to absorb the biomolecules that contain RGD motifs. Mammalian cells can indirectly bind to the cellulose scaffold surface via matrix ligand biomolecules through integrin receptor complexes that bind via the surface absorbed proteins[68,83] (Figure 1.4). Mammalian cell integrins have a heterodimer structure that composed of α and β sub-units[84]. The integrin's specificity comes from the different combinations of the 24α and 9β proteins [84]. Within the ECM, the process of inside-out signalling modulates integrin affinity for a specific ligand by inducing high-affinity conformation change within the integrin [84]. The activated integrins are then sequestered to the cell membrane, where they cluster to reinforce links from the cell- matric ligand interface via complexes known as focal adhesions (FA) (Figure 1.8 b) [85,86]. FA are complexes that include several diverse scaffold molecules that include GTPases and enzymes such as kinases, phosphatases, proteases and lipases [87].

Figure 1.4 C2C12 cells are cultured on 3D cellulose scaffolds. SEM image of a cellulose scaffold cross-section after being seeded with C2C12 cells allowed to proliferate for four weeks. (Scale bar = 20 μm)

Focal complexes are early-stage focal adhesion sites that are localized at the periphery of migrating cells[88]. Individual FA protein complexes depend on the composition and mechanics of the surrounding ECM distinguished by the cell via integrin binding[88]. FAs are the central hub of cell-ECM interactions where the forces are transmitted from the cell to the ECM. FA are complex dynamic structures that are organized into a transmembrane and intercellular layer[88]. Within the cell s the FA protein complexes involve the scaffolding, docking and signalling proteins that connect the exterior integrins to the internal cytoskeleton[89] (Figure 1.8b). The cell's substrate's focal adhesion complexes reflect the ECM components and the mechanics of the cell's substrate as determined via the cell's integrin binding. The FA complex's intracellular proteins are known to have roles independently in detecting mechanical cues and propagating mechanical force signal transduction[90]. A combination of innate cellular machinery and the numerous available hydroxyl groups of the amorphous cellulose fibrils allow for mammalian cellular adhesion to the plant cell wall cellulose surface[68] (Figure 1.1 and 1.4).

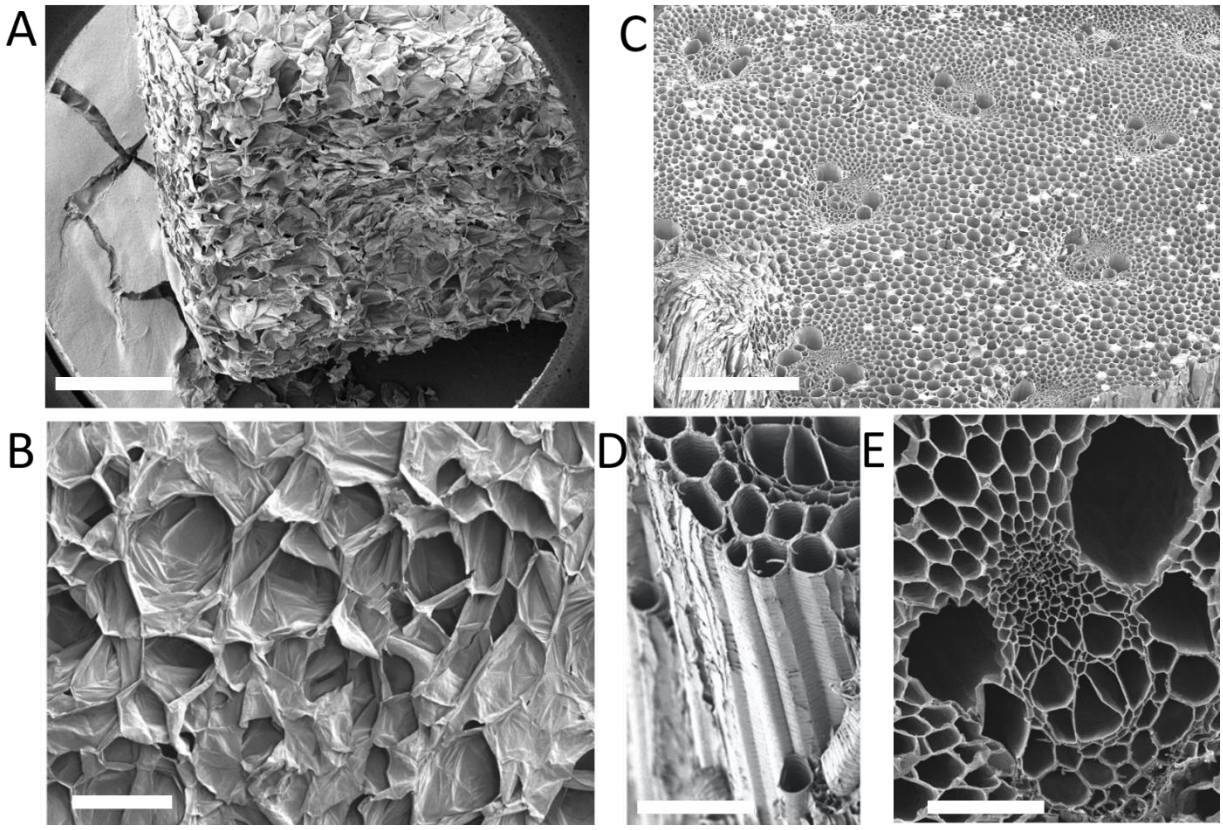

Figure 1.5 Plant Cell wall of Apple hypanthium and *Asparagus officinalis* Vascular Bundle a) Decellularized SEM plant-derived scaffolds of apple hypanthium tissue. The porosity of the scaffold is apparent with the overlapping cell wall cavities. The scaffold's physical dimension remain even after decellularization. (Scale bar = 1.5 mm) b) SEM image of apple hypanthium cellulose scaffold revealing its three-dimensional nature and large cavities. (Scale bar=200 μm) c) Decellularized plant-derived scaffold of Asparagus with visible vascular bundles (VBs) surrounded by parenchyma (Scale bar= 0.7mm). **d)** SEM reveals scaffolds also have a grooved outer topography. VB channel architecture runs the entire length of the scaffold (Scale bar=300μm). **e)** Imaging the scaffold cross-section at higher magnification reveals a VB (bar=100μm).

1.5.3 The Plant cell wall of Hypanthium and Vascular Tissue

The cell wall was one of the first biological structures that Robert Hooke studied examined using a microscope and led to the establishment of The Cell Hooke theory in 1663 [91]. The cell wall begins its synthesis during the cytokinesis stage of the plant cells' life cycle. The two daughter cells form a cell plate that forming the primary cell wall[91]. The primary cell wall is relatively thin

compared to the mature cell wall and is easily extendible to accommodate the plant cell's growth. Once the cell's growth is complete, the secondary cell wall is synthesized with cellulosic fibres integrated with lignin, pectin polymers and cross-linked glycans[91]. Apple fruit tissue has an internal structure composed of cell walls that encompass pores and air pockets that facilitate the transport of nutrients and water throughout the fleshy tissue[92]. The cell wall architecture's porous structure comprises overlapping cell wall cavities with diameters ranging from 100-300μm with a cell wall thickness of 4.04±1.4μm (Figure 1.5 a, b). Tracheophyte plants, including clubmosses, horsetails, and ferns gymnosperms and angiosperms) evolved distinct vascular structures that facilitate the transport of water and nutrients in the xylem and phloem[1]. Xylem are lignified channels within angiosperms that have developed for water and nutrient transport, derived from the root tissue, and function as a support function in the stem of plants: phloem structures, transport products of photosynthesis from source tissues to sink root tissues[1]. The VBs architectures and distribution vary among the plant types[1]. The stem of the monocot angiosperms *Asparagus officinalis* contains VBs distributed in a circular pattern (Figure 1.5 d, e and Figure 1.6 1 a,b,c), generally separated from one another by 612±70μm of overlapping parenchyma tissue. Scanning electron microscopy (SEM) of the vascular tissue reveals a variety of structures with characteristic diameters, such as xylem channels (51±15 μm), sieve tubes (40±16μm), parenchyma (35±8μm) and the phloem (9±2μm) (Figure. 1.5 c, d, e). On average, each scaffold contains 11±2 VBs, each containing 35±5 microchannels. These channels were observed to be consistent in diameter and orientation throughout their entire length and can be seen emerging from both ends of the scaffold in the same position. The *Asparagus officinalis* plant tissues are mechanically anisotropic due to the linear orientation of the VBs along the plant stem with an elastic modulus of 148±53kPa or

12±4 kPa when measured parallel or perpendicular to the long axis, respectively. These properties are within the range of healthy rat spinal cords[39,40].

1.6 Decellularization of Mammalian and Plant tissues

Allogeneic organ transplantation is currently the only treatment for patients suffering from end-stage organ failure. With 2,782 organ transplant procedures performed within Canada in 2018, organ transplant continues to be the only option to improve Canadian patients' quality of life. In 2018, 4,351 patients were on the waiting list for an organ transplant, with 223 patients dying while waiting for an organ transplant [93]. This statistic highlights the shortage of donor organs, resulting in extend patient waiting lists [93]. As with any transplant, the patient must be matched with the donor to limit any adverse rejection effect, creating a bottleneck when matching available organs with patients[93]. Decellularized tissues provide a potentially exciting new source for organ replacement. The field of whole organ tissue engineering has always been held back by the lack of current technologies to produce scaffolds with the internal adequate ECM microarchitecture[94]. However, 3D biological microcontact printing continues to improve in creating specialized microscale scaffolds to mimic tissue[26]. As such, decellularization has become a prevalent method in tissue organ engineering. It allows researchers to relatively quickly decellularize whole organs removing the cellular component leaving just the intact ECM architecture for re-seeding with patient-derived cells [94]. Tissue engineers have succesfully decellularized tissues and whole organs such as hearts, lungs, kidneys, and the pancreas. However, the patient seeding techniques and protocols to functionalize the ghost tissues are still lacking[94,95]. This thesis outlines the first published works of adapting and establishing the decellularization protocol for cellulose plant tissue to create biomaterials (Chapter 2 and 3). The Pelling lab has published several works on decellularized scaffolds that have gone on to inspire labs worldwide to approach decellularized

plant scaffolds[73,92,96]. Chapter 3 demonstrated that plant kingdom structures' various cell wall architecture allows researchers to source plant tissue for unique needs [73]. This challenge has been accepted as researchers worldwide have used various plant tissue, including; celery, spinach leaves, leeks, bamboo, vanilla, orchid, parsley, persimmon, jujube, sweet pepper, calathea, solenostum, green onion, carrot, broccoli, cucumber, potato, tobacco with apple hypanthium tissue still the most popular [6–13]. The Ju group has shown that apple hypanthium tissue is compatible with the supporting iPSCs that differentiated into osteoblasts. When grafted into bone, the apple scaffolds demonstrated biocompatibility and osteointegration in a rat model[7]. Their *in vivo* results mirrored what we had reported in our original paper (Chapter 3), including; biocompatibility, protein deposition/remodelling, and blood vessel formation; importantly, these results corroborate our claims but highlight the multi-functionality of apple hypanthium cellulose scaffolds. We observed that the VB and internal asparagus cell wall structure had striking similarities to SCI scaffolds designed to repair SCI in animal models[95,97–103]. (Figure 1.6 d-i) Although varied in material and production techniques, these scaffolds have several key design commonalities; mechanical support to the lesion site, orientated channels for physical guidance cues for projecting axons, exhibit a low FBR, could be loaded with therapeutic molecules and, therapeutic cell adhesion. Additionally, a review of currents scaffold devices highlighted the success of natural polymer over synthetic polymers, specifically cellulose, in averting the FBR response and astrogliosis in SCI[95,97,104–107]. (Figure 1.6 d-i) This lead us to hypothesize that the asparagus VB scaffolds could be adapted to an SCI scaffold in animal models.

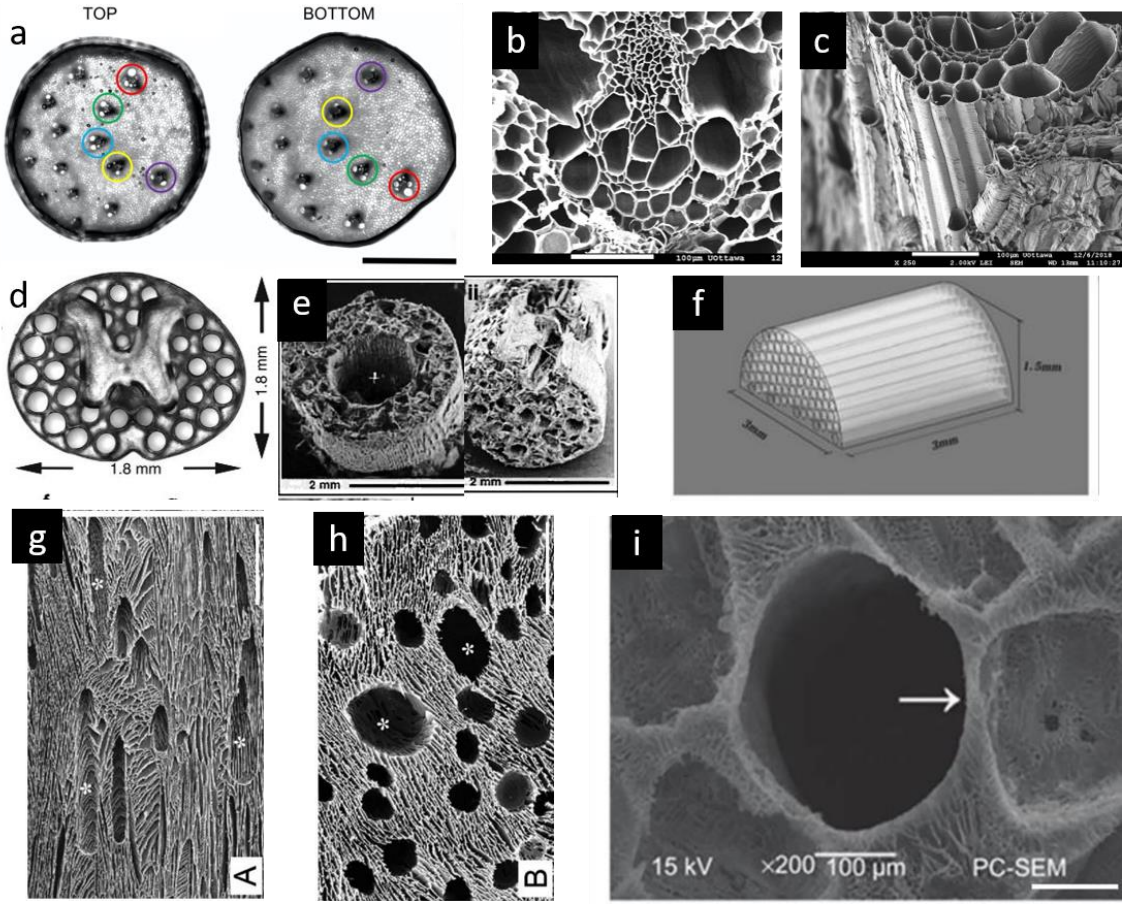

Figure 1.6 The physical similarities in the natural cell wall architecture compared to designed scaffolds to treat SCI. A cross-section of the asparagus SCI scaffold. Various SCI scaffolds are fabricated via several techniques, but with key parallel channel architectures **a)** Phase contrast image of the entire surface of the asparagus scaffold reveals the distribution of the VBs. Notably, VBs on the top surface emerge in nearly the same position on the bottom surface. Individual VBs are circled in different colours. As the scaffold is flipped over to image each side, the VB positions are also flipped (bar=2mm). **b)** High magnification SEM imaging of an individual VB revealing the channel structures within the asparagus scaffolds (bar=100µm). **c)** VB channel architecture runs the entire length of the scaffold (bar=100µm). **d)** SCI scaffolds produced with micro-continuous printing to mimic the native rat spinal cord's linear white tracts. Channels are distributed throughout the scaffold with solid similar to the distribution of VBs of an asparagus scaffold. **e)** Salt-leached porous poly(ε-caprolactone) cast in a channel and open path-with core designs that match the asparagus scaffolds' physical dimensions. Wong et al. found that these designs resulted in the best tissue ingrowth, myelinated fibres, inhibition of astrocytes and axonal infiltration than other SCI scaffolds[102]. **f)** The SCI scaffold design comprises HA containing parallel hollow channels throughout the scaffold as with the VBs of asparagus SCI scaffold[101]. **g)** Saggital section and **h)** axial section of directional frozen PLA scaffolds under SEM. The channels were oriented in the direction of cooling[103]. **i)** Axial section of PLGA scaffolds under SEM demonstrating the channel structure of SCI scaffold [108]

1.7 Spinal cord scaffold design characteristics.

Researchers designing scaffolds to reconnect injured spinal cord injuries face several unique design challenges respective to CNS. The successful SCI scaffolds have several common design characteristics, including; biocompatibility, mechanical strength, scaffold morphology and, therapeutic cell/molecule delivery[106,109]. For the scaffold to provide contact guidance for neurons, the scaffold must be biocompatible and permissive for cell adherence[109]. Any scaffold that triggers a strong chronic FBR will ultimately lead to implant rejection-resulting in catastrophic secondary pathologies, especially in prone areas as the CNS[110]. Researchers must design SCI scaffolds composed of materials that do not incite FBR; such materials tend to be natural polymers [106,109]. Collagen is a natural polymer that demonstrated both favourable biocompatibility and degradable characteristics [106,109]. Recent studies have shown how collagen-formed channels can align axon projection and lower levels of GFAP scarring[97,109,111]. Hybrid scaffolds composed of chitosan and collagen scaffolds, have shown a lower degradation rate while maintaining axon projection and motor recovery[104,109,112]. Agarose, a sugar polymer, has a low degradation rate and can maintain physical support over a month *in vivo* that can be extended with cross-linking treatments. Freeze-dried agarose techniques can create hollow uniaxial channel structures within the scaffold. (Figure 1.6 g, h) with tunable diameters. Freeze-dried agarose scaffolds have shown promise in rat SCI models showing integration into the spine and axonal alignment within the channels[106,109]. Hydroxyapatite (HA) has also been shown to have limited success as SCI scaffolds (Figure 1.6 f). When processed into channels loaded with poly- L-lysine and nogo-66 receptor antibody inhibits detrimental glial scar and promotes angiogenesis[106,109]. Natural polymers have shown promise as the backbone polymer in SCI scaffolds as they show low immune response by the host and degradability[36,53,106,109,113–125]. These natural polymer SCI scaffolds are purified from their natural

source (or synthesized) and reconstituted into scaffolds that ultimately degrade within the host. The dogma that long-term biomaterials have to degrade within the host ultimately has been losing momentum, a relic from the second generation FDA biomaterial requirements[95]. SCI scaffolds need to provide the injury site protection from various external forces for the implant's lifetime. A degrading scaffold will ultimately lose all mechanical support and no longer provide the essential physical support required to align regenerating axons[26].SCI scaffolds provide physical guidance cues to align axons projections. One such approach is the use of uniaxial orientated channels (50-400 microns) that have shown the promotion of axonal alignment and increased integration into spinal cord[39,102,106,109,126,127] (Figure 1.6 d-i). The uniaxial channels are fabricated using various methodologies as they have been shown to promote axonal alignment in animal models[95,97–103]. Multiple studies have demonstrated motor recovery with SCI scaffolds combined with the therapeutic cells/compounds. Yet, many of these studies only show motor improvement when the SCI scaffold is combined with therapies rather than improvement from the scaffold alone[26,128,129]. The work in this thesis (Chapter 2) demonstrates plant-derived scaffolds have shown that they are biocompatible with various mammalian cells and are corroborated with the findings of multiple groups [6–13]. Together, the asparagus VBs scaffold demonstrates the key characteristics of successful SCI scaffolds (Figure 1.7), and as such, we hypothesized that the plant-derived cellulose cell wall architecture could function as an SCI scaffold.

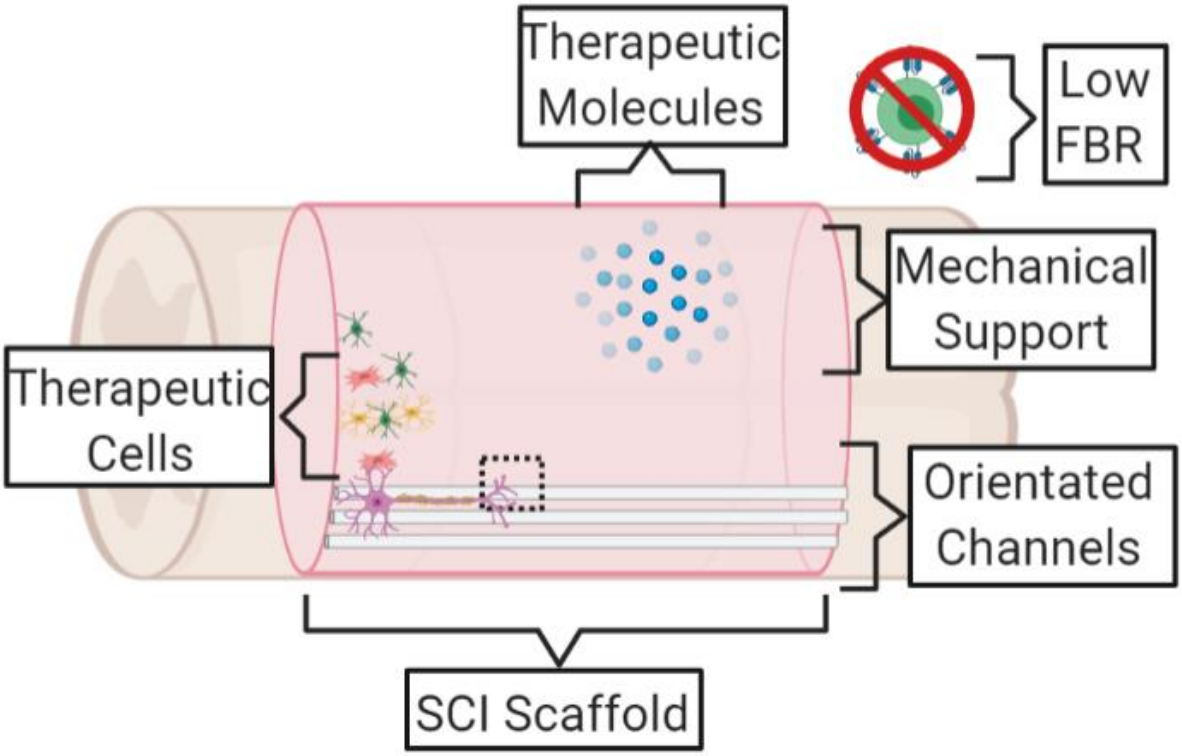

Figure 1.7 The five characteristics of an ideal Scaffold. The scaffold (pink) connects the injured spinal cord tissue (brown). The ideal SCI scaffolds must provide the injury lesion site with mechanical support to the injury site, orientated channels for axonal guidance, biocompatible, allow for therapeutic cell loading and therapeutic molecules. The smaller dashed box outlines the growth cone of a CNS neuron projecting axon that is being guided via topographical cues of the orientated channels. Created in Biorender.com

1.7 Neuron Structure and Function Overview

Typically, neurons have a polarized structure with a cell body (soma) centred around projecting dendrites and axons[130]. The size of the neurons is dependent on the anatomical location of the neurons.[130] Neuron cell morphology various between specific neuronal cell types; however, all neurons share four distinct cell regions, dendrites, soma, axon and axon terminals, each of which has a unique function[131].Dendrites are specialized membrane projection that receives chemical signals from the axon termini of neighbouring neurons via synapsis and propagates the signal inwards towards the axon hillock[132]. Neurons have complex dendrite projections that allow for multiple interconnections of neurons. The axons are specialized membrane projection structures emitting from the soma of neurons that conduct electrical impulses[132]. Action potentials (AP) are initiated at the axon hillock, located at the soma base, where both chemical inhibitory postsynaptic potentials and excitatory postsynaptic potentials cumulate in an all or none response resulting in an AP[132]. Within the cell, AP results in a sudden depolarization of the -70 mV resting state of the membrane potential of the neurons[132]. The activation of Na^+ channels results in an influx of Na^+ ions that further activate Na^+ and K^+ leak channels (rising phase). At the peak phase, +40 mV, Na^+ voltage channels are closed, resulting in the displacement of K^+ ions across the electrochemical gradient through K^+ that have been activated as a result of the positive membrane potential[132]. As the membrane potential continues to decrease, K+ channels remain activated in a delayed response[132]. The delay activation causes an undershoot of the resting potential. The period where the membrane potential normalizes back to the resting potential is referred to as the refractory period[132]. Axons are typically myelinated by Schwann cells to facilitate efficient and faster propagation of signal[132]. Myelin is a lipid and protein insulating sheath that surrounds the axons and acts as another barrier to ions or leak channels improving the efficiency of AP[132]. There are

periodic gaps in the myelin sheath, nodes of Ranvier, that act to amplify the AP by allowing the Na^+ gated channels to activate and increasing the positive charge across the membrane[132]. The AP's signal is propagated to other cells at the axon terminals, containing the synapsis structures[132]. A single AP within one CNS neuron can propagate several neurons at the axon terminal[132].

1.8 Axon Projection

Axon guidance is a critical step in neural development that allows for extending axons to connect with specific destinations[130]. This process is critical as it ultimately forms the neural networks of the nervous system. There are many aspects of axon guidance that remain unclear; however, the dynamics of motile actin-contractile complexes that powers the growth cone projection are well understood [130]. A growth cone is a subcellular structure found at the tip of axons projection that functions to sense and navigate the neuron's surrounding microenvironment. Growth cones are powered by F-actin polymerizing and projection[130]. Growth cones are organized into three regions; peripheral domain (P), transitional domain (T) and the central domain (C)[130]. The P domain encompasses the growth cone extremities with structures of filopodia and lamellipodium. The lamellipodium is cytoplasm cell projections within the leading edge of the cell[133]. The cytoskeletal components of the peripheral domain include the unipolar F-actin bundles embedded in a dense actin network[133]. (Figure 1.8 a**)** The T domain encompasses the interface regions of the P and C domains[133]. The C-domain that centers the growth cone comprises the microtubules, organelles, vesicles and several cytoskeletal-associated proteins[133,134].

The size of a growth cone is variable, ranging from 10 μm^2 to 160 μm^2, depending on the existing growth cone conditions, cell type and ECM parameters[135]. The axons' diameter can vary from 0.08

µm to 20 µm, with the largest diameter at the soma base decreasing as the axon extends from the soma [136–138]. The filopodium diameter is 100-300 nm range, making it the smallest structure contributing to neurite guidance [139] (Figure 1.8**).**

The proteins associated with FAs in non-neurons cells also have a similar mechanosensor role within growth cones such as p130Cas, talin, and filamin[140]. Mechanical activation of the p130 causes a conformational change in the protein, exposing a tyrosine residue for Src and Abl kinase phosphorylation leading to several signalling cascades [141]. p130Cas enzymes are also regulated by mechanically-dependent netrin–integrin signalling during axon guidance[142]. The talin protein has several roles within the growth cone, where it is critical for the FA site assembly and F-actin stabilization. Similarly, filamins expose cryptic binding sites for signalling molecules, including RhoA, ROCK, p21-activated kinase and PKC [140]. Significance of the filamins is highlighted as developing animals with knocked-out filamins demonstrate premature axon termination, ectopic branching, and aberrant pathfinding *in vivo*[140] (Figure 1.8 b).

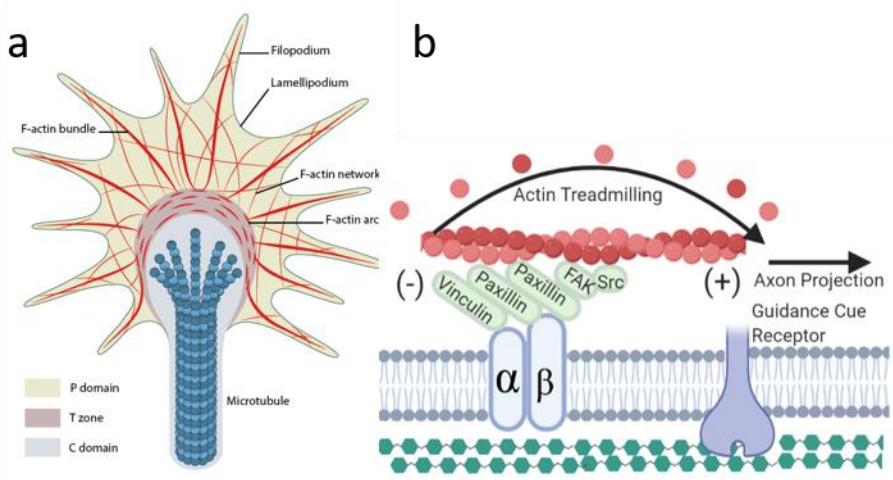

Figure 1.8 Cartoon of the axon growth cone and the cytoskeletal skeleton's organization in the growth cone. a) The three zones (P, T and C domains) of the axonal growth cone are represented with microtubules (blue) and F-actin (red) b) The larger dashed box demonstrated the key molecular components of an axon growth point. Alpha and beta heterodimeric (Light blue) integrins are in the membrane (grey) that are seen adhered to the cellulose substrate (green). The integrins' cytoplasmic tail recruits the scaffolding proteins' assembly, including talin, paxillin, and vinculin. The FAK and Src phosphorylated key sites, when mechanically activated that further initiates signalling cascades. Actin filaments (red) are bound to the ECM (green) through the integrins and generate the membrane protrusion forces via the actin polymerization stemming from the positive end (+). Guidance cues (dark blue) can promote the axon growth cone's direction via activation of FAK and Src tyrosine kinase, modulating adhesion and cytoskeleton turnover. Created in Biorender.com

1.9 Axonal Guidance Cues

Depending on the neuron's nature, axons may need to navigate various tissues and sometimes the entire embryo's entire length to find its exact intended neural circuit target[143]. The precision necessary for axon targeting is highlighted in the extreme adverse neurological disorders during flawed neural circuit development.[144] At the axon growth cone, integrin receptor proteins are expressed that interact with molecules of the ECM distributed throughout the axon path that cumulate in an attractive or repulsive response. Together, axons rely on the crosstalk between short and long-range guidance cues to navigate their multiple respective targets. For guidance cues, axons must reach their intermediate target before moving on to the subsequent targets along the axon projection trajectory towards its final intended target. The intermediate target acts to give axons local guidance information and promote the axon projection to the next stage once the axon has reached it. The switch (attractant to repulsive) mechanism of intermediate guidance remains poorly understood. The molecular switch must do so with exact timing[145]. A premature switch would inhibit the initial contact of the growth cone, and a delayed switch could cause the axon to stop prematurely before reaching its target[145]. In developing CNS, the switching events can be observed at the spinal cord's ventral midline floor plate, where the axons collectively halt growth before migrating together[145]. The switch mechanism is thought to be brought on by a change in surface receptors' expression on the axonal growth cones [145]. The spinal cord's axons at the floor plate depend on short-range molecule guidance, specifically the interactions between axonal contactin-2 and the neuronal cell adhesion molecule NrCAM of the floor plate[146]. With the high concentration of attractive signal guidance cues at the floor plate, a mechanism was needed to explain how the axons projected across the midline to targets that do not have such guidance cues. The axon projection was attributed to the repulsive molecule interaction of -Slits, which was found to target the axon receptor roundabout (Robo)[145].

Interestingly, Robo's growth cone surface expression was found dependent on the growth cone current location, while the axons growth cone were located on the floor plate did not express the receptor [145]. Whereas, once the axon growth cone reached the floor plate, the Robo protein is expressed to the growth

cones so as to expel the axons towards the midline[145]. The Robo regulation has been studied in multiple animal models, with the current theory suggesting that Robo is regulated via a post-translational modification [147]. Additionally, there are several other classes of signalling cues that The repellent molecule Class-3 semaphorins is also associated within the floor plate, and like Slits, the expression is dependent on the axon position across the midline[145]. The receptor proteins of the signal molecules semaphorins (Sema3B, and Sema3F), including the plexin A1 and neuropilin-2 are disintegrated by the enzyme calpain, a calcium-dependent protease [145]. Caplain's activity is regulated by the NrCAM adhesion molecule, which is present only on the floorplate. When the axon growth projects to the floorplate, the calpain is inactivated via NrCAM, allowing integrin plexin A1 to be expressed onto the surface of the growth, promoting the repulsion axon once crossing the floor plate[148]. Netrins have been shown to direct axon and cone growth and are critical in the early CNS development and the development of axonal outgrowth [149]. Moore et al. demonstrated that growth cone integrins binding to the netrin result in the activation of FAK molecule that can generate tractions forces larger than 60pN *in vitro* [142].

Additionally, within the growth cone, a receptor-like protein tyrosine phosphatase alpha (RPTP-α) can sense the underlying ECM stiffness to regulate axon extension. RPTP-α binds to the intracellular domain of the αvβ6 integrins, which promote the adhesion signalling through the activation of Src tyrosine kinases [150]. If RPTP-α responds to mechanical stimuli is still not understood[150]. (Figure 1.8 b)

1.10 Classifying the type of Spinal cord injuries

Although the common symptom of all spinal cord injury (SCI) is a loss potential of a motor function, the actual injuries are patient-specific[110]. All injuries will be unique depending on an

extensive list of factors, both mechanics of the actual injury and the patients' background. There are several other characteristics of human SCI that contribute to the total extent of symptoms. The lesion's size can vary but does not correlate to the extent of the motor and sensation loss[110]. SCIs are rarely restricted to just a single lesion with multiple lesions present throughout the spinal cord's injured area. In such events, there is not a sum of its parts affect, in which several lessons do not immediately make the prognosis several times worse. As such, it becomes difficult to study SCI without categorizing injuries into broad groups[110]. Bunge et al, were the first to categorize SCI into a classification system of four groups; Solid Core, Contusion/Cavity, Laceration and Massive compression[151].

In patients, solid cord injury, which represents around 10% of all SCI, refers to the injuries to the spinal cord that appear acutely undamaged to the surrounding tissue. None of the expected softening, discoloration, and or cavity formation appears at the initial stage injury site. However, with time the damage to the spinal cord and surrounding tissue becomes apparent. (Figure. 1.9b)

Contusion/cavity injuries are the most common and account for 49% of all SCI. Contusion injuries display no disruption of the dura and or the spinal cord surface anatomy. As the injury develops, the injured site displays hemorrhage and necrosis that progress into cysts within the parenchyma. Typically, the cyst tapper rostrally and caudally and develop into a cone's shape along the ventral regions of the posterior columns. (Figure. 1.9c)

Laceration are clear-cut disruptions in the parenchyma tissue's surface anatomy and account for 21% of the cases. Caused by penetration of the spinal cord injury by sharp fragments of fractured bones or projectiles. The lesions are distinguished by extensive damage to the underlying parenchyma with the epicentre dominated by collagenous connective tissue deposition. (Fig.1.9d)

Massive compression injuries are associated with severe vertebral fractures and account for 20% of injuries. Compression injuries are distinguished by the cord's macerated or pulpified appearance. There is a tangled mesh of connective scar tissue at the lesion's epicentre with nerve roots' surviving fragments. (Fig 1.9e)

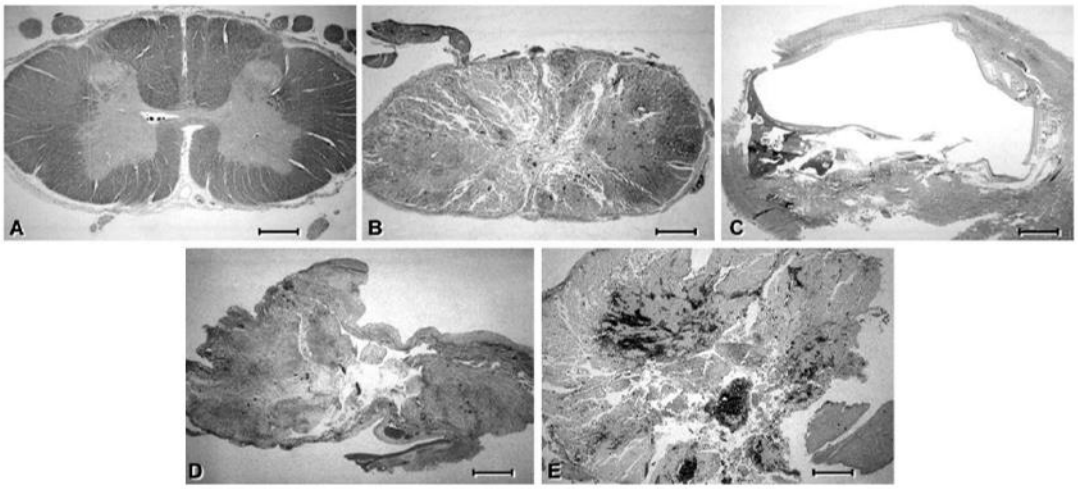

Figure 1.9 Cross-sections of human spinal cord with the various etiologies of Spinal cord injuries. a) Cross-section of healthy spinal cord. b) Cross-section of solid cord injury demonstrating a loss of the normal spinal cord architecture but with significant myelin loss from Wallerian degeneration. c) Cross-section of contusion injury. A cyst has replaced the spinal cord. d) Cross-section of laceration injury that has breached past the pia surface and into the spinal cord. e) Massive compression damage highlighting fragmentation, distortion, and hemorrhage. (Scale bar = 2mm for all) [110]

1.11 The pathophysiology of spinal cord injury

The pathophysiology of SCI is categorized into primary phase and latent phase. In the primary phase, the damage directly results from the injury's initial mechanical force and the total accumulated damage to the remaining spinal cord and surrounding tissue from secondary damage,

including; loss of vasculature and oxidative stress resulting in increased cellular death [110]. The most common spinal cord injury (49%) is compressive injuries resulting from falling injuries[110]. The primary injury site has little or no gross observable damage to the spinal cord with compressive injuries. The extent of injuries only comes apparent with the onset of secondary stage injuries that follow from persistent increasing contusion pressure[110]. The lack of visible injuries highlights the importance of understanding the secondary phase of SCI pathology's timing dynamics to mediate unrelenting symptoms. In the secondary phase, several physiological events determine the patient's outcome, including Wallerian degeneration and the formation of glial scarring at the stumps. Oligodendrocytes, the CNS's supporting cells, are seen in active apoptosis stemming from the rostral and inferior ends of the SCI stump at the onset of the injury. This initial apoptotic core can stem up to 13 mm from the SCI lesions and continue up to 8 days after the patient's initial SCI and result from hemorrhaging pressures at the tissue[123,152,153].

Wallerian degeneration; is the further breakdown of distal surrounding healthy spinal cord tissue stemming from the original injury site. Wallerian degeneration will be continuing to affect the surrounding healthy tissue in SCI patients and may take several years before the extent of the injury is stabilized [123,154]. The secondary phase of SCI is highlighted by the glial scar surrounding the spinal cord's lesions and damaged tissue. The formation of the glial scar is a universal response to trauma. Similar glial scar formation is observed in severe brain injuries, ischemic stroke and neurodegenerative diseases[123,155] Glial scar is extremely well studied in the context of SCI as it remains a physical obstacle that is thought to block the re-establishing of neural circuits [123,155]. When there is damage to the spinal cord, the lesion edges begin to hypertrophy with astrocytes surrounding the lesion and proliferate to form a border around the lesioned core [155,156].

The lesion's core is comprised of a rich deposit of ECM proteins that inhibit axonal growth and remyelination. (Figure 1.10) The astrocytes surrounding the lesion increase the cytoskeletal component glial fibrillary acidic protein (GFAP)[157]. The astrocytes continue to proliferate and extend overlapping processes forming gap and tight junctions to create a dense overlapping network the constitutes the scar[157]. Researchers have speculated the role of glial scar formation as it appears to impede neural circuit repair after injury [123,157]. However, the glial scar forms a border isolating the site injury critical in restoring the blood-brain barrier[123]. The glial scar protects the prone injured neurons by providing oxidative stress relief and stabilizing extracellular ion balance [156,158]. Researchers need to keep both the initial and latent tissue collapse stages in mind when designing an SCI biomaterial. The vast majority of SCI patients are within the chronic stage; however, researchers focus on acute injuries models.

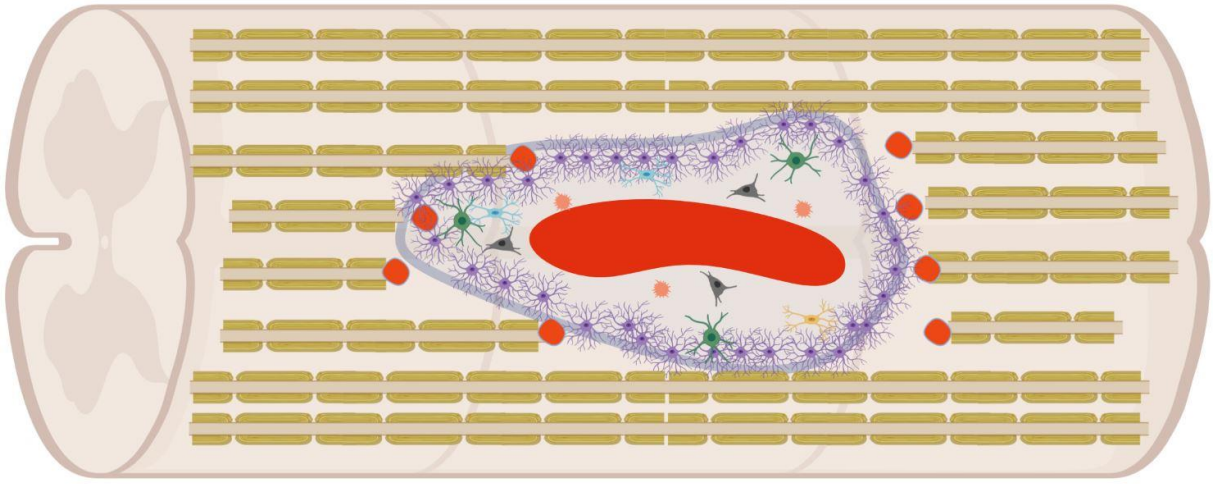

Figure 1.10 Cartoon representation of the formation of the glial scar and axon inhibition. The glial scar made of reactive astrocyte (purple) expressing elevated levels of GFAP, NG2 glia (green) and microglia (yellow) that form a dense network of tightly adhered cells that make up the glial scar to form a tight barrier around the lesion core, or area of severe tissue damage. The lesion core (purple core) have both the primary injury (red) and the latent tissue injury and contains macrophages (orange) and stromal cells (black). Injured axons (red circles) that can not navigate across the glial scar. Created with Blender.com

Chapter 2 | *Manuscript*

APPLE DERIVED CELLULOSE SCAFFOLDS FOR 3D MAMMALIAN CELL CULTURE

Daniel J. Modulevsky[1], Cory Lefebvre[2], Kristina Haase[2], Zeinab Al-Rekabi[2] and Andrew E. Pelling[1,2,3,4]

[1]*Centre for Interdisciplinary NanoPhysics, University of Ottawa, Ottawa, Ontario, Canada,*

[2]*Department of Biology, University of Ottawa, Ottawa, Ontario, Canada*

[3]*Department of Physics, University of Ottawa, Ottawa, Ontario, Canada*

[4]*Institute for Science, Society and Policy, University of Ottawa, Ottawa, Ontario, Canada*

[5]*SymbioticA, School of Anatomy, Physiology and Human Biology, University of Western Australia, Perth, WA, 6009*

Submitted November 13, 2013 to PLOS One

Accepted May 19, 2014, https://doi.org/10.1371/journal.pone.0097835

- I, Daniel Modulevsky, contributed to the majority of the research work, including the production of the biomaterial's development, cell culture, scanning electron microscopy, image acquisition and data analysis.
- The arrangement of the manuscript has been modified for thesis formatting purposes.

Motivation |

- I hypothesize that cellulose scaffolds derived directly from plant tissue will act as a biomaterial supporting mammalian cell proliferation, invasion and growth.

2.1 Hypothesis and Objectives |

- Plant tissue can be decellularized, processed and sterilized without altering the cell wall structure or the mechanical properties.
- The mechanical properties of the decellularized plant tissue can be mechanically tuned with surface modifications including collagen coating and glutaraldehyde cross-linking while remaining biocompatible and capable of cultivating mammalian cells.

- Established mammalian cell lines, including NIH3T3 fibroblast, C2C12 precursor myoblast and HeLa human epithelial cells, can adhere to cellulose scaffold, migrate, proliferate and remain viable after 12 weeks of culture.
- The cellulose cell wall structure of the plant-based biomaterial will allow the mammalian cells to migrate into the biomaterial's internal structure.
- The porosity of the apple hypanthium cell wall architecture will allow for constant media turnover, reducing the necrotic core of cells within the internal structure of the biomaterial.

2| APPLE DERIVED CELLULOSE SCAFFOLDS FOR 3D MAMMALIAN CELL CULTURE

2.2 Abstract

There are numerous approaches for producing natural and synthetic 3D scaffolds that support the proliferation of mammalian cells. 3D scaffolds better represent the natural cellular microenvironment and have many potential applications *in vitro* and in *vivo*. Here, we demonstrate that 3D cellulose scaffolds produced by decellularizing apple hypanthium tissue can be employed for in vitro 3D culture of NIH3T3 fibroblasts, mouse C2C12 muscle myoblasts and human HeLa epithelial cells. We show that these cells can adhere, invade and proliferate in the cellulose scaffolds. In addition, biochemical functionalization or chemical cross-linking can be employed to control the surface biochemistry and/or mechanical properties of the scaffold. The cells retain high viability even after 12 continuous weeks of culture and can achieve cell densities comparable with other natural and synthetic scaffold materials. Apple-derived cellulose scaffolds are easily produced, inexpensive and originate from a renewable source. Taken together, these results demonstrate that naturally derived cellulose scaffolds offer a complementary approach to existing techniques for the in vitro culture of mammalian cells in a 3D environment.

2.3 Introduction

Development of novel biomaterials for the *in vitro* culture of cells in three-dimensional (3D) microenvironments has gained traction in recent years [48,55,159–162]. The motivation behind this development is to compensate for limitations of current two-dimensional (2D) cell culture practices. In particular, 2D plastic or glass substrates are ubiquitously employed to study many biological processes, despite the obvious structural and mechanical differences with the *in vivo*

microenvironment. *In vivo*, cells are found in a complex extracellular matrix (ECM) whose biochemical and physical properties have a significant impact on numerous critical physiological and pathological processes [163]. Significant morphological and biological differences have already been observed between cells grown on 2D versus 3D microenvironments [40,164]. It is has been routinely observed that primary cells isolated from tissues will become progressively flatter when cultured on conventional 2D surfaces [165,166]. However, cells cultured on 2D surfaces can regain their 3D morphologies when placed into a 3D culture scaffold [167]. 3D cell culture promises to more closely reflect the biochemical and physical properties of the cellular microenvironment found in tissues and organs [168], and so the development of novel biomaterials towards this effort is of considerable importance.

Both synthetic and naturally derived materials are currently employed in 3D culture methods in order to create tuneable scaffolds engineered with specific biochemical and physical properties. Cellulose, the major component of plant cell walls, is an organic polysaccharide made of D-glucose subunits through β(1-4) bonds. Unlike the polysaccharides starch and glycogen, cellulose provides very little nutritional energy as the β(1-4) glycosidic bonds are difficult to digest and can only be broken down by cellulase [77]. As such, there has a great focus on using cellulose as a candidate biomaterial [67,71,72,167,169–174]. Cellulose has previously been employed as a permeable dialysis membrane and as diffusion limiting membranes within biosensors[175]. As well, previous studies found that cellulose produced by bacteria could support the proliferation of mammalian cells [171,176,177]. Synthetically produced cellulose scaffolds have also been employed for 3D mammalian cell culture [160,170,172,174]. Myocytes cultured on these synthetic cellulose scaffolds contained periodic myofibrils, a distinct cytoarchitectural element within mature cardiac myocytes

[178]. As well, enhanced connectivity, in the form of increased gap junction density, and electrochemical connectivity, resulted from 3D culture, in comparison to cells grown on glass [178]. These examples suggest that cellulose may be a suitable material to support 3D cell growth. Moreover, cellulose is widely available as it is the most common organic polymer, accounting for $1.5x10^{12}$ tons of total annual biomass production [74].

Apple hypanthium tissue has an internal structure composed of cell walls that encompass pores and air pockets, facilitating the transport of nutrients and water throughout the fleshy tissue. These naturally developed characteristics, are important in any scaffold employed for 3D cell culture [179]. In order to act as a 3D scaffold, the apple hypanthium tissue must first be decellularized in order to remove existing nucleic acids, lipids, and proteins, producing a purified cellulose scaffold. Decellularization is now commonly employed on mammalian tissues to selectively remove cellular components while leaving behind an intact ECM [180–183] Typically, mammalian tissues are bathed in solutions, detergents and/or proteases, in order to produce a decellularized matrix that retains the shape of the original tissue[3,4,184–191]. Decellularized tissue can then be repopulated with new cells, in order to produce new functional organs. Hearts, kidneys have been decellularized and reseeded with various cells [3,4,183,191]. As well, functional bladders and lungs have be produced and transplanted into animals using this technique [192,193]. Importantly, decellularized tissue also maintains a well conserved native ECM architecture and cell-ECM binding domains [3].

In this study, we hypothesized that decellularized apple hypanthium tissue might provide an easily produced scaffold for 3D cell culture. The major aim of this study was to demonstrate that mammalian cells would successfully proliferate within a 3D cellulose scaffold in vitro. Through

modification of an existing decellularization protocol, we generated apple-derived cellulose scaffolds for cell culture. We examined how three mammalian cell types (mouse NIH3T3 fibroblasts, mouse C2C12 myoblasts and human HeLa epithelial cells) proliferated within these scaffolds, for up to twelve weeks. Phase contrast microscopy, laser scanning confocal microscopy and scanning electron microscopy were used to characterize the structure of the scaffolds, cell growth, cell morphology and the influence of the scaffolds on the actin cytoskeleton. We also modified the surface biochemistry and mechanical properties of the cellulose scaffolds by collagen functionalization, or chemical cross-linking with glutaraldehyde. Atomic force microscopy was employed to quantify the effect of these modifications on the mechanical properties of the scaffolds. We demonstrate that the 3 mammalian cell lines used in this study were able to proliferate and remain viable in the 3D cellulose scaffold *in vitro*, achieving cell densities similar to other synthetic and natural biomaterials. Given the natural porosity and ease of production of cellulose scaffolds, as well as the ability to modify their mechanical properties, we demonstrate that cellulose scaffolds are a potentially useful biomaterial that can be successfully employed for in vitro 3D cell culture.

2.4 Material and Methods

2.4.1 Apple tissue preparation, decellularization and storage

McIntosh Red apples (Canada Fancy) were stored at 4°C in the dark for a maximum of two weeks. In order to prepare apple sections, the fruit was first chilled in a -20°C freezer for 5 minutes prior to being cut with a mandolin slicer to a uniform thickness of 1.20 ± 0.14 mm, measured with a vernier caliper (Figure 2.1 A-B). Only the outer (hypanthium) tissue of the apple was used. Slices containing visible ovary-core tissue were not used. The slices were then cut into 2.0x0.5 cm segments parallel to the direction of the apple pedicel (Figure 2.1 C). Apple tissue was then decellularized by using a well-established protocol [3] for removing cellular material and DNA from tissue samples while leaving behind an intact and three-dimensional scaffold. Individual apple tissue samples were placed in sterilized 2.5 mL microcentrifuge tubes and 2 mL of 0.5% sodium dodecyl sulphate (SDS) (Sigma-Aldrich) solution was added to each tube. Samples were shaken for 12 hours at 160 RPM at room temperature (Figure 2.1 D). The resultant cellulose scaffolds were then transferred into new sterile microcentrifuge tubes, washed and incubated for 6 hours in PBS (Sigma-Aldrich) with 1% streptomycin/penicillin (HyClone) and 1% amphotericin B (Wisent). At this point, the samples were immediately used or stored in phosphate buffered solution (PBS) at 4 °C for no more than 2 weeks.

2.4.2 Post-decellularization treatments

Here, we examined cell proliferation and invasion into native, collagen functionalized, or chemically cross-linked cellulose scaffolds. In order to functionalize scaffolds with collagen,

samples were incubated for 6 hours in a solution of 10% acetic acid and 1 μg/mL rat tail collagen type I (Invitrogen), followed by washing in PBS before use. To chemically cross-link the scaffolds, the samples were incubated in a 1% EM-grade glutaraldehyde solution (Sigma-Aldrich) for 6 hours. The scaffolds were then rinsed in PBS and incubated in a solution of 1% sodium borohydride (Sigma-Aldrich) overnight in order to reduce any unreacted glutaraldehyde (Figure 2.1E). Prior to seeding cells into the scaffolds, all samples (native, collagen coated, or cross-linked) were incubated in mammalian cell culture medium (described below) for 12 hours in a standard tissue culture incubator maintained at 37°C with 5% CO_2 (Figure 2.1F).

2.4.3 Cell culture

C2C12 mouse myoblasts, NIH3T3 mouse fibroblasts and HeLa human epithelial cell lines were used in this study (all obtained from the American Type Culture Collection (ATCC)). Cells were cultured in standard cell culture media (high glucose DMEM (HyClone), supplemented with 10% fetal bovine serum (HyClone), 1% penicillin/streptomycin (HyClone) and 1% amphotericin B (Wisent) at 37°C and 5% CO_2 in T75 flasks (Thermo Scientific). Culture media was exchanged every second day and the cells were passaged at 80% confluence.

2.4.4 In vitro cell culture in cellulose scaffolds

The scaffold seeding procedure took place in 24-well tissue culture plates. Each well was individually coated with polydimethylisiloxane (PDMS) to create a hydrophobic surface in order to prevent the adhesion of cells. A 1:10 solution of curing agent: elastomer (Sylgard 184, Ellsworth

Adhesives) was poured into each well. The PDMS was cured for 2 hours at 80°C, and was allowed to cool to room temperature, then rinsed with PBS. Scaffolds were cut into 0.5x0.5 cm pieces and placed within each well. A 40 μL droplet containing $6x10^6$ cells was carefully formed on top of each scaffold. The samples were placed in the incubator for 6 hours to allow the cells to adhere to the scaffolds. Subsequently, 2 mL of DMEM was added to each well and the samples were incubated for 48 hours. At this point, samples containing mammalian cells were then carefully transferred into new 24-well PDMS-coated tissue culture plates. For continued cell proliferation, the culture media was exchanged every day and scaffolds were moved into new 24-well plates every 2 weeks.

2.4.5 Immunofluorescence staining

The actin cytoskeleton and nucleus of mammalian cells, cultured on glass or within the scaffolds, were stained according to previous protocols [194,195]. Briefly, samples were fixed with 3.5% paraformaldehyde and permeabilized with Triton X-100 at 37°C. Actin was stained with phalloidin conjugated to Alexa Fluor 488 (Invitrogen) and nuclei were stained by labelling the DNA with DAPI (Invitrogen). Samples were then mounted in Vectashield (Vector Labs).

In order to simultaneously stain the cellulose scaffold and mammalian cells, we first fixed the samples as described above, and then washed them with PBS 3 times. To label the apple cell walls, we used an established protocol described previously by Trueunit et al. (2008) [196]. The samples were rinsed with water and incubated in 1% periodic acid (Sigma-Aldrich) at room temperature for 40 minutes. The tissue was rinsed again with water and incubated in Schiff reagent (100 mM

sodium metabisulphite and 0.15 N HCl) with 100 mg/mL propidium iodide (Invitrogen) for 2 hours. The samples were then washed with PBS. To visualize the mammalian cells within the apple tissue, the samples were incubated with a solution of 5 μg/mL wheat germ agglutinin (WGA) 488 (Invitrogen) and 1 μg/mL Hoechst 33342 (Invitrogen) in HBSS (20 mM HEPES at pH 7.4; 120 mM NaCl; 5.3 mM KCl; 0.8 mM $MgSO_4$; 1.8 mM $CaCl_2$; and 11.1 mM dextrose). WGA and Hoechst 33342 are live cell dyes that label the mammalian cell membrane and nucleus, respectively. The samples were then transferred onto microscope slides and mounted in a chloral hydrate solution (4 g chloral hydrate, 1 mL glycerol, and 2 mL water). Slides were kept overnight at room temperature in a closed environment to prevent dehydration. The samples were then placed in PBS until ready for imaging.

We also labelled samples to test for long-term mammalian cell viability. In these cases, cells were maintained in culture for 12 weeks and then stained with a solution of 1 μg/mL Hoechst 33342, which stains the nuclei of all cells, and 1μg/mL Propidium iodide (PI), which is cell membrane impermeable and will only stain the nucleic acids of apoptotic or necrotic cells. Samples were then fixed with 3.5% paraformaldehyde as above and then submerged in PBS until ready for confocal imaging. In order to quantify the number of viable cells we prepared and stained n=3 samples. Individual Hoechst-positive and PI-positive cells were automatically counted using the particle analyzer function on ImageJ

2.4.6 Microscopy

Confocal imaging was performed on an A1R high speed laser scanning confocal system on a TiE inverted optical microscope platform (Nikon, Canada) with appropriate laser lines and filter sets. Transmitted light images were acquired on an inverted TiE microscope (Nikon, Canada) with phase contrast optics. Images were analyzed using ImageJ open access software (http://rsbweb.nih.gov/ij/). Brightness and contrast adjustments were the only manipulations performed to images.

2.4.7 Scanning Electron Microscopy

Scaffolds containing mammalian cells were first fixed with 3.5% paraformaldehyde as presented above, and then gently washed repeatedly with PBS. The samples were then dehydrated through successive gradients of ethanol (50%, 70%, 95% and 100%) and dried within a lyophilizer. Samples were then gold-coated at a current of 15 mA for 3 minutes with a Hitachi E-1010 ion sputter device. SEM imaging was conducted at voltages ranging from 2.00-10.0 kV on a JEOL JSM-7500F FESEM.

2.4.8 Atomic force microscopy (AFM)

AFM was employed to measure the mechanical properties of the native, collagen functionalized, or chemically cross-linked (n = 3 in each case) cellulose scaffolds. In all cases, tip-less PNP-TR-TL (Nano world) AFM cantilevers were modified with a 10 µm polystyrene bead (Fluka) using an optical adhesive (Norland), cured in a UV cross-linker (Spectroline Select Series). Cantilevers possessed an average spring constant of 37 ± 5 pN/nm as determined using the thermal fluctuation method[197,198]. Local mechanical properties were measured by 5-15 force-indentation curves

collected at 10-15 randomly chosen locations at a rate of 1 Hz. A total of n = 200 measurements were acquired for each sample. PUNIAS software was used to fit the first 200 nm of indentation to the Hertz model for a spherical indenter, using a Poisson ratio of 0.5[194,198,199].

2.4.9 Statistical Analyses

All presented values are the average ± standard deviation. Where applicable, we assessed statistical significance by performing a two-sample student's t-test ($\alpha < 0.05$).

2.5 Results

2.5.1 Preparation of cellulose scaffolds

As described in the Materials and Methods section, apple hypanthium tissue was cut to uniform size and decellularized following established protocols (Figure 2.1) [3]. Hypanthium tissue was employed as it is rich in cellulose and contains very few cells [200,201]. Decellularization protocols were employed to ensure the complete removal of any remaining plant cells, nucleic acids and biomacromolecules. After processing the samples, a highly porous structure is observed with phase contrast microscopy (Figure 2.2A). The apple tissue has evolved as a very porous structure, with cell wall cavities observed throughout the sample, allowing for facilitated nutrient transfer throughout. Cellulose scaffolds were then fixed and dehydrated for SEM imaging. Samples were cut horizontally down the mid-section revealing the interior surface. A highly porous and relatively robust scaffold is clearly observed (Figure 2.2B). In all cases, the cellulose scaffold was the only apparent feature observed in all images, as no other identifiable structures were witnessed (i.e. cellular organelles or otherwise).

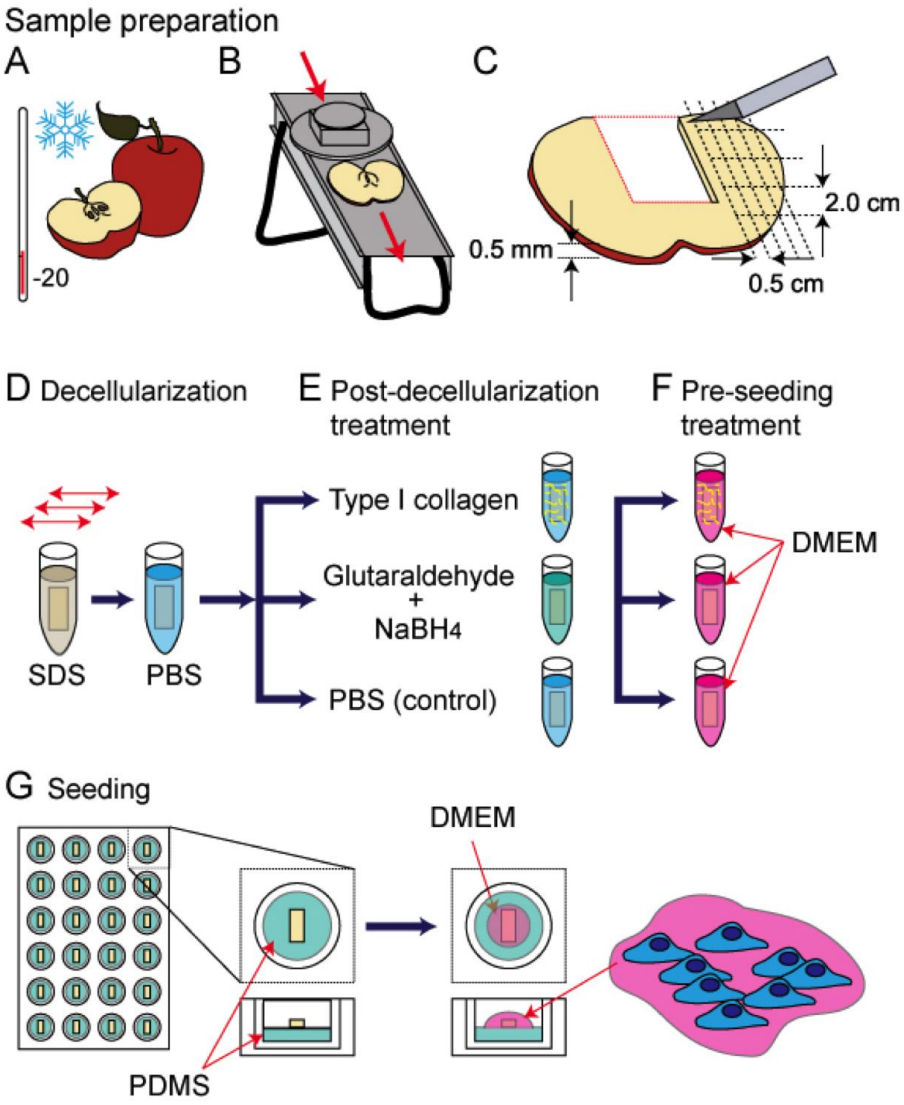

Figure 2.1. A cartoon schematic representing the apple tissue decellularization and mammalian cell seeding protocol used in this study.
a) McIntosh Red apples were exposed to −20°C temperatures for a max duration of 5 minutes, to increase the firmness of the outer apple hypanthium tissue. **b**) Uniform 1.2±0.1 mm thick slices of the apples were obtained using a mandolin slicer. Slices containing any of the ovary core of the apple were removed. **c**) The apple slices were cut into uniform 2.0 by 0.5 cm segments that were placed in individual microcentrifuge tubes. **d**) A 0.5% SDS solution was added to the microcentrifuge tubes and placed on a shaker for 12 hours at room temperature. The scaffolds were then rinsed repeatedly with PBS and allowed to incubate in a PBS solution with 1% streptomycin/penicillin and 1% amphotericin B for 6 hours at room temperature. **e**) The scaffolds were then coated with Type 1 collagen, chemically cross-linked with glutaraldehyde or incubated in PBS. F) All the samples were then incubated in a mammalian cell culture medium (DMEM) for 12 hours in a standard tissue culture incubator maintained at 37°C and 5% CO2. G) The scaffolds were placed in PDMS coated 24 well plates and a 40 µL cell suspension was placed on each. After 6 hours in the incubator, the wells were filled with DMEM and cells cultured for up to 12 weeks.

2.5.2 Mechanical properties of native and modified cellulose scaffolds

We employed two post-decellularization functionalization protocols in order to examine the ease of modification of the mechanical properties of these cellulose scaffolds. The two modifications included functionalization of the scaffold with type I collagen, or chemically cross-linking of the scaffold with glutaraldehyde. These modifications allowed us to control the biochemical environment of the scaffolds, and alter their mechanical properties. AFM was used to quantify the local elasticity of the scaffolds in response to each treatment. We measured the elasticity of four specific samples: untreated (native), decellularized (SDS), decellularized and collagen functionalized (SDS+Coll), and finally decellularized and glutaraldehyde cross-linked (SDS+GA) tissue. Native tissue, SDS, SDS+Coll and SDS+GA scaffolds possessed an elasticity of 0.9 ± 0.1 kPa, 1.1 ± 0.1 kPa, 2.2 ± 0.2 kPa and 4.1 ± 0.3 kPa, respectively (Figure. 2.3A). The native and SDS scaffolds did not display any significant difference in mechanical properties ($p>0.05$). Both the SDS+Coll and SDS+GA scaffolds displayed a significant increase in elasticity compared to the native and decellularized scaffolds ($p<0.001$). These results demonstrate that the local elasticity of the scaffolds can clearly be controlled to fall within a range which mimics some mammalian tissues [202,203]. Finally, C2C12 cells were seeded into different scaffold preparations (SDS, SDS+Coll and SDS+GA, n = 3 in each case) and cultured for 2 weeks (Figure 2.3B-D). Phase-contrast microscopy revealed the presence of mammalian cells in each of the scaffolds compared to the cellulose scaffold presented in Figure 2.3B The images shown are representative of the n = 3 scaffolds prepared in each case.

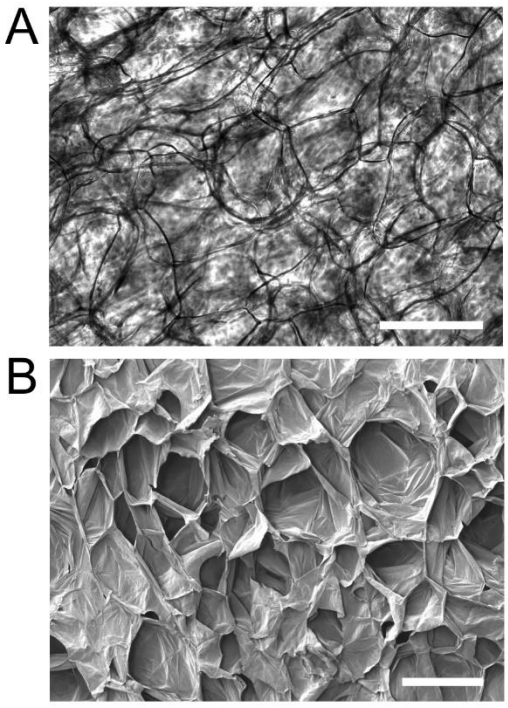

Figure 2.2. Decellularized cellulose scaffolds. a) Phase contrast image of cellulose cell wall structure in a decellularized apple tissue sample. The dark lines correspond to distinct cellulose structures which form a three-dimensional matrix. **b**) SEM image of a similar cellulose scaffold revealing its three-dimensional nature and large cavities. Scale bar=200 μm

2.5.3 Mammalian cell culture in native, collagen functionalized, and chemically cross-linked cellulose scaffolds

To test the ability of the cellulose scaffolds for supporting 3D mammalian cell culture, we examined the proliferation of mouse C2C12 myoblasts, mouse NIH3T3 fibroblasts and human HeLa epithelial cells within the native, collagen functionalized, or chemically cross-linked cellulose scaffolds (n = 3 for each case). In all cases, the proliferation of cells was similar. After 4 weeks in culture, immunofluorescent images were generated for every sample to selectively visualize the mammalian cells within the apple cell wall. A distinct cell wall structure was observed for all conditions, seen as a uniform thin red structure forming individual cavities of consistent size (see Figure 2.4). Interestingly, similar observations were made of the cellulose structure in the

SEM images (Figure 2.2b). The cell membranes (green) and nucleus (blue) of C2C12 myoblasts (Fig. 2.4a), mouse NIH3T3 fibroblasts (Fig. 2.4b) and human HeLa epithelial cells (Fig. 2.4c) are seen throughout the scaffold in numbers exciding the intial seeding. Taking together this demonstrates that the mammalian cells proliferate in unmodified (Figure 2.4a-c), as well as modified scaffolds (data not shown). Cells were observed to be growing on the surface of the scaffolds.

It was also observed that the majority of cells are in closely interacting aggregates within the individual cell wall cavities. To further examine the proliferation within the cellulose structure, orthogonal views of volume-images were generated. The green (membrane) and blue (nucleus) signals can be seen within the cellulose structure's interior, thus demonstrating that the cells proliferate deep within the scaffolds. Fluorescent signals can be seen up to depths of approximately 120 µm from the surface of the scaffolds. It is important to note that the loss of fluorescence signal coincides with the limit of imaging depth of the confocal microscope. Hence, the actual degree of cell invasion into the scaffold cannot be determined with confocal microscopy alone. To further investigate the degree of cellular invasion into the cellulose scaffolds, we fixed and dehydrated (n = 3) native scaffolds for SEM imaging. The samples were prepared in a way that revealed the interior surface of the cellulose scaffolds. SEM images also reveal that cells can migrate within the scaffolds. In Fig 2.4d, we present images of C2C12 cells that have migrated towards the interior of the sample. Cells are clearly visible within the scaffold (Figure 2.4d) in comparison to SEM of an un-seeded scaffold (Fig. 2.2b). Cells in the scaffold can be seen attached to the cellulose structure, with their morphologies varying between round and spread, consistent with other mammalian cells grown in other natural and synthetic 3D scaffolds [204,205].

Finally, the morphology of the actin cytoskeleton was also examined for all cell types in unmodified cellulose scaffolds (n = 3 for each cell type). In this case, cells were only cultured for 1 week, as the actin cytoskeleton was more easily resolved in lower density samples. All mammalian cell types within the scaffolds displayed clear actin stress fibers, consistent with strongly attached cells, as those demonstrated on solid 2D substrates [194,195,206] (Fig. 2.5). These results demonstrate that the mammalian cells were well-adhered to the cellulose scaffold, rather than simply being physically confined within the scaffold.

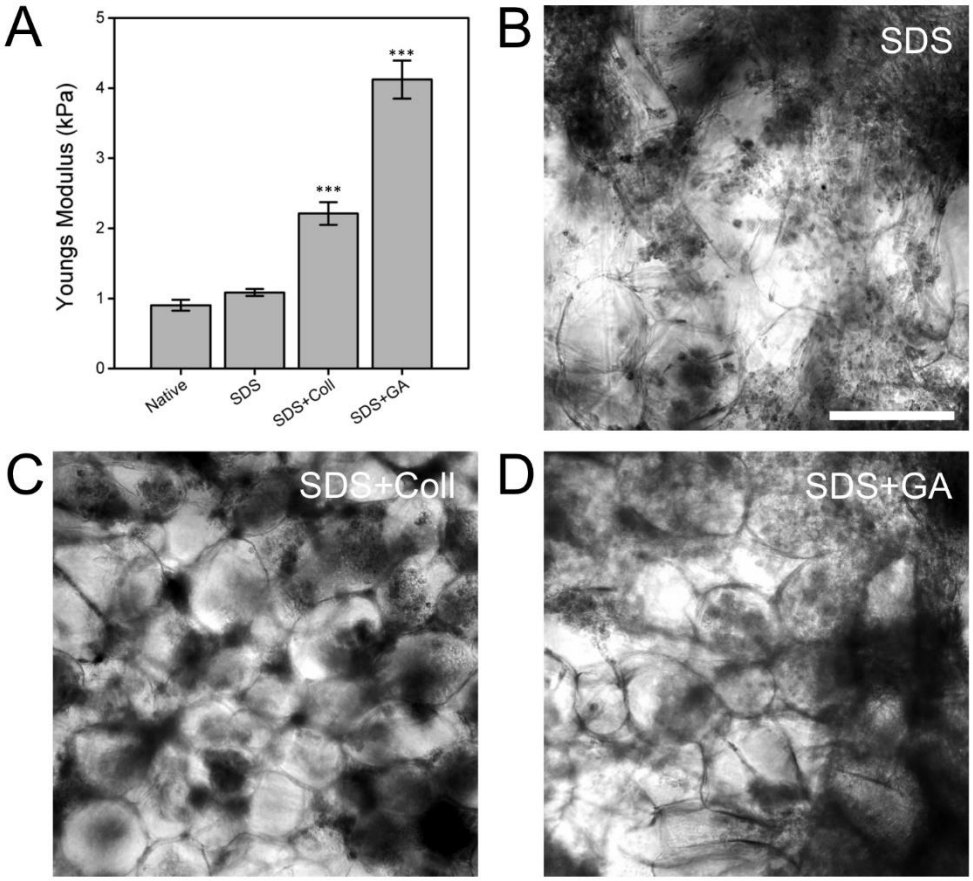

Figure 2.3. The mechanical properties of functionalized cellulose 3D scaffolds and C2C12 myoblast cultured within the 3D cellulose scaffolds. a) The local mechanical elasticity of native tissue, decellularized (SDS), collagen functionalized (SDS+Coll) and glutaraldehyde (SDS+GA) cross-linked cellulose scaffolds. The native tissue and unmodified scaffolds do not display any significant difference in mechanical properties. Both the collagen functionalized and chemically cross-linked scaffolds displayed a significant increase in elasticity compared to the DMEM scaffolds (***=p<0.001). The (**b**) decellularized (SDS), (**c**) Collagen functionalized (SDS+Coll) and (**d**) glutaraldheyde cross-linked (SDS+GA) scaffolds all support the growth of C2C12 cells. Phase contrast images of C2C12 cells after two weeks of growth reveal the presence of cell colonies. Scale bar=200 μm.

2.5.4 Proliferation and Viability

In order to quantitatively assess long-term cell proliferation and viability, confocal images were acquired throughout the cellulose scaffold after 1, 8 and 12 weeks of continuous cell culture. To assess proliferation, confocal volumes of cell nuclei were acquired at random locations on n=3 scaffolds seeded with NIH3T3, C2C12 or HeLa cells. For each cell type, n=3 randomly chosen $1.6x10^6$ μm^2 imaging regions were chosen, and confocal imaging was performed. The imaging depth required to capture all cells in the sample area was observed to change due to the fact that cells were invading deeper into the scaffold over time. Using this data, cells were counted and shown to increase in number by several-fold over a 12-week period (Fig. 2.6a). HeLa and C2C12 cells were observed to increase in number at a similar rate, which was higher than NIH3T3 cells. Regardless, all cell types exhibited a three- to four-fold increase in number over a 12-week period of continuous culture.

We also examined cell viability within these cellulose scaffolds after 12-weeks of continuous culture. Scaffolds (n = 3) were incubated with Propidium iodide and Hoechst 33342 to specifically label apoptotic/necrotic or living cells, respectively (Fig. 2.6b). In all cases, Hoechst labelled all cell nuclei (live and dead) throughout the sample. Conversely, Propidium iodide specifically labelled a minority of dead cells, which were mainly located towards the interior portion of the scaffold. Cell viability was quantified by counting the Hoescht-positive (live) and PI/Hoescht-positive (dead) nuclei of cells. The majority of cells (98 ± 1% of C2C12 cells) cultured on the apple scaffold were Hoechst-positive after 12 weeks in culture (Figure 2.6c), with identical results in the other cell types (data not shown). These results demonstrated a high degree of viability for long-term cultures on the surfaces of these cellulose scaffolds. Orthogonal projections

demonstrated that a small population of apoptotic/necrotic cells were located approximately 120 µm towards the interior of the cellulose scaffold (see Fig. 2.6b). Even in regions of increased cell density there was sufficient porosity within the cellulose scaffold to allow for media/nutrient transfer to the interior of the scaffolds.

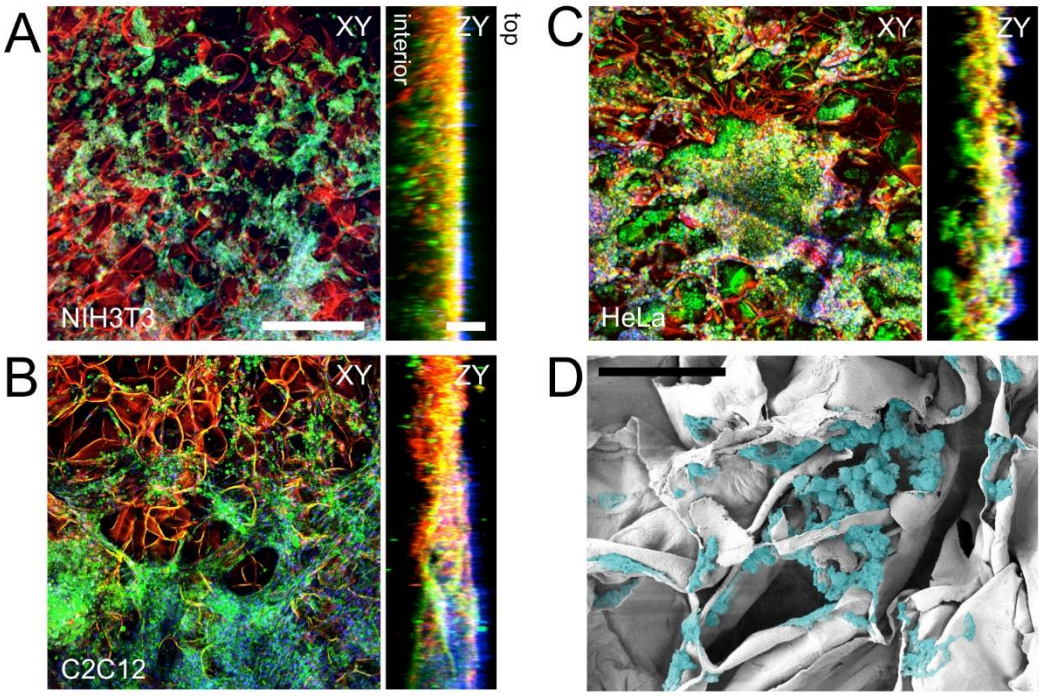

Figure 2.4. Fixed and stained NIH3T3, C2C12 and HeLa cells cultured on 3D cellulose scaffolds. Specific fluorescent staining of (**a**) NIH3T3, (**b**) C2C12 and (**c**) HeLa mammalian cells within the cellulose scaffolds and subsequent laser scanning confocal microscopy reveals the cellulose structure (red), mammalian cell membranes (green) and nuclei (blue). Cells were cultured in these scaffolds for four weeks prior to staining and imaging. Confocal volumes were acquired and projected in the XY and ZY plane. The ZY orthogonal views demonstrate the depth of cell proliferation within the cellulose scaffold. The top and bottom surfaces of the scaffold are indicated. Scale bars: XY=300 µm, ZY=100 µm. **d**) SEM image of a cellulose scaffold cross section after being seeded with C2C12 cells that were allowed to proliferate for four weeks. The cells were digitally colourized in order to increase contrast between the cells and cellulose structure (Scale bar: 50 µm)

2.6 Discussion

Cells in a 3D environment, whether an artificial extracellular matrix or living tissues, often display numerous morphological and biochemical differences compared to cells cultured on a 2D surface [164]. These differences are under intense scrutiny, as many studies have demonstrated the importance of spatial cues within the ECM. For example, geometry and special cues have been shown to affect cell morphology, mRNA signalling, and differentiation [37,40,161,207,208]. Therefore, the use of 3D scaffolds for *in vitro* cell culture is beneficial towards our fundamental understanding of cell biology, and has consequently has many potential applications. The development and use of 3D biocompatible scaffolds does however present several challenges. Biomaterials must be biocompatible, biodegradable, allow for surface modifications, and be cost effective. Two methods of production have emerged. The first of these methods is the use of artificial scaffolds synthesized from (bio)polymers. Artificial scaffolds have the advantage of allowing for exceptional control over the material, allowing for tuning of biochemical and structural properties of the scaffold [209–213]. On the other hand, decellularization has been employed to produce natural 3D scaffolds from existing tissue [168,180,183,192,211–213]. Decellularization employs various reagents to lyse and remove cells from the ECM of a given tissue sample [182,184]. Though this approach lacks fine control over the physical and biochemical properties of the scaffold, it results in an easily obtained, naturally derived, scaffold that has been employed in the creation of functional organs [3,4,183,191,192] .

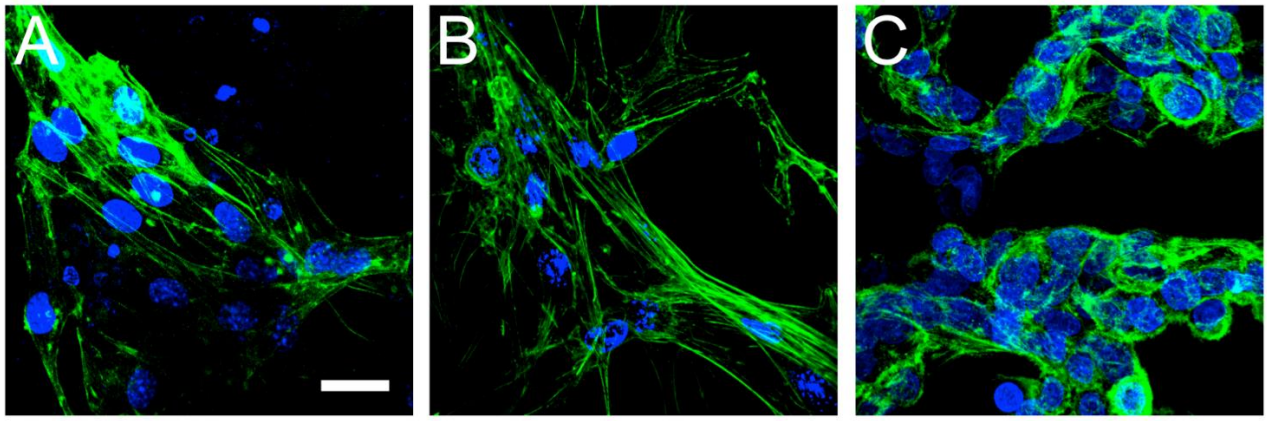

Figure 2.5. Fixed and stained images of cells actin cytoskeleton cultured within the 3D cellulose scaffold. a) NIH3T3,**b**) C2C12 and **c**) HeLa cells were cultured onto the cellulose scaffolds for 2 weeks prior to stained for actin (green) and cell nuclei (blue). (NIH3T3 and C2C12 cells display characteristic actin stress fibres found in cultured cells. HeLa cells also display characteristic actin structures, including fewer prominent stress fibres and a large amount of cortical actin localization. Scale bar=25 μm and applies to all.

Herein, decellularized apple hypanthium tissue is shown to provide several characteristics that are desirable for producing 3D cellular scaffolds. Apple hypanthium is primarily composed of plant cell walls which form a porous network of cavities in which the plant cells reside [214]. This porous environment allows for facilitated transfer of nutrients throughout the tissue. In addition, this environment is also ideal for decellularization as it allows for rapid exchange of detergents, buffers and media without the use of perfusion systems. We were able to rapidly produce decellularized cellulose scaffolds by simply using a detergent solution. Importantly, mouse fibroblast (NIH3T3), mouse muscle myoblast (C2C12) and human epithelial (HeLa) cells were all able to completely invade, proliferate and remain viable after a long term period of culture (12 weeks) within the cellulose scaffolds.

The mechanical and biochemical properties of the ECM are known to play a very important role in governing cellular physiology [37,161,207,208]. The apple hypanthium-derived scaffolds, used in this study, are composed of cellulose that is assembled into microfibrils which are then cross-linked

by hemicellulose[215], and resemble the porous nature of the ECM. Here, using AFM, we demonstrated that the local Young's modulus of the scaffold could be altered through chemical cross-linking or biochemical functionalization. We found that the native and SDS samples displayed no statistical difference in local Young's modulus (p<0.05), demonstrating that SDS treatment did not alter the mechanics of the cellulose structure [181]. Furthermore, it was also observed that scaffolds functionalized with collagen or cross-linked with glutaraldehyde displayed a significant two to four-fold increase in Young's modulus (p<0.001) compared to the native tissue or unfunctionalized decellularized scaffolds. Our results are consistent with previous studies, which demonstrate that collagen functionalization or glutaraldehyde cross-linking tends to increase the Young's modulus of biological materials [216–218]. The ability to tune the cellulose scaffold rigidity is critical as it has been long established that cells preferred matrix with specific rigidities to differentiate and acquire their specific cellular properties [182,184,207,214,215]. Hence, we showed that it is possible to control and modulate the mechanical rigidity of the cellulose scaffold.

Previous studies employing mechanical compression testing of bulk apple samples have reported significantly higher Young's modulus measurements, in the MPa range [219,220], compared to the ones obtained in our study. Their technical approaches measure an elasticity that reflects the forces required to deform all of the cells and cellulose structures within a large region of apple tissue. In contrast, we employed an AFM with a modified cantilever probe using a 10 µm colloid polystyrene bead in order to probe local elasticities. Young's modulus measurements obtained with this approach are reflective of the local deformation of a small microscale region of the cellulose scaffold. Due to the local nature of AFM measurements, the measured Young's modulus more accurately reflects the mechanical properties experienced by the cells. Interestingly, in a recent

study, the local Young's modulus of tomato plant tissue was determined to be in the same order of magnitude of our measurements, ~7-29 kPa [221]. These results were also obtained using AFM and a modified cantilever with an attached 10 µm colloid. Importantly however, under all conditions and for differing Young's moduli, cells were observed to rapidly grow and proliferate within the cellulose scaffolds.

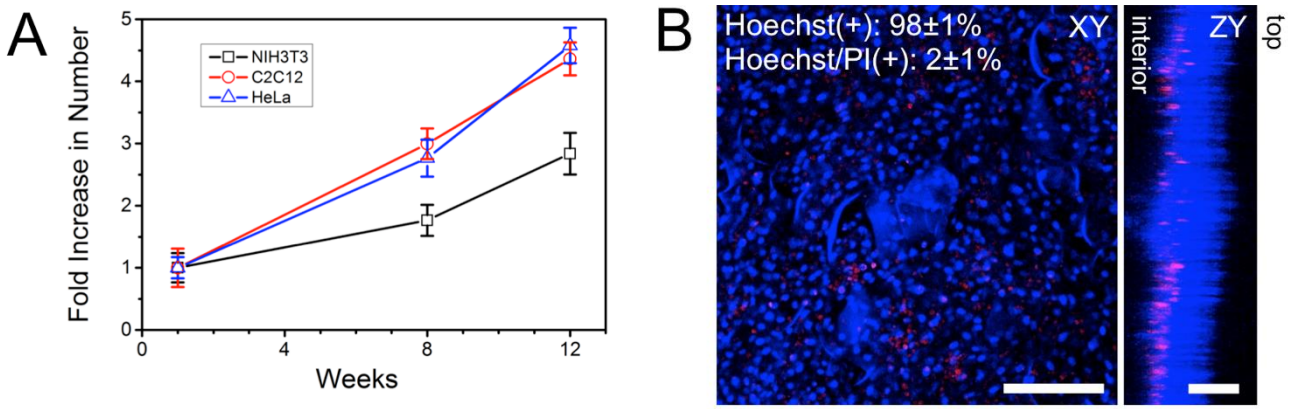

Figure 2.6. Cell proliferation and viability over time. a) NIH3T3, C2C12 and HeLa cells were cultured individually in cellulose n=3 scaffolds for 1, 8 and 2 weeks and then imaged with confocal microscopy after being stained with Hoechst 33342. Cells were counted at each time point and an increase in cell population is clearly observed. **b**) After 12 weeks of culture, C2C12 cells were fixed and stained with Hoechst 33342 (blue: viable cells) and Propidium iodide (PI) (red: apoptotic/necrotic cells). Confocal volumes were acquired and projected in the XY and ZY plane and reveal that cells have proliferated throughout the structure during the 12-week culture. The cells that are apoptotic/necrotic are found in deeper regions of the scaffold. The top and bottom surfaces of the scaffold are indicated. The number of live (Hoechst(+)) and dead (Hoechst/PI(+)) cells were counted and it was found that ~98% of the cells within the scaffold are viable. Data is shown for C2C12 cells, but is similar for NIH3T3 and HeLa cells (data not shown). Scale bar: B=200 µm for XY and 100 µm for ZY.

Employing a staining protocol established by Truernit *et al.* [196], we simultaneously visualized the cellulose structure along with the embedded cells. Confocal microscopy images revealed that all three cell types used in this study were found on the surfaces and the interior cavities within the

cellulose scaffold. Cells were reliably imaged to a depth of approximately 120 μm below the upper surface of the scaffold. In all three cell types we also observed the presence of distinct F-actin stress fibres, which are a morphological characteristic of substrate-adhered cells [195,222,223]. Both fibroblasts and myoblasts cultured in our scaffolds possessed pronounced actin stress fibres, similar to those found in the same cells cultured on 2D substrates [194,195]. HeLa cells were observed to express cortical actin and actin stress fibres. In this case, stress fibres were less prominent than those observed within the fibroblasts and myoblasts, however the observed morphology of the actin cytoskeleton is very consistent with HeLa cells cultured on 2D substrates [223]. The results clearly demonstrate that all cell types studied here were able to proliferate, displaying strong attachment to the surfaces of the cellulose scaffolds.

A constraint of confocal microscopy is the limited depth at which a sample can be imaged. In order to determine whether the mammalian cells migrated towards the interior of the scaffold, the sample was fixed, frozen, and then fractured perpendicular to the top surface. This process allowed us to image the interior of the cellulose scaffold using SEM. In this case, C2C12 cells were cultured on the scaffolds and subsequently imaged. Cells were found deep within the interior of the scaffold and to possess morphologies that were both rounded, as well as flat and spread-out along the cellulose surfaces, analogous to that of myoblasts cells in other 3D environments [224,225]. Interestingly, the cellulose scaffold appears in a collapsed/compressed state in the presence of mammalian cells. When mammalian cells are absent from the scaffold, such morphologies are not observed, confirming that the preparation for SEM imaging is not causing this effect. At present, the origin of this change in morphology is not well understood, however we hypothesize it may be

due to the presence of cellular traction forces, adsorption of serum proteins on the scaffold, or cellular remodelling/degradation of the scaffold.

To quantify proliferation, we counted the number of cells present in the scaffolds after 1,8 and 12 weeks of continuous *in vitro* culture. In all cases, cells were observed to proliferate and increase in number by three to four-fold. However, it was observed that C2C12 and HeLa cells had nearly twice the number of NIH3T3 cells. This is an intriguing result as doubling rate of NIH3T3 cultured on glass (18 hours) is slightly lower than that of HeLa cells (24 hours) [226,227]. Viability assays also reveal that a high percentage of cells remained viable even after 12 weeks of continuous *in vitro* culture. The majority of apoptotic cells were present towards the interior of the cellulose scaffold. This is likely caused by a lack of media turnover, leading to an insufficient supply of nutrients and oxygen, a common phenomenon in 3D culture models [228]. 3D spheroid cell cultures often contain a necrotic core of cells due to an insufficient supply of nutrients and oxygen [228].

Although the results show that cells proliferate and remain viable in the scaffolds, their porosity can have an important influence on the observed results. The high porosity of the scaffolds offers both advantages and disadvantages. The high porosity of the scaffold allows cells to pass through the material without a high degree of confinement. This leads to a low seeding efficiency that can be problematic in some applications (the culture of rare cells, etc.). For example, in this study each scaffold (~1 mm^3 total volume) was initially seeded at a density of ~$6x10^6$ cells/mm^3. However, cell density was lower after 1-week of culture (~$2x10^6$ cells/mm^3) due to the loss of cells during media exchange. Therefore, a large amount of time (12-weeks) is required for the cells to slowly proliferate and invade the entire scaffold. This is not surprising given the issues highlighted above,

and the fact that these mammalian cells are proliferating in a scaffold that is composed largely of cellulose as opposed to ECM proteins. Although there is a slow proliferation, the cell density does approach the levels reported in other biomaterials [3,4,229]. The efficiency of the initial seeding might be improved through further biochemical modification or chemical cross-linking of the scaffolds to increase the binding potential. Future work will investigate scaffold modification to control porosity and improve seeding efficiency. Alternatively, naturally occurring cellulose with lower porosity might be found in other apple species or plant types. Regardless, future studies will examine the use of higher density cellulose scaffolds to increase seeding efficiency, which will lower the time required to fully populate the scaffolds.

In addition, the high porosity of the scaffolds likely leads to an overestimation of cell viability. Dead cells can be easily washed away during media exchange, lowering the observed number of dead cells in the scaffold. Furthermore, the limited depth associated with confocal microscopy will also influence the ability to assay the physiological state of the cells deep within the scaffold. Other viability assays are also impeded by the nature of the cellulose scaffold. In particular, Trypan blue assay is problematic as the dye interacts strongly with the scaffold, which significantly impedes cell counting and quantification.

Although these limitations exist, mammalian cells are clearly able to proliferate, invade and possess an intact actin cytoskeleton within the scaffolds. In all three cases, cells were observed to interact closely with each other and the scaffold in large, long-range networks. Furthermore, theses cellulose scaffolds represent a very low-cost approach to studying the proliferation and invasion of cells in 3D. These cellulose biomaterials are highly complementary with the myriad of

possibilities for the study of 3D cell biology *in vitro*. Cellulose scaffolds are porous enough to allow for efficient nutrient/gas exchange, biocompatible, easily functionalized and their mechanical properties can be controlled.

2.7 Acknowledgments

The authors wish to thank Dr. Yun Liu for assistance with SEM imaging, Mr. Safi Sayeed for generously donating samples for this study and Tristan Matheson assistance with figure preparation.

Chapter 3| *Manuscript*

BIOCOMPATIBILITY OF SUBCUTANEOUSLY IMPLANTED PLANT-DERIVED CELLULOSE BIOMATERIALS

Daniel J. Modulevsky[1,2,*], Charles M. Cuerrier[1,3,*] and Andrew E. Pelling[1-5]

[1]*Centre for Interdisciplinary NanoPhysics, University of Ottawa, Ottawa, Ontario, Canada,*

[2]*Department of Biology, University of Ottawa, Ottawa, Ontario, Canada*

[3]*Department of Physics, University of Ottawa, Ottawa, Ontario, Canada*

[4]*Institute for Science, Society and Policy, University of Ottawa, Ottawa, Ontario, Canada*

[5]*SymbioticA, School of Anatomy, Physiology and Human Biology, University of Western Australia, Perth, WA, 6009*

Submitted February 12, 2016 to PLOS One

Accepted June 7, 2016, DOI:10.1371/journal.pone.0157894 June

- I, Daniel Modulevsky, contributed to the majority of the research work, including the production of the biomaterials, surgeries, animal care, scanning electron microscopy and image acquisition. Charles M. Currier and Andrew E. Pelling were instrumental in the preparation of the first draft and subsequent revisions
- The arrangement of the manuscript has been modified for thesis formatting purposes.

Motivation |

- After demonstrating the *in vitro* biocompatibility of the plant derived biomaterial I hypothesize that the same characteristics that made the plant derived biomaterial a successful 3D culture will translate to an implantable biomaterial in an *in vivo* model.

3.1 Hypothesis and Objectives |

- The stability of the plant derived biomaterials will allow the biomaterial to be dorsally subcutaneously implanted into mice model and remain intact for 8 weeks.
- The inert properties of cellulose will limit the amount of host foreign body response to the implant as well the host organism will not display any symptom of discomfort during the implantation.

- The porosity of the plant derived biomaterials, observed in the previous *in vitro* study, will allow for the host cells and interstitial fluid to infiltrate the biomaterial.
- As demonstrated in the *in vitro* study the porosity of the plant derived biomaterial will limit the observable necrotic core.
- Rat tail collagen (type I) was successfully coated onto the plant derived biomaterial in the previous study, as such, the host organism will respond by depositing extracellular matrix onto the biomaterial while implanted.

3| BIOCOMPATIBILITY OF SUBCUTANEOUSLY IMPLANTED PLANT-DERIVED CELLULOSE BIOMATERIALS

3.2 Abstract

There is intense interest in developing novel biomaterials which support the invasion and proliferation of living cells for potential applications in tissue engineering and regenerative medicine. Decellularization of existing tissues have formed the basis of one major approach to producing 3D scaffolds for such purposes. In this study, we utilize the native hypanthium tissue of apples and a simple preparation methodology to create implantable cellulose scaffolds. To examine biocompatibility, scaffolds were subcutaneously implanted in wild-type, immunocompetent mice (males and females; 6-9 weeks old). Following the implantation, the scaffolds were resected at 1, 4 and 8 weeks and processed for histological analysis (H&E, Masson's Trichrome, anti-CD31 and anti-CD45 antibodies). Histological analysis revealed a characteristic foreign body response to the scaffold 1 week post-implantation. However, the immune response was observed to gradually disappear by 8 weeks post-implantation. By 8 weeks, there was no immune response in the surrounding dermis tissue and active fibroblast migration within the cellulose scaffold was observed. This was concomitant with the deposition of a new collagen extracellular matrix. Furthermore, active blood vessel formation within the scaffold was observed throughout the period of study indicating the pro-angiogenic properties of the native scaffolds. Finally, while the scaffolds retain much of their original shape, they do undergo a slow deformation over the 8-week length of the study. Taken together, our results demonstrate that native cellulose scaffolds are biocompatible and exhibit promising potential as a surgical biomaterial.

3.3 Introduction

The development of novel biomaterials for tissue engineering strategies is currently under intense investigation [24,230,231]. Biomaterials are being developed for the local delivery of therapeutic cells to target tissues [33,232], the regeneration of damaged or diseased tissues [233–236] or the replacement of whole organs [3,188,237–240]. In their most general form, biomaterials provide a three-dimensional (3D) scaffold which attempts to mimic the *in vivo* cellular milieu [3,241]. Approaches have been developed to engineer the mechanical [242–249], structural [250] and biochemical properties [92,210,231,251] of these scaffolds with varying complexity. As well, significant efforts are underway to ensure that such implanted biomaterials are biocompatible and stimulate only minimal immune responses. The efforts in biomaterials research is being driven by the significant need for replacement organs and tissues. With an aging population, the gap between patients waiting for organ transplants and available donor organs is rapidly increasing [252]. While clinical applications of biomaterials have been somewhat limited, physicians have successfully utilized synthetic biomaterials to treat various damaged tissues and structures, such as skin, gum, cartilage, and bone [253–258].

Biomaterial scaffolds can take several forms such as powders, gels, membranes, and pastes [24,230]. Such polymer or hydrogel formulations can be moulded or 3D-printed to produce forms that are of therapeutic values [259–261]. An alternative approach to these synthetic strategies is whole organ decellularization [3,188,237,239–241]. Indeed, it has been shown that it is possible to dissociate the cells from a donated organ, leaving behind the naturally occurring scaffold matrix, commonly referred as a ghost organs [3]. The ghost organs lack any of the cells from the donor and can be subsequently cultured with cells derived from the patient or another source. Such approaches have already been utilized to repair and replace defective tissues [262–264]. In the past several years, many body parts

have been created using synthetic and decellularization approaches, including the urethra, vaginal, ear, nose, heart, kidney, bladder, and neurological tissues [3,192,260,261,265–268].

However, these approaches are not without some disadvantages [269]. Synthetic techniques can require animal products and decellularization strategies still require donor tissues and organs. There has also been intense investigation into the development of resorbable biomaterials [270]. In these cases, the aim is to provide the body with a temporary 3D scaffold onto which healthy tissues can form. After several week or months, the implanted scaffold will be resorbed leaving behind a completely natural healthy tissue [14,251,271]. Although this is an ideal approach, many non-resorbable biomaterials (ceramic, titanium) have been successfully employed in clinical settings and play a major role in numerous therapies [270,272–276]. Significantly, resorbable biomaterials suffer from the fact that regenerated tissues often collapse and become deformed due to the loss of structure [277–281]. For example, for several decades, research on ear reconstruction from engineered cartilage has shown that biomaterial implants eventually collapse and become deformed as the implanted scaffolds break down and resorb [282]. However, recent successful approaches have relied on the use of resorbable collagen scaffolds embedded with permanent titanium wire supports [273,283,284]. Therefore, the need for non-resorbable yet biocompatible scaffolds persists in the field of tissue and organ engineering.

Recent complementary approaches have utilized scaffolding materials that are not derived from human organ donors or animal products. Namely, various forms of cellulose have been shown to have utility in both *in vitro* and *in vivo* studies [72,169,175,177,178,285]. Cellulose is abundant in nature, is easily produced and sourced, can be chemically modified to control surface biochemistry and produced as hydrogels with tuneable porosity and mechanical properties [67,74,160,178,286–288].

Moreover, nanocrystalline, nanofibrillar and bacterial cellulose constructs and hydrogels also have been shown to support the proliferation and invasion of mammalian cells *in vitro* and *in vivo* with high biocompatibility [289–294]. In our recent work, we developed an orthogonal, yet complementary, approach to organ decellularization and synthetic cellulose strategies. We developed a highly robust and cost effective strategy for producing cellulose biomaterials from decellularized apple hypanthium tissue [92]. The scaffolds required no further complex processing as is often the case in the production of nanocrystalline, nanofibrillar and bacterial cellulose constructs. The cellulose scaffolds were employed for *in vitro* 3D culture of NIH3T3 fibroblasts, mouse C2C12 muscle myoblasts and human HeLa epithelial cells. Our previous work revealed that these cells could adhere, invade and proliferate within the cellulose scaffolds and retain high viability even after 12 continuous weeks of culture.

Our previous work opens the question of *in vivo* biocompatibility [92]. Therefore, the objective of this study is to characterize the response of the body to apple-derived cellulose scaffolds. Macroscopic (~25 mm^3) cell-free cellulose biomaterials were produced and subcutaneously implanted in mouse model for 1, 4 and 8 weeks. Here, we assess the immunological response of immunocompetent mice, deposition of extracellular matrix on the scaffolds and evidence of angiogenesis (vascularization) in the implanted cellulose biomaterials. Notably, although a foreign body response was observed immediately post-implantation, as expected for a surgical procedure, by the completion of the study, only a low immunological response was observed with no fatalities or noticeable infections whatsoever in all animal groups. Surrounding cells were also found to invade the scaffold, mainly activated fibroblasts, and deposit a new extracellular matrix. As well, the scaffold itself was able to retain much of its original shape and structure over the 8-week study. Importantly, the scaffolds clearly had a pro-angiogenic effect, resulting in the growth of functional

blood vessels throughout the implanted biomaterial. Taken together, our work demonstrates that we can easily produce 3D cellulose scaffolds that are biocompatible, becoming vascularized and integrated into surrounding healthy tissues.

3.4 Material and Methods

3.4.1 Animals

All experimental procedures were approved by the Animal Care and Use Committee of the University of Ottawa. Wild-type C57BL/10ScSnJ mice (males and females; 6-9 weeks old; n= 7 mice for each group) were purchased from The Jackson Laboratory (Bar Harbor, Maine, USA) and bred in our facilities. All animals were kept at constant room temperature (±22°C) and humidity (~52%). They were fed a normal chow diet and were kept under a controlled 12 hours light/dark cycle.

3.4.2 Cellulose scaffold preparation

As described previously [92], McIntosh Red apples (Canada Fancy) were stored at 4°C in the dark for a maximum of two weeks. In order to prepare apple sections, the fruit was cut with a mandolin slicer to a uniform thickness of 1.14±0.08mm, measured with a Vernier caliper. Only the outer (hypanthium) tissue of the apple was used. Slices containing visible ovary-core tissue were not used. The slices were then cut parallel to the direction of the apple pedicel into squares segments of 5.14±0.21mm in length and with an area of 26.14±1.76mm^2. Apple tissue was then decellularized by using a well-established protocol [3] for removing cellular material and DNA from tissue samples while leaving behind an intact and three-dimensional scaffold. Individual apple tissue samples were placed in sterilized 2.5ml microcentrifuge tubes and 2ml of 0.1% sodium

dodecyl sulphate (SDS; Sigma-Aldrich) solution was added to each tube. Samples were shaken for 48 hours at 180 RPM at room temperature. The resultant cellulose scaffolds were then transferred into new sterile microcentrifuge tubes, washed and incubated for 12 hours in PBS (Sigma-Aldrich). To sterilize the cellulose scaffold, they were incubated in 70% ethanol for 1 hour and then washed 12 times with PBS. The samples were then maintained in PBS with 1% streptomycin/penicillin (HyClone) and 1% amphotericin B (Wisent, QC, Canada). At this point, the samples were immediately used or stored at 4°C for no more than 2 weeks.

3.4.3 Cellulose implantation

The mice were anesthetized using 2% Isoflurane USP-PPC (Pharmaceutical partners of Canada, Richmond, ON, Canada) and their eyes protected by the application of ophthalmic liquid gel (Alco Canada In., ON, Canada). To prepare the surgery sites, mouse back hairs were shaved and the skins were cleaned and sterilized using ENDURE 400 Scrub-Stat4 Surgical Scrub (chlorhexidine gluconate, 4% solution; Ecolab Inc., Minnesota, USA) and Soluprep (2% w/v chlorhexidine and 70% v/v isopropyl alcohol; 3M Canada, London, ON, Canada). To maintained animal hydration, 1ml of 0.9% sodium chloride solution was administrated subcutaneously (s.c.) (Hospira, Montréal, QC, Canada). During the surgical procedures, we applied all sterility measures requested for survival surgeries. To implant the scaffolds, two 8mm incisions were made on the dorsal section of each mouse (upper and lower). Two cellulose scaffold samples were separately and independently implanted on each mouse. The incisions were then sutured using Surgipro II monofilament polypropylene 6-0 (Covidien, Massachusetts, USA) and transdermal bupivicaine 2% (as monohydrate; Chiron Compounding Pharmacy Inc., Guelph, ON, Canada) was topically applied on surgery sites to prevent infection. Also, buprenorphine (as HCL) (0.03mg/ml; Chiron

Compounding Pharmacy Inc. Guelph, ON, Canada) was administrated s.c. as a pain reliever. All animals were then carefully monitored for the next 3 days by animal care services and received repetitions of the same pharmacological treatments.

3.4.4 Scaffold resections

At 1, 4 and 8 weeks after scaffold implantation, the mice were euthanized using CO_2 inhalation. After blood collection, the dorsal skin was carefully resected and immediately immersed in PBS solution. The skin sections containing cellulose scaffolds were then photographed, cut and fixed in 10% formalin for at least 48 hours. The samples were then kept in 70% ethanol before being embedded in paraffin by the PALM Histology Core Facility of the University of Ottawa.

3.4.5 Histological analysis

Serial 5µm thick sections were cut, beginning at 1 mm inside the cellulose scaffold, and stained with hematoxylin and eosin (H&E) and Masson's trichrome. For immunocytochemistry, heat induced epitope retrieval was performed at 110°C for 12 min with citrate buffer (pH 6.0). Anti-CD31/PECAM1 (1:100; Novus Biologicals, NB100-2284, Oakville, ON, Canada), anti-alpha smooth muscle actin (1:1000, ab5694, abcam, Toronto, ON, Canada) and anti-CD45 (1:3000; ab10558, abcam, Toronto, ON, Canada) primary antibodies were incubated for an hour at room temperature. Blocking reagent (Background Sniper, Biocare, Medical, Concorde, CA, USA) and detection system MACH 4 (Biocare Medical, Concord, CA, USA) were applied according to company specifications. For the evaluation of cell infiltration, extracellular matrix deposition and vascularisation (angiogenesis), micrographs were captured using Zeiss MIRAX MIDI Slide

Scanner (Zeiss, Toronto, Canada) equipped with 40x objective and analysed using Pannoramic Viewer (3DHISTECH Ltd., Budapest, Hungary) and ImageJ software. The scoring of inflammation was evaluated by a pathologist. The scoring was subjectively assigned by qualitative analysis of the magnitude of the total foreign response as well, the cell population proportions within the foreign response.

3.4.6 Scanning electron microscopy (SEM)

The structure of cellulose was studied using a scanning electron microscopy. Globally, scaffolds were dehydrated through successive gradients of ethanol (50%, 70%, 95% and 100%). Samples were then gold-coated at a current of 15mA for 3 minutes with a Hitachi E-1010 ion sputter device. SEM imaging was conducted at voltages ranging from 2.00–10.0 kV on a JSM-7500F Field Emission SEM (JEOL, Peabody, MA, USA).

3.4.7 Statistical analysis

All values reported here are the average ± standard deviations. Statistical analyses were performed with one-way ANOVA by using SigmaStat 3.5 software (Dundas Software Ltd, Germany). A value of $p < 0.05$ was considered statistically significant.

3.5 Results

3.5.1 Scaffold Preparation

Cellulose scaffolds were prepared from apple tissue using a modified decellularization technique we have previously described [92]. All scaffolds were cut to a size of 5.14±0.21 x 5.14±0.21 x 1.14±0.08mm (Fig 3.1a), decellularized and prepared for implantation (Fig 3.1b). The scaffolds appear translucent after decellularization due to the loss of all plant cellular material and debris. The removal of apple cells was also confirmed with histological observation (Fig 3.1c) and scanning electron microscopy (Fig 3.1d). Analysis of the histological images and the measurement of the average wall thickness (4.04±1.4μm) reveal that the cellulose scaffolds is highly porous, capable of being easily invaded by nearby cells and results in an acellular cellulose scaffold that maintains its shape.

3.5.2 Implantation of Cellulose Scaffolds

Two independent skin incisions (8mm) were produced on the back of each mouse to create small pouches for the biomaterial implantation (Fig 3.2a). One cellulose scaffold (Fig 3.2b) was implanted in each subcutaneous pouch. Throughout the study, there were no cases of mice exhibiting any pain behaviour that may have been induced by the cellulose scaffold implantation and none of them have displaying any symptoms of visible inflammation or infection. The cellulose scaffolds were resected at 1 week, 4 weeks and 8 weeks after their implantation and were photographed to measure the change in scaffold dimensions (Fig 3.2d-f). At all-time points, healthy tissue can be observed surrounding the cellulose scaffold with the presence of blood vessels, that are proximal or in direct contact, and the scaffolds retain their square shape. The pre-

implantation scaffold had an area of 26.3±1.98mm^2 and it was observed to slowly decrease as function of their implantation time base on the scaffold area that is visible to the naked eye on the skin (Fig 3.2g). At 8 weeks post-implantation, the scaffold dimensions reach a near plateau measurement of 13.82±3.88mm^2 demonstrating an approximate 12mm^2 (48%) change over the course of this study.

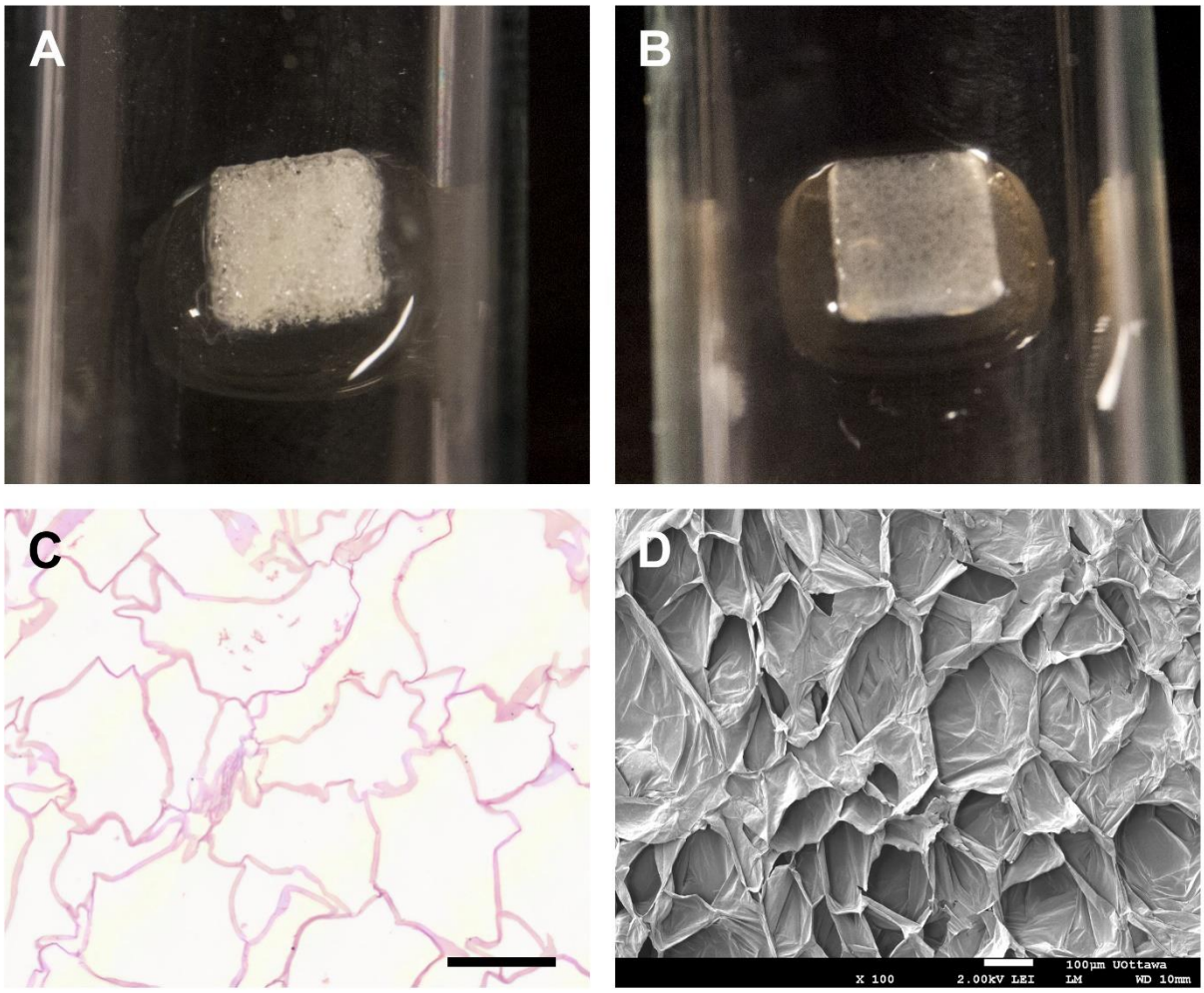

Figure 3.1 Cellulose scaffold preparation. Macroscopic appearance of a freshly cut apple hypanthium tissue (**a**) and the translucent cellulose scaffold biomaterial post-decellularization and absent of all native apple cells or cell debris (**b**). H&E staining of cross sectioned decellularized cellulose scaffold (**c**). The cell walls thickness and the absence of native apple cells following decellularization are shown. The 3D acellular and highly porous cellulose scaffold architecture is clearly revealed by scanning electron microscopy (**d**). Scale bar: **a-b** = 2mm, **c-d** = 100µm.

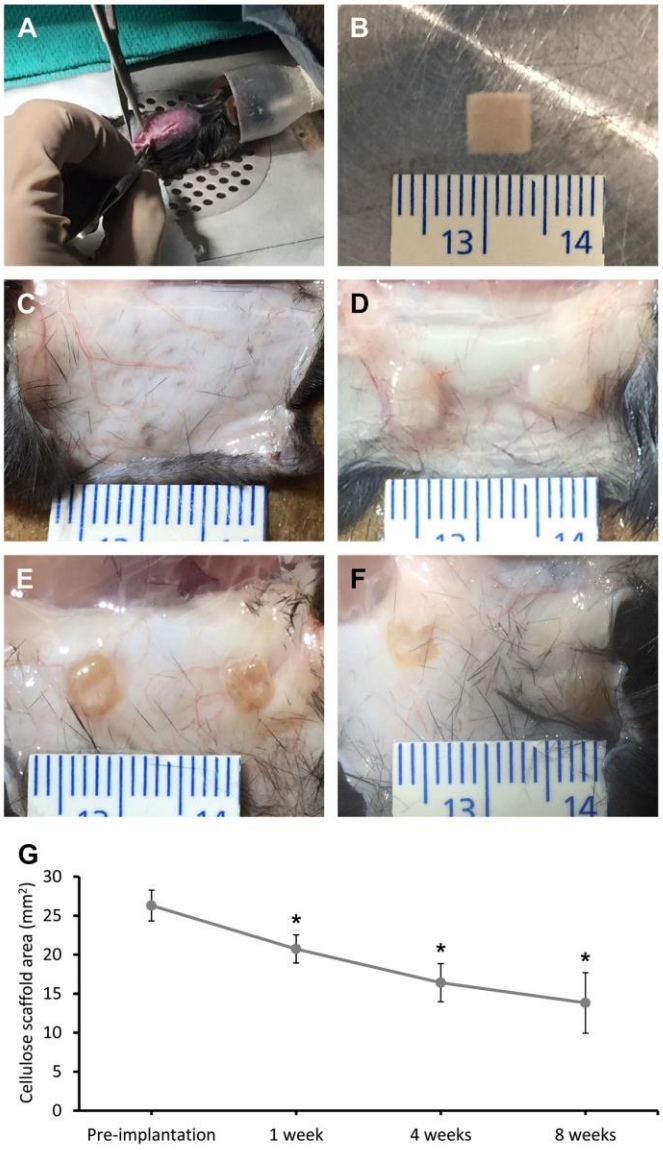

Figure 3.2 Cellulose scaffolds implantation and resection. The subcutaneous implantations of cellulose scaffolds biomaterial were performed on the dorsal region of a C57BL/10ScSnJ mouse model by small skin incisions (8 mm) (**a**). Each implant was measured before their implantation for scaffold area comparison (**b**). Cellulose scaffolds were resected at 1 week (**d**), 4 weeks (**e**) and 8 weeks (**f**) after the surgeries and macroscopic pictures were taken (control skin in **c**). The changes in cellulose scaffold surface area over time are presented (**g**). The pre-implantation scaffold had an area of 26.30±1.98mm^2. Following the implantation, the area of the scaffold declined to 20.74±1.80mm^2 after 1 week, 16.41±2.44mm^2 after 4 weeks and 13.82±3.88mm^2 after 8 weeks. The surface area of the cellulose scaffold has a significant decrease of about 12mm^2 (48%) after 8 weeks implantation (* = P<0.001; n= 12-14).

3.5.3 Biocompatibility and cell infiltration in plant derived cellulose scaffolds

Scaffold biocompatibility and cell infiltration was examined with H&E staining of fixed cellulose scaffolds at 1, 4 and 8 weeks following their implantation (Fig 3.3). The global views of longitudinal section of representative cellulose scaffolds are shown in Fig 3.3a-c. The scaffolds are implanted under the muscular layer of the dermis. Interstitial fluids, stained in pink, can be seen throughout the implanted scaffold, in contrast to a non-implanted scaffold (see Fig 3.1c), highlighting their high porosity and permeability. Within the global view it was observed that the scaffold maintains its general shape throughout the study. In Fig 3.3d-f, a magnified section of the perimeter of the scaffold is shown at each post-implantation time points. At 1 week, the dermis tissue surrounding implant displays symptoms of an acute moderate to severe immune response (qualitative study performed by a pathologist) (Fig 3.3d). As well a dense layer of cells can be seen infiltrating into the cellulose scaffolds. The population of cells within the scaffold at 1 week consist mainly of granulocytes, specifically; polymorphonuclear (PMN) and eosinophils (Fig 3.3d). There is also a population of dead cells and apparent cell debris. Importantly, all of these observations are completely consistent with an expected acute foreign body reaction that follows implantation [295–297]. At the 4 week point we observed a stark difference in both the surrounding epidermis tissue and in the cell population migrating into the cellulose scaffold (Fig 3.3e). The epidermis tissue surrounding the cellulose scaffold has a decreased immune response, now scored as mild to low. The population of cells within the epidermis surrounding scaffolds now contain higher levels of macrophages and lymphocytes (Fig 3.3e). This is an anticipated characteristic of the foreign body reaction to an implanted biomaterial, demonstrating the scaffold cleaning process [295–297]. There is also an increase in the population of multinucleated cells within the interior of the scaffold as part of an inflammatory response (Fig 3.3e). Finally, 8 weeks post-implantation, the immune response

apparent at 1 and 4 weeks has completely disappeared (Fig 3.3f), with the epidermis tissue now appearing normal. In fact, the epidermis tissue in contact with the cellulose scaffold contains the same structures as normal epidermis tissue. In the cellulose scaffold perimeter there is now a lower density of cells due to the decreased inflammation and notably, there are no fragmented dead cells present. Instead, the population of cells now contain an elevated level of macrophages, multinucleated cells and active fibroblasts. The active fibroblasts (appearing spindle shaped), can be observed migrating from the surrounding epidermis into the cellulose scaffold. In fact, fibroblasts were found throughout the cellulose scaffold. These results demonstrate that by 8 weeks post-implantation the cellulose scaffold has been accepted by the host. In parallel with the H&E inflammation analysis, we performed anti-CD45 staining to evaluate the level of inflammation throughout the scaffold and surrounding dermis tissue (Fig 3.3 g-i). It is clear that the inflammation throughout the dermis and within the scaffold is elevated after 1 week. However, the amount of leukocytes significantly decreases in the surrounding dermis and scaffold over the implantation time reaching a near basal level at 8 weeks.

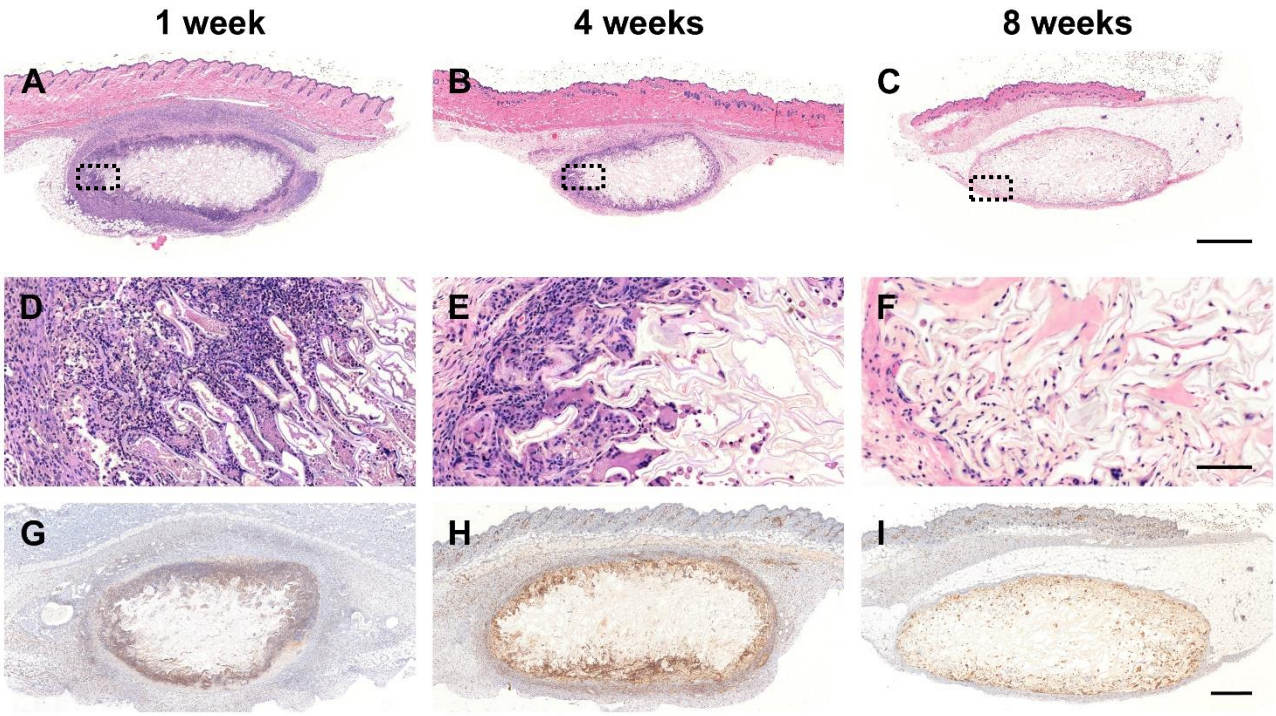

Figure 3.3 Biocompatibility and cell infiltration. Cross sections of representative cellulose scaffolds stained with H&E and anti-CD45. These global view show the acute moderate-severe anticipated foreign body reaction at 1 week (**a**), the mild chronic immune and subsequent cleaning processes at 4 weeks (**b**) and finally, the cellulose scaffold assimilated into the native mouse tissue at 8 weeks (**c**). Higher magnification regions of interest allow the observation of all the cell type population within biomaterial assimilation processes. (**d-f**) At 1 week, we can observe populations of granulocytes, specifically; polymorphonuclear (PMN) and eosinophils that characterize the acute moderate to severe immune response, a normal reaction to implantation procedures (**d**). At 4 weeks, a decreased immune response can be observed (mild to low immune response) and the population of cells within the epidermis surrounding scaffolds now contain higher levels of monocytes and lymphocytes characterizing chronic response (**e**). Finally, at 8 weeks, the immune response has completely resorbed with the epidermis tissue now appearing normal. The immune response observed with H&E staining is confirmed using anti-CD45 antibody, a well known markers of leukocytes (**g-i**). The population of cells within the scaffold are now mainly macrophages, multinucleated cells and active fibroblasts. Scale bars: **a-c** = 1mm, **d-f** = 100µm and **g-i** = 500µm.

3.5.4 Extracellular Matrix Deposition in the Cellulose Scaffolds

The presence of active fibroblasts led us to question if the cellulose scaffold was acting as a substrate for the deposition of new extracellular matrix. This was determined using Masson's Trichrome staining of fixed cellulose scaffolds slides at each time point following implantation (Fig 3.4). At 1 week post-implantation, the histological study shows the absence of collagen structures inside the collagen scaffold (Fig 3.4a, d, and g). As fibroblast cells invade the scaffold, as seen with H&E staining and confirmed by anti-alpha smooth muscle actin staining (data not shown), collagen deposits inside the cellulose scaffold can be observed after 4 weeks (Fig 3.4b, e, and h). At 8 weeks (Fig 3.4c, f and i) the collagen network is clearly visible inside the cavities of the cellulose scaffold. The complexity of the deposited collagen network is highlighted in Fig 3.4i, where we can detect individual collagen fibers within the collagen matrix. This is in contrast to the characteristic high density, thick, cable-like organization of collagen found in scar tissue.

3.5.5 Vascularization of the Cellulose Scaffolds

Capillaries ranging from 8 to 25μm were also identified within the scaffolds as early as 1 week post-implantation. At 4 week and 8 week post implantation, blood vessels and capillaries can be observed extensively within the scaffold and the surrounding dermal tissue. We observed blood vessels presence on the cellulose scaffold and in surrounding dermis in the macroscopic photos taken during the resection (Fig 3.5a). Multiple cross sections of blood vessels, with the presence of red blood cells (RBCs), are identified within 4 weeks of scaffold implantations (Fig 3.5b; H&E stain). The same results are obtained 8 weeks after implantation where capillaries with RBC and endothelial cells are clearly seen (Fig 3.5c; Masson's richrome). All results on blood vessels formation were also confirmed with anti-CD31 staining to identify endothelial cells in the scaffold (Fig 3.5d).

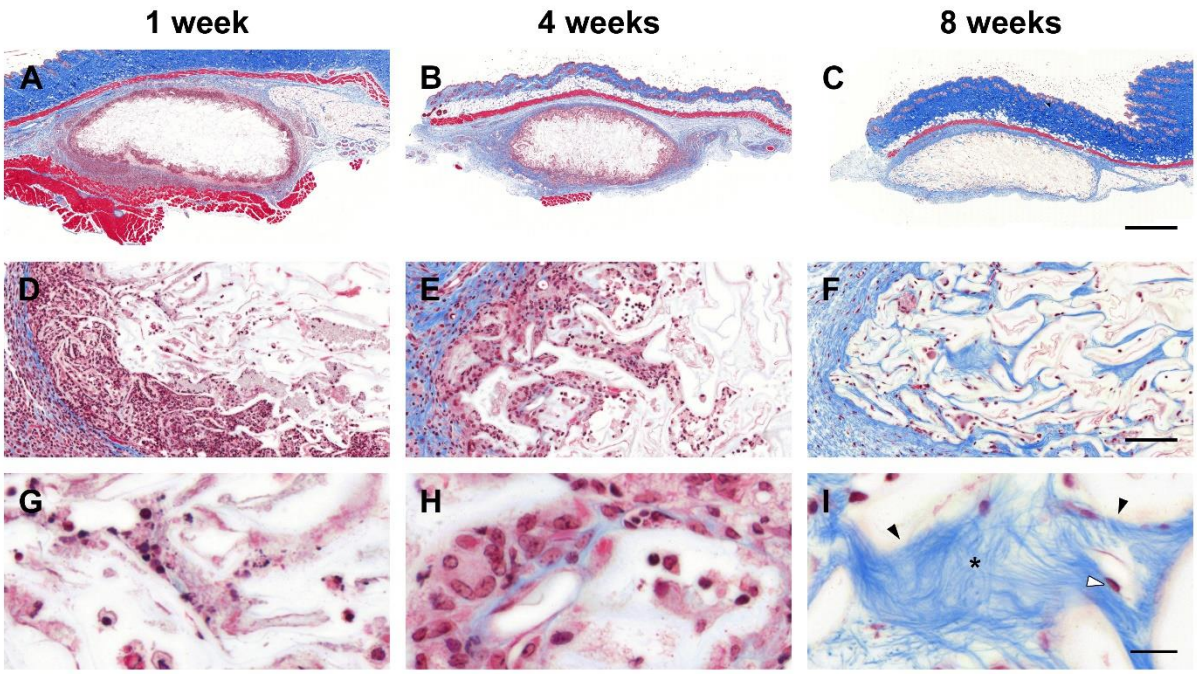

Figure 3.4 Extracellular matrix deposition. Cross sections of representative cellulose scaffolds stained with Masson's Trichrome (**a-c**). After 1 week post-implantation, the magnification of region of interest in (**a**) show the lack of collagen structures inside the collagen scaffold (**d, g**). As fibroblast cells start to invade the scaffold, collagen deposits inside the cellulose scaffold can be sparsely observed after 4 weeks (**e, h**). Concomitant with the observation of activated fibroblast (spindle shaped cells) inside the cellulose scaffold, collagen network is clearly visible inside the cavities after 8 weeks (**f, i**). Scale bars: **a-c** = 1mm, **d-f** = 100µm and **g-i** = 20µm. * = collagen fibers; black arrows = cellulose cell wall; white arrow = fibroblast.

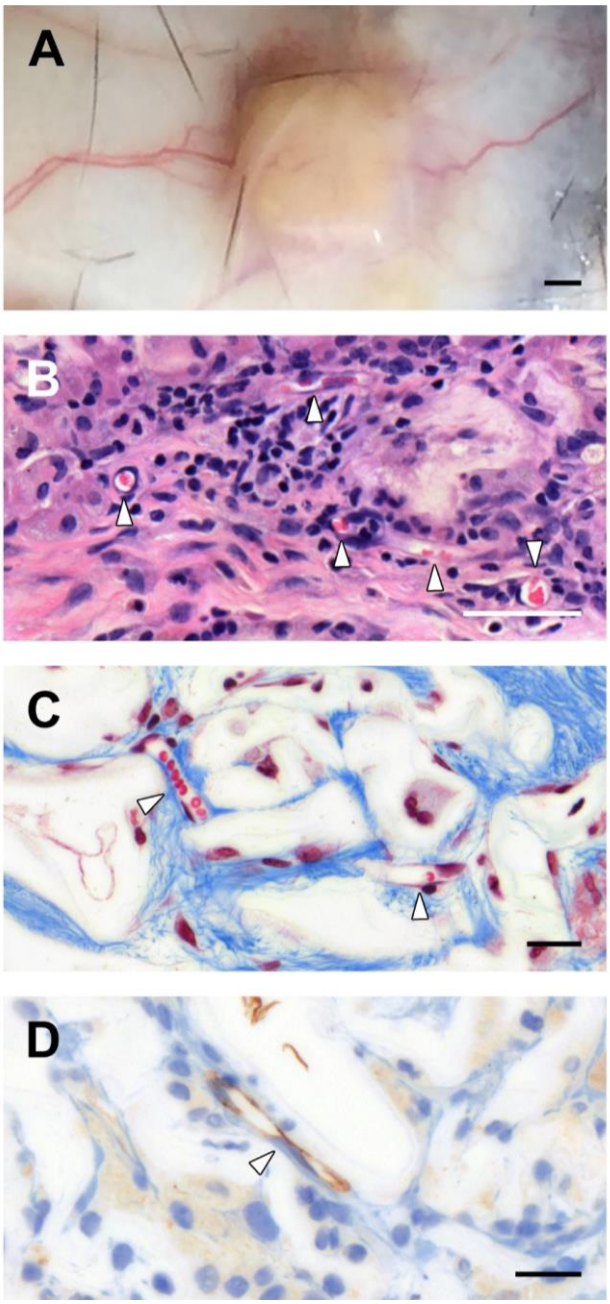

Figure 3.5 Vascularization and Angiogenesis. Macroscopic observations of blood vessels directly in the surrounding tissues around the cellulose scaffold (**a**). Confirmation of angiogenesis within the cellulose scaffold by the observation of multiple blood vessel cross sections in H&E staining (**b**) and Masson's Trichrome staining (**c**) micrographs. The angiogenesis process was also confirmed with anti-CD31 staining to identify endothelial cells within the cellulose scaffold (**d**). Scale bars: **a** = 1mm, **b** = 50μm and **c-d** = 20μm. White arrows = blood vessels.

3.6 Discussion

In this study, our objective was to examine the *in vivo* biocompatibility of acellular cellulose scaffolds derived from apple hypanthium tissue. To this end, acellular cellulose scaffolds were subcutaneously implanted within immunocompetent mice to establish their biocompatibility. Our data reveals that the implanted scaffolds demonstrate a low inflammatory response, promote cell invasion and extracellular matrix deposition, and act as a pro-angiogenic environment. Remarkably, none of the mice in this study died or demonstrated any symptoms of implant rejection such as edema, exudates or discomfort during the course of this research indicative of a successful implantation of the cellulose scaffolds. This implanted scaffolds are composed of a porous network of cavities in which the original host plant cells resided. This architecture efficiently facilitates transfer of nutrients throughout the plant tissue. As we have shown here and in our previous study, the apple tissues are easily decellularized [92]. This simple treatment changes the appearance of the hypanthium tissue so that it becomes transparent, as a result of the removal of cellular materials.

Several important conclusions emerge from the current study. First, after implantation, the scaffolds are rapidly infiltrated with host cells, which begin with inflammatory cells. Consistent with previous findings, the immune response of the host animals followed a well-known timeline [295–299], ultimately demonstrating biocompatibility. As expected, the cell population within the scaffold after 1week post-implantation are mainly granulocytes, specifically; polymorphonuclear (PMN) and eosinophils, constituting a clear inflammatory response. The production of a provisional matrix around the scaffold was also observed resulting in an inflamed appearance in

the tissue surrounding the scaffold [295–299]. This is not unexpected and is the result of the foreign material as well as a response to the surgical procedure [295–299]. Four weeks post implantation, the population of cells within the scaffold have evolved and are now lymphocytes, monocytes, macrophages, foreign body multinucleated cells as well as scattered eosinophils. Typical with chronic inflammation, the cellular debris present in the provisional matrix at 1 week, is now being cleared by the host immune system [295–299]. At 8 weeks, the cellulose scaffold is now void of all provisional matrix and cellular debris and low levels of macrophages and foreign body multinucleated cells are still visible within the scaffold. Consistent with the immune response within the cellulose scaffold, the surrounding tissue is observed to return to its original physiology. In fact, at 8 week implantation the surrounding tissue is nearly similar to control tissue. Although the immune response and inflammation at 8 weeks is low, low levels of macrophages can be observed within the scaffold. Although traditionally associated with inflammation, macrophages have beneficial roles consistent with our findings. Specifically, macrophages are also known to secrete growth and pro-angiogenic factors, ECM proteins and pro-fibrogenic factors that actively regulate the fibro-proliferation and angiogenesis in tissue repair and regeneration [297]. Regardless, the vast population of cells within the scaffold after 8 weeks are now reactive fibroblasts. These cells are altering the microenvironment of the scaffold through the secretion of a new collagen extracellular matrix. Importantly the new matrix displays a remarkably low density compared, suggestive of regeneration as opposed to the characteristic high density, cable-like organization of collagen found in scar tissues [300].

Our data also demonstrates that the scaffolds are pro-angiogenic, which is critical to ensuring blood transport from the surrounding tissue [301]. As with native tissue, limited blood supply to the

scaffold will result in ischemia and potentially necrosis. Interestingly, it was demonstrated that bioceramics with pore diameters lower than 400μm resulted in a decrease in the growth of blood vessels and limits the size of blood vessel diameter in *in vivo* implantations. The porous structure of the cell wall architecture is composed of overlapping cell wall cavities with diameters ranging from 100-300μm with manual interconnection distance of 4.04±1.4μm. As such, the high porosity size and low volume-fraction of the cellulose scaffolds are consistent with the promotion of blood vessel formation. Taken together, the cellulose scaffold now appears to completely void of the provisional matrix and fully accepted as a subcutaneous implant.

We also observed a decrease in the scaffold area over time, but it does not appear that the cellulose scaffold is in the processes of degradation. Rather, the change in area is due to the collapse of the cell wall cavities on the perimeter of the scaffold resulting from the active movement of the mouse. Active biological degradation is not expected to be possible as mammals lack the appropriate enzymes to digest plant-synthesized cellulose [302,303]. Moreover, the highly crystalline form of cellulose that is found in plant tissues is also known to resistant to degradation in mammals [303]. Alternatively, it has been demonstrated that *in vivo* cellulose implants can be chemically activated in order to be more easily degraded [304]. Most importantly however, highly crystalline forms of cellulose have some of the lowest reported immunological responses [303].

A large variety of clinically approved biomaterials are used to treat specific conditions within patients[24]. Such biomaterials can be derived from human and animal tissues, synthetic polymers, as well as materials such as titanium and ceramics [14,24,74,161,171,204,224,230,251,270,273–275,288,305–313].

However, these approaches are not without disadvantages that arise from concerns about the source, production costs and/or widespread availability [269]. There is currently an intense interest in developing resorbable biomaterials that will degrade *in vivo* and only act as a temporary scaffold that will promote and support the repair or regeneration of damaged/diseased tissue [270]. Although this is an ideal scenario, newly formed structures are also found to collapse as the scaffold degrade [48,183,190,273,283]. Moreover, the products of degradation can also be found to have toxic or undesirable side-effects [273,314,315]. For example, the reconstruction of the ear has become a well-known challenge in tissue engineering. Early studies have employed scaffolds in the shape of an ear that are produced from animal or human derived cartilage [273,277,278,280,282,283]. However, after implantation and eventual scaffold degradation, the ear is often found to collapse or deform [279–281]. Recent strategies have now opted to create biological composite materials composed of both a titanium frame embedded in a biological matrix [273]. Therefore, there is still a clear need for non-resorbable, yet inert and biocompatible, scaffolds persist in the field of tissue and organ engineering.

We suggest that plant-derived cellulose biomaterials offer one potential approach for the production of implantable scaffolds. This approach is complementary to bacterial cellulose strategies which have demonstrated clear utility as well [67,72,294,310,316,169–171,173,176,177,285,291]. However, plant derived materials are cost effective to produce and are extremely straightforward to prepare for implantation, exhibit clear biocompatibility, an ability to retain their shape while supporting the production of natural extracellular matrix and most importantly, the promotion of vascularization. In our previous work we have shown that the scaffolds can also be functionalized with proteins prior to culture *in vitro*. Such work will also be conducted in the future in order to

explore the use of scaffold surface functionalization with growth factors and matrix proteins to promote the invasion of specific cell types, further minimize the early immune response and promote maximal vascularization. Moreover, the cellulose scaffolds can easily be formed into specific shapes and sizes, offering an opportunity to create new tissues with specific geometrical properties. Although there are numerous new avenues of research to follow, we have been able to demonstrate that acellular cellulose scaffolds are biocompatible *in vivo* in immunocompetent mice and might be considered as a new strategy for tissue regeneration.

3.7 Acknowledgments

We thank Joshua Lavigne, VT, RLAT for technical assistance with animals, Ana Giassi, PhD for histological processing and Manijeh Daneshmand, MD for her histopathological analysis. We thank Virgile Koffi and Nathan Adolphe for pictures in Figure 1A and B.

Chapter 4| *Manuscript*

PLANT SCAFFOLDS SUPPORT MOTOR RECOVERY AND REGENERATION IN RATS AFTER TRAUMATIC SPINAL CORD INJURY

Daniel J. Modulevsky[1,2], Charles M. Cuerrier[1,2,3], Maxime Leblanc-Latour[1,3], Ryan J. Hickey[1], Ras-Jeevan K. Obhi[1], Isabel Shore[1,3], Ahmad Galuta[4], Krystal L. A. Walker[4], Eve C. Tsai[4,5,6] and Andrew E. Pelling[1,2,3,7,8*]

1Department of Physics, STEM Complex, 150 Louis Pasteur Pvt., University of Ottawa, Ottawa, ON, K1N5N5 Canada

2Department of Biology, Gendron Hall, 30 Marie Curie, University of Ottawa, Ottawa, ON, K1N5N5 Canada

3Spiderwort Inc., 7, Bayview Station Road, Ottawa, ON, K1K4R3 Canada

4Program in Neuroscience, Ottawa Hospital Research Institute, Ottawa, ON, K1Y 4E9 Canada

5Division of Neurosurgery, Department of Surgery, The Ottawa Hospital, Ottawa, ON, K1Y 4E9 Canada

6Department of Cellular and Molecular Medicine, Faculty of Medicine, University of Ottawa, Ottawa, ON, K1H 8M5 Canada

7Institute for Science Society and Policy, Simard Hall, 60 University, University of Ottawa, Ottawa, ON, K1N5N5 Canada

8SymbioticA, School of Human Sciences, University of Western Australia, Perth, WA, 6009 Australia

Submitted October 24, 2020 to Nature

- I, Daniel Modulevsky, contributed to the majority of the research work, including the production of biomaterials, surgeries, animal care, scanning electron microscopy and image acquisition. Andrew E. Pelling was instrumental in the preparation of the first draft and subsequent revisions
- The arrangement of the manuscript has been modified for thesis formatting purposes.

Motivation |

- In the last part of the thesis, we demonstrated that plant-derived biomaterial that already had success and safety *in vivo* applicability could be used to treat a significant pathology in an animal model.

4.1 Hypothesis and Objectives |

- I hypothesize that the vascular bundles that mimic the tube-like design of many current spinal cord biomaterials can be used to re-connect the severed ends of the spinal cord by providing additional structural and mechanical support as well as providing nano- and micro-topographical cues
- Complete transection of the spinal cord will be an appropriate model as any improvement in the biomaterial can be attributed to the biomaterial rather than the model's neuroplasticity.

- Creating SCI implantable grafts, matching the diameter and individual length for each animal within the study

- Several studies demonstrate the effect of nano- and micro-topographical cues that effectively drive neuronal and axonal guidance.[317–319] We speculate that vascularized plant tissue architecture will act as a natural axonal guide reconnecting the severed ends of the spinal cord and providing a bridge via the scar tissue formation allowing for motor and sensory axons to reconnect.

- The mammalian spinal cord produces endogenous stem cells found within the ependymal region. If the plant-derived biomaterial can provide the underlying support structure, the injured spinal cord can potentially repair the recover the function of the lower limbs.

- The current approach to spinal cord therapy is a biodegradable compound that will degrade throughout implantation. We hypothesize that a non degradable stable scaffolds will provide a stable platform for neuronal reconnection.

- **Chapter 4| PLANT SCAFFOLDS SUPPORT MOTOR RECOVERY AND REGENERATION IN RATS AFTER TRAUMATIC SPINAL CORD INJURY**

4.2 Abstract

As of yet, no standard of care incorporates the use of a biomaterial to treat traumatic spinal cord injury (SCI)[126,320–323]. However, intense development of biomaterials for treating SCI have focused on the fabrication of microscale channels to support the regrowth of axons while minimizing scar tissue formation[26,97,324–326]. We previously demonstrated that plant tissues can be decellularized and processed to form sterile, biocompatible and implantable biomaterials that support cell infiltration and vascularization *in vivo*[73,92,96]. Notably, the vascular bundles of plant tissues are also composed of microscale channels with geometries thought to be relevant for supporting neural tissue regeneration[26,327]. We hypothesized that decellularized vascular bundles would support neural regeneration and the recovery of motor function. Therefore, rats that received a complete T8-T9 spinal cord transection were implanted with plant-derived channelled scaffolds. Animals that received the scaffolds alone, with no therapeutic stem cells or other interventions, demonstrated a significant and stable improvement in motor function over six months compared to controls. Histological analysis reveals minimal scarring and axonal regrowth through the scaffolds, further confirmed with tracer studies. Taken together, our work defines a novel route for exploiting naturally occurring plant microarchitectures to support the repair of functional spinal cord tissue

4.3 Introduction

The annual incidence of traumatic spinal cord injury (SCI) is as much as 51 per million people in developed countries, with mortality rates of 48-79%[328]. Although treating the devastating loss of motor function is the ultimate clinical goal, recovery of bowel, bladder, sexual and tactile function can all contribute to a significant improvement in patient quality of life[329]. While there are no accepted therapies to treat the underlying issue of scar and cyst formation at the epicentre of the injury[126,320–323], one possible approach is the use of a biomaterial that promotes axonal regrowth, sequesters scar tissue and supports blood vessel formation, which can ultimately aid in the recovery of function[330]. There has been an intense effort to create scaffolds with 3D architectures designed to achieve this goal utilizing all manner of microfabrication techniques[26,324–326,331]. As such, the performance of many varieties of natural and synthetic polymers have been investigated in a number of SCI animal models[26,36,39,41,53,97,109,116,126,324–326,332–335]. In many studies, scaffolds demand supplementation with neural progenitor cells (NPCs), pharmaceuticals, or growth factors (alone or in combination) to achieve the desired effect[26,326]. Often, tissue regeneration and improvement in motor recovery is only possible with combined strategies[26,43,114,336–338].

Here, we investigated the stalks of *Asparagus officinalis* as a potential biomaterial as they contain linearly arranged, parallel microchannels which form vascular bundles (VBs) (Figure. 4 a, b). The VBs are circularly arranged and separated from one another by parenchyma tissue with an average spacing of 612±70μm. The VBs are composed of tissues that aid in the efficient transport of water, nutrients and biomolecules throughout the plant and their structures are preserved after decellularization (Figure 4.1 a, b). Scanning electron microscopy (SEM) of the VBs reveals a variety of tissue structures with characteristic diameters, such as xylem channels (51±15 μm), sieve tubes (40±16μm), parenchyma (35±8μm) and the phloem (9±2μm) (Figure. 4.1 c-e,

Supplementary Figure. 4.1). Due to the distribution of microchannels in their architecture, we hypothesized that decellularized vascular plant tissues could be exploited as lignocellulosic scaffolds for the repair of completely transected spinal cord in a rat model.

4.4 Material and Methods

4.4.1 Biomaterial Production

This protocol is based on our previously published works[9–11]. Asparagus (*Asparagus officinalis)* was purchased from local supermarkets. The asparagus was stored at 4°C in the dark for a maximum of one week and kept hydrated. In order to prepare the scaffolds, the asparagus stalks (with a diameter of 14–17 mm) were washed, and the end of the stalks were cut to remove any dried tissue. The scaffolds were cut at different lengths using a #820 microtome (American Optical Company). The thickness of the asparagus scaffold was adjusted with the z-position block. The desired length of asparagus was cut with microtome blades (Westin Instruments Boston) in a quick motion to create two perpendicular surfaces with a precise length ranging from 0.2 mm – 1.6 cm. The resulting sections were then measured with a Vernier calliper. A 4 mm biopsy punch was used to cut out cylindrical sections close to the edges of the tissue to maximize the number of VBs. An effort was made to avoid the central fibrous tissues common in all angiosperm plants. Asparagus samples were placed in sterilized 2.5ml microcentrifuge tubes, and 2ml of 0.1% sodium dodecyl sulphate (SDS) (Sigma-Aldrich) solution was added to each tube. Samples were shaken for 48 hours at 180 RPM at room temperature. The resulting cellulose scaffolds were then transferred into new sterile microcentrifuge tubes, washed and incubated for 12 hours in phosphate-buffered saline (PBS) (Sigma-Aldrich). Following the PBS washing steps, the asparagus were then incubated in 100 mM $CaCl_2$ for 24 hours at room temperature to facilitate the removal of any of the remaining SDS. The samples were washed 3 times with dH_2O and then sterilized in 70%

ethanol overnight. Finally, they were then washed 12 times with sterile saline solution and stored in saline. At this point, the samples were immediately used or stored at 4°C for no more than 24 hours.

4.4.2 Young's Modulus Testing

Scaffolds were loaded onto a CellScale UniVert (CellScale) compression platform. The Young's modulus was measured by compressing the material to a maximum 10% strain, at a compression speed of 50 µm/s. The force-indentation curves were converted to stress-strain curves and fitted in Origin 8.5. The Young's modulus was extracted from the elastic region of the curves.

4.4.3 Animal Care and Surgical Procedures

All procedures described in this study were approved by the University of Ottawa Animal Care and Veterinary Services ethical review committee. Female Sprague Dawley rats ranging in weight from 250-300 grams were purchased from Charles River. The rats were anesthetized with isoflurane USP-PPC (Pharmaceutical partners of Canada) and injected subcutaneously with normal saline (Baxter) and enrofloxacin (Baytril). Laminectomies were performed at the T8-T9 level to expose the spinal cord. The dura was incised with micro scissors to expose the spinal cord. A hook was passed ventrally to ensure the entire cord was within the bend of the hook. The spinal cord was carefully lifted with the hook and the entire cord was then cut with micro scissors. Both stumps of the spinal cord were carefully examined to confirm complete transection of spinal cord and spinal roots at that level. Surgifoam 1972 (Ethicon) was inserted into the gap between the two spinal cord stumps. After several minutes, when hemostatic control was established, the surgifoam was removed and the resulting gap size was measured. Prior to the surgery, animals were randomly assigned as biomaterial or control. For animals assigned to the biomaterial group, a biomaterial

scaffold was selected that best matched the gap distance of the stumps (range was typically 1to 3.5 mm). A volume of 0.2 mL Fibrin glue (Tisseel) was then applied to the dorsal surface to stabilize the biomaterial. Negative control animals had 0.2 mL fibrin glue placed between the two stumps. The muscle layers were then reapproximated with 3-0 Vicryl sutures (Johnson & Johnson) while the skin was closed with Michel clips (Fine Science Tools). Following the surgery, rats had their bladders expressed manually three times a day and were monitored for any symptoms of weight loss, dehydration, pain and urinary infections.

4.4.4 Functional Studies

The locomotor function of the rats was assessed weekly based on the Basso Beattie Bresnahan (BBB) open-field assessment[339]. The rats were placed at the same time point in a 1-meter diameter arena once a week and was assessed by an independent blind observer while also being recorded from at least one view point for the entire duration of the cohort. Each of the five minutes videos of the rats was then scored by three blind observers and was averaged to get a weekly score. Any substantial spasticity and reflexes/twitches in any of the four joints were ignored and confirmed with repeated views of the videos.

4.4.5 Retrograde Tracer Study

Rats with biomaterial and controls were randomly selected at 14 weeks post-injury to undergo retrograde tracer studies. Animals were anesthetized and maintained with isoflurane USP-PPC (Pharmaceutical partners of Canada). A laminectomy was then performed at the T13 level with a complete spinal cord transection performed as described in the previous spinal cord transections. In the spinal cord transection gap, a surgifoam (Ethicon,) soaked in 10 uL of 4% FluoroGold (Fluorochrome) in saline was placed onto the rostral end of the spinal cord stumps. Petroleum jelly (Sherwood Medical) was then added to stabilize the surgifoam into place and prevent nonspecific

labelling before the muscles were then closed with 3-0 Vicryl. The skin was then closed with Michel suture clips (Fine Science Tools). The rats were allowed to recover and were monitored for 7 days to allow the FG to travel.

4.4.6 Spinal Cord and Biomaterial Resection

For harvesting of the tissue, animals were sacrificed by intraperitoneal injection of 0.7–1.0 ml of sodium pentobarbital (65 mg/ml) and underwent intracardiac perfusion with 500 mL of normal saline and 0.5 U/mL heparin solution. The rats then perfused with 500 mL of 4% paraformaldehyde (Sigma-Aldrich,) in 0.1mM PBS(Sigma-Aldrich). The entire spinal cord and brain was then dissected out and further fixed overnight in 4% paraformaldehyde and 0.1mM phosphate buffer solution at 4°C. The tissue was then removed from the fixation solution and incubated in 30% sucrose (Sigma-Aldrich) 1% sodium azide (Sigma-Aldrich) in PBS for 24 hours at 4°C. The biomaterial and the surrounding tissue were then frozen and mounted in Optimum Cutting Temperature compound (Stephens Scientific) with the remaining tissue fixed into paraffin. For tracer animals, the entire spinal cord and brain were frozen in individual blocks. Axial and sagittal sections of the tissue at 7–10 μm thick were then processed and mounted onto cold Superfrost Plus slides (Fisher Scientific) by the PALM Histology Core Facility at the University of Ottawa. Slides were stored in -80°C freezer until stained and mounted.

4.4.7 Histology and Immunochemistry

Frozen sections were stained with hematoxylin-eosin (H&E). Frozen sections were completely dried, rehydrated in 1X TBST buffer and blocked for 30 minutes with Rodent Block R (Biocare). Sections were then incubated overnight at 4°C with the following primary antibodies rabbit AB5804 GFAP (1:2000, Millipore) and mouse N0142 NF200 (1:3000, Sigma). The following day, the sections were washed with 1X TBST and then incubated with secondary antibodies: AB150077

Goat anti-rabbit 568 (Abcam) or AB175473 Goat anti-mouse 568 (Abcam) at 1:500 dilution for 2 hours in the dark at room temperature. Sections were washed with 1X TBST, incubated with 1ug/mL of DAPI (Thermo Scientific), washed, and then mounted in VectaShield Vibrance (Vector Laboratories) before adding a cover slip. The slides were kept in the dark at -20°C for a maximum of a week prior to imaging.

4.4.8 Microscopy

Micrographs of colorimetric stains were captured using Zeiss AxioScan Z1 slide Scanner (Zeiss) equipped with 10x objective and analyzed using ZenBlue (Zeiss, Canada) and ImageJ software. Phase microscopy was carried out on an A1R TiE inverted optical microscope (Nikon). Fluorescence imaging of tissue sections stained with NF200 and GFAP antibodies was carried out on a Nikon A1RsiMP Confocal Workstation with a 32-detector array for spectral imaging with 6 nm resolution detectors (Nikon). As lignocellulose can be auto fluorescent, spectral linear unmixing was achieved by imaging negative control scaffolds to obtain autofluorescence spectra. The spectral profile of the 568 antibody was then unmixed from any scaffold autofluorescence and the resulting unmixed z-stack was 3D deconvolved to create a projection. Although both antibodies have the same 568nm wavelength fluorophore, for clarity NF200 data is presented as false-color green images to distinguish from false-color red GFAP data. FG slides samples were imaged with a Nikon Ni-U Ratiometric Fluorescence Microscope with a 340/380 filter set. All image processing was carried out with Nikon Elements software (Nikon).

4.4.9 Scanning Electron Microscopy

The structure of cellulose was studied using a SEM. Globally, scaffolds were fixed in an electron microscopy grade 4% PFA (Fisher Scientific) and dehydrated through successive gradients of ethanol (50%, 70%, 95% and 100%). The biomaterial was then dried with a critical point dryer (CPD) (SAMDRI-PVT-3D). Samples were then gold-coated at a current of 15mA for 3 minutes with a Hitachi E-1010 ion sputter device. SEM imaging was conducted at voltages ranging from 2.00–10.0 kV on a JSM-7500F Field Emission SEM (JEOL).

4.4.10 Statistics

All values reported here are the average ± standard error of the mean. Statistical analyses of the BBB scoring and scaffold volume were performed with one-way ANOVA by using SigmaStat 3.5 software (Dundas Software Ltd). A value of $p<0.05$ was considered statistically significant.

4.5 Results and Discussion

On average, each scaffold contained 11±2 VBs, each containing 35±5 microchannels. These channels were observed to be consistent in diameter and orientation throughout the entire scaffold and emerge in the same position on either end (Supplementary Figure. 4.2). Scaffolds were selected that contained the maximum number of VBs to promote invasion of regenerating axon projections in a completely transected spinal cord. The scaffolds are mechanically anisotropic due to the linear orientation of the VBs along the plant stem. This results in an elastic modulus of 148±53kPa (n=10) or 12±4 kPa (n=10) when measured parallel or perpendicular to the long axis, which is within the range of healthy rat spinal cords[340] (Supplementary Figure 4.3).

In animals with a complete T8-T9 spinal cord transection, the scaffold group (n=18 animals) had grafts inserted with lengths to match the stumps' intra gap distance. Fibrin was applied across the dorsal surface of the scaffold to fix it between the stumps (Figure 4.1 f). The control group (n=13

animals) did not receive the scaffold and the fibrin was applied to the gap formed between the stumps. After 4 weeks, animals were imaged with magnetic resonance imaging (MRI) to confirm that the scaffold remained in place (Fig. 4.1 g, h). The rostral and caudal stumps of the transected spinal cord remain aligned with the scaffold, while in the control animals, typical symptoms of intermediate and chronic secondary spinal cord injuries were apparent[26,41,110,329,335,341,342].

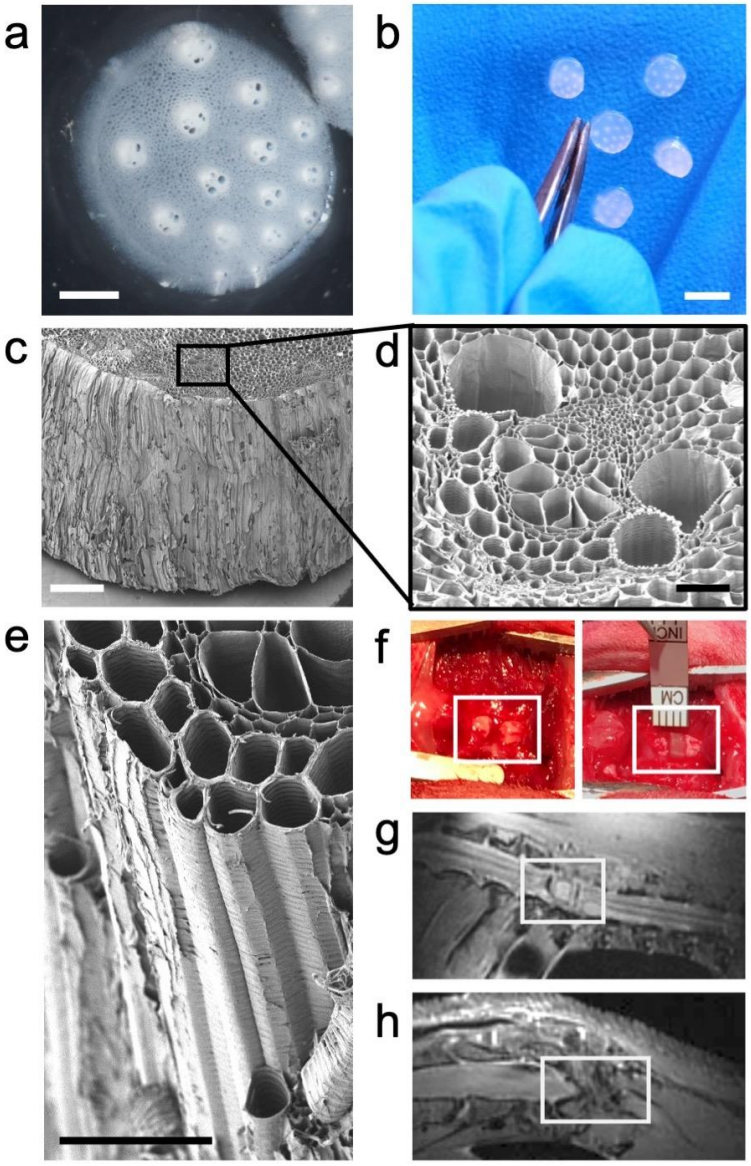

Figure 4.1 | Plant-derived scaffolds for spinal cord injury. a) Decellularized plant-derived scaffold with visible vascular bundles (VBs) surrounded by parenchyma (bar=1mm). **b)** VBs are even visible to the naked eye (bar=4mm). **c)** SEM reveals scaffolds also have a grooved outer topography (bar=300µm). **d)** Imaging the scaffold cross-section at higher magnification reveals a VB (bar=100µm). **e)** VB channel architecture runs the entire length of the scaffold (bar=100µm). **f)** An exposed fully transected spinal cord (left, box) and a scaffold after implantation (right, box). **g**) Sagittal MRI of T8-T9 injury (box) containing a scaffold after 4 weeks, and **h)** the resulting scar a control animal.

The motor recovery of the rats was blindly assessed using the established Basso, Beattie and Bresnahan (BBB) locomotor scale[339]. Rats that received the scaffold had a statistically significant ($p=0.030655$) functional recovery starting at week 4 (Figure 4.2a). Though both groups were observed to display some motor recovery, the degree of recovery was significantly higher in animals that received the scaffold. By week 4, control scores plateaued at 2.3±0.5 (extensive movement of one joint). Conversely, the scaffold group displayed continued improvement until week 7, after which the BBB score plateaued at 5.5±0.1 (extensive movement at all three hindlimb joints, $p= 2.4x10^{-7}$). This improvement in motor function was consistent with limb recovery and coordination, leading to weight-supported plantar stepping (Supplementary Figure 4.4). The motor skills did not deteriorate significantly over the remainder of the 6 months (Figure 4.2a). To rule out reflex adaptation, random animals were selected for an end point re-transection surgery at the T13 vertebra[43]. Animals were allowed to recover for one week before motor skill re-assessment. In the scaffold and control groups, motor recovery was lost and BBB scores of 0.3±0.2 and 0.1±0.1, respectively ($p=0.251289794$). The rats were euthanized and harvested at their respective endpoints of 14 and 28 weeks. Tissue was sectioned in either an axial or sagittal orientation (Figure 4.2 b-f) and stained with hematoxylin and eosin (H&E). It was observed during the dissection that the scaffold was well integrated well enough between the two stumps of the spinal cord that the entire structure could be moved as one unit. The control groups were difficult to remove as the stumps loosely adhered via scar and connective tissues. These observations are consistent with MRI, which revealed that the scaffold formed a physical bridge between the spinal cord stumps (Figure 4.1 g)

At 14 weeks, H&E staining revealed that the scaffold retained its pre-implant size. Although macrophages were present, there was no observable degradation of the scaffold (Figure 4.2 b).

The VBs within the scaffold were infiltrated with cells throughout its length between the spinal cord stumps (Fig. 2c, d). Almost no foreign multinucleated cells, basophils cells or lymphocytes associated with chronic foreign body response (FBR), were observed (Figure 4.2 e). Importantly, at 28 weeks H&E imaging revealed results highly consistent with the 14 week time point (Supplementary Figure 4.5). Moreover, the control animal injury site was void of cell infiltration, with cysts forming at the site of transection, as is typical with untreated SCI transection injuries[3] (Figure 4.2 f). Capillaries and blood vessels were found in 86% of all VBs, which demonstrated that the channels of the scaffold support vascularization throughout the injury site (Figure 4.2e), consistent with our previous in vivo studies[73,96]. The vascularized VBs are then likely able to supply infiltrating cells in the nearby scaffold tissues with nutrients/oxygen. This is consistent with the observation of host fibroblast cells migrate within the interstitial spaces formed by the overlapping plant cell walls in the parenchyma tissue (Figure 4.2d, e). The largest channels of VBs were observed to incorporate the majority of granulation scar tissue or mature blood vessels characterized by a thick endothelial lining (Figure 4.2e). Thus, the mammalian scar tissue response appeared to be largely sequestered to the VB elements (Supplementary Figure 4.6).

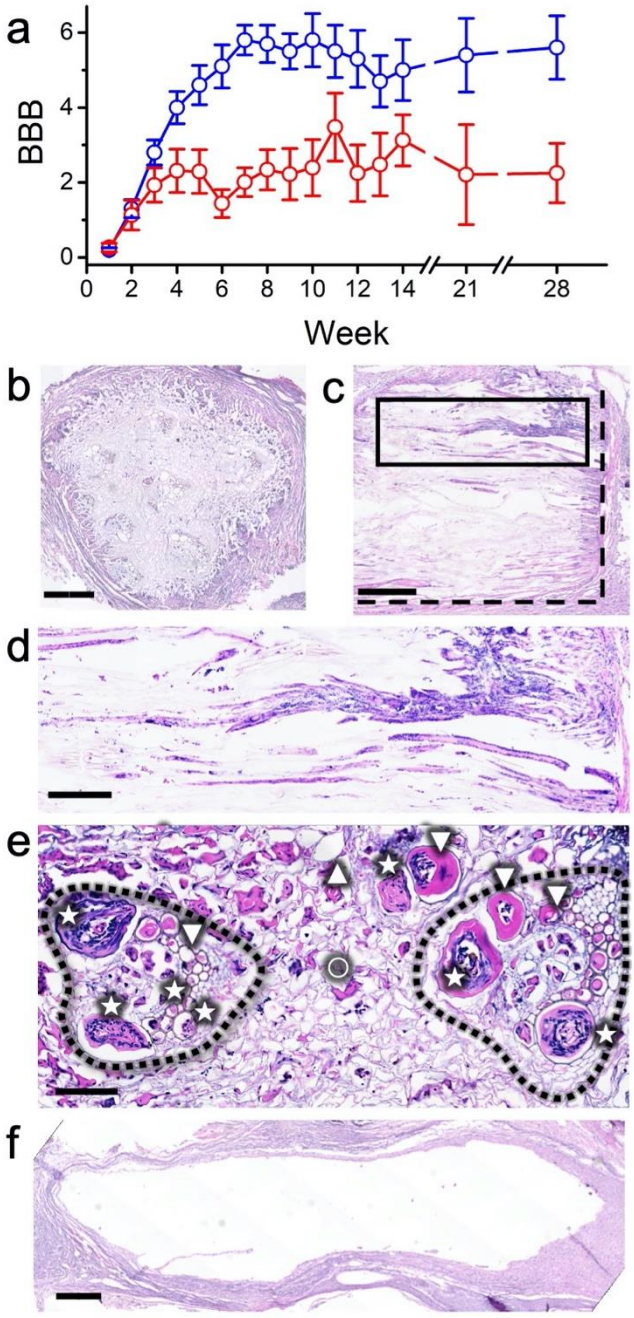

Figure 4.2. Motor recovery and histology after 14 weeks post injury. a) BBB motor scores after complete transection in animals with (blue) and without (red) a scaffold are significantly different from week 4 (p=0.030655) and onwards. **b)** Axial H&E of scaffold. VBs are infiltrated with host cells (bar=400μm). **c)** Sagittal H&E of the scaffold (bar =500μm) and **d)** higher magnification of the boxed (bar=250μm). VBs are infiltrated from the stumps and cells are observed throughout the scaffold (scaffold-tissue interface (dotted line)). **e)** H&E of two VBs (dotted lines) after 14 weeks. Blood vessels (▽), granulation tissue (★) are observed in the VBs. The parenchyma (o) between the VBs contains fibroblasts (△) (bar=100 μm) **f)** Sagittal H&E of a control animal spinal cord for comparison (bar=500μm).

The formation of astrocyte scarring was assessed by glial fibrillary acidic protein (GFAP) labelling. The rostral and caudal ends of the scaffold-spinal cord interface both displayed low GFAP scarring when compared to the control animal stump (Figure 4.3a-c). The thickness of the GFAP labelled astrocyte scarring when present around the biomaterial was measured at 54±3.5 µm, significantly less than the control animals at 159±8µm ($p=1.23631x10^{-17}$) (Fig. 3d). These results were consistent with the inhibition of astrocyte scarring in previously reported synthetic cellulose-based scaffolds[6]. When GFAP-positive astrocytes were observed in the scaffold and surrounding tissue they were generally located within the largest diameter VBs. Though the precise role of glial scar tissue is still not known, scarring was observed to be segregated within the large diameter channels[343–345]. This left the parenchymal tissue and smaller VBs available for projecting axons.

Host axons, labelled with neurofilament protein NF200 were observed regenerating readily throughout the entire scaffold in a linear orientation along the median axis of the spinal cord (Figure 4.3 e-g). Axon density in the scaffolds (545±37 axons/mm^2) was significantly higher ($p=0.01859$) than in the tissue of the control scar tissue (368±62 axons/mm^2) (Figure 4.3 h). Cells and axons surrounding the scaffold were also observed to be aligned to external linear topography (Figure 4.1 e , Figure 4.3 i) of the biomaterial, consistent with contact guidance[346]. Minimal scar tissue was also observed in these regions (Figure 4.3 j). These results suggest that the scaffold provides a microenvironment that promotes the growth of native axons while inhibiting uncontrolled astrogliosis.

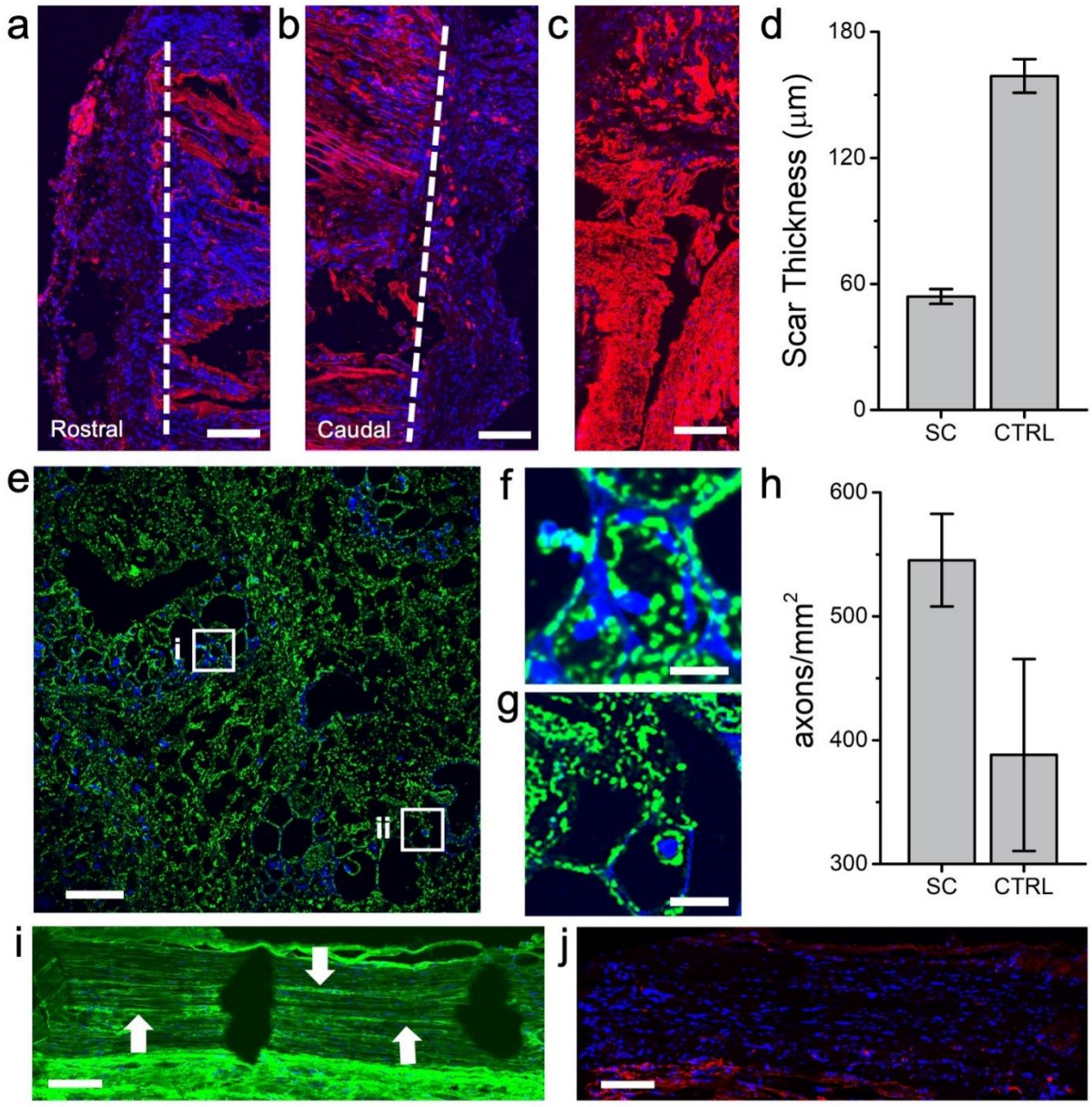

Figure 4.3. NF200 and GFAP staining 14 weeks post injury. a) Rostral end, sagittal view of the scaffold interface (dotted line) with spinal cord stained for GFAP (red) and DAPI (blue) (bar=500μm, for a to c). **b)** Caudal end, Sagittal view of the same implant. **c)** Axial section of GFAP and DAPI stained control animals. **d)** The thickness of the GFAP astrocyte scar tissue in scaffolds (SC) vs control (CTRL) ($p=1.23631x10^{-17}$). **e)** Axial section within the scaffold of NF200 (green) and DAPI (blue) after 14 weeks (bar=100μm). Magnification of the boxed areas **i** and **ii** are shown in **f)** and **g)**, respectively (bar=25μm). **h)** The density NF200 labelled axons within the scaffold and control tissue ($p=0.01859$). **i)** Sagittal view of longitudinal sections of the tissues on the dorsal surface of the scaffold. Axons appear in a linear orientation (arrows) (bar=125μm). **j)** Another sagittal view reveals limited scarring in tissues on the dorsal surface of the scaffold (bar=125μm).

To determine the functionality of axons projecting into the scaffold from the rostral and caudal ends, we utilized retrograde axonal tracing with Fluorogold (FG)[347]. At 14-weeks post injury, animals with scaffolds, and controls (n=3 for both), underwent a second complete transection at T13 (Figure 4.4a), and had FG applied to the rostral aspect of the cut cord to label the cell bodies of neurons in a retrograde fashion. FG labelled axons were observed inside the scaffold at the rostral and caudal ends (Figure 4.4b, c). An axial section of the scaffold also revealed the presence of point-like structures consistent with axon morphology (Figure 4.4d) and NF200 staining (Figure 4.3e-g). Importantly, FG positive cell bodies and axons were observed in the rostral spinal cord tissue across the scaffold (Figure 4.4e). In control experiments, we observed low FG signal, and a lack of non-specific FG wicking through the scaffold in negative controls (Supplementary Figure 4.7). These results confirmed that FG-positive cells were a result of retrograde axonal transport. FG intensity and FG positive cell counts were quantified in the spinal cord rostral and caudal to the scaffold (Figure 4.4f). The number of FG-positive cells on the rostral side of the injury was significantly decreased compared to the caudal end in control animals ($p=0.01102$), which was not the case in animals that received a scaffold ($p=0.77785$). Likewise, FG intensity nearly disappeared across the transection in the control animals ($p=0.00278$). Conversely, in animals that received a scaffold, FG intensity remained constant ($p=0.59004$). The results demonstrate the presence of axonal connections between neurons on the caudal side of the scaffold to axons and cell bodies on the rostral side (Supplementary Figure 4.8).

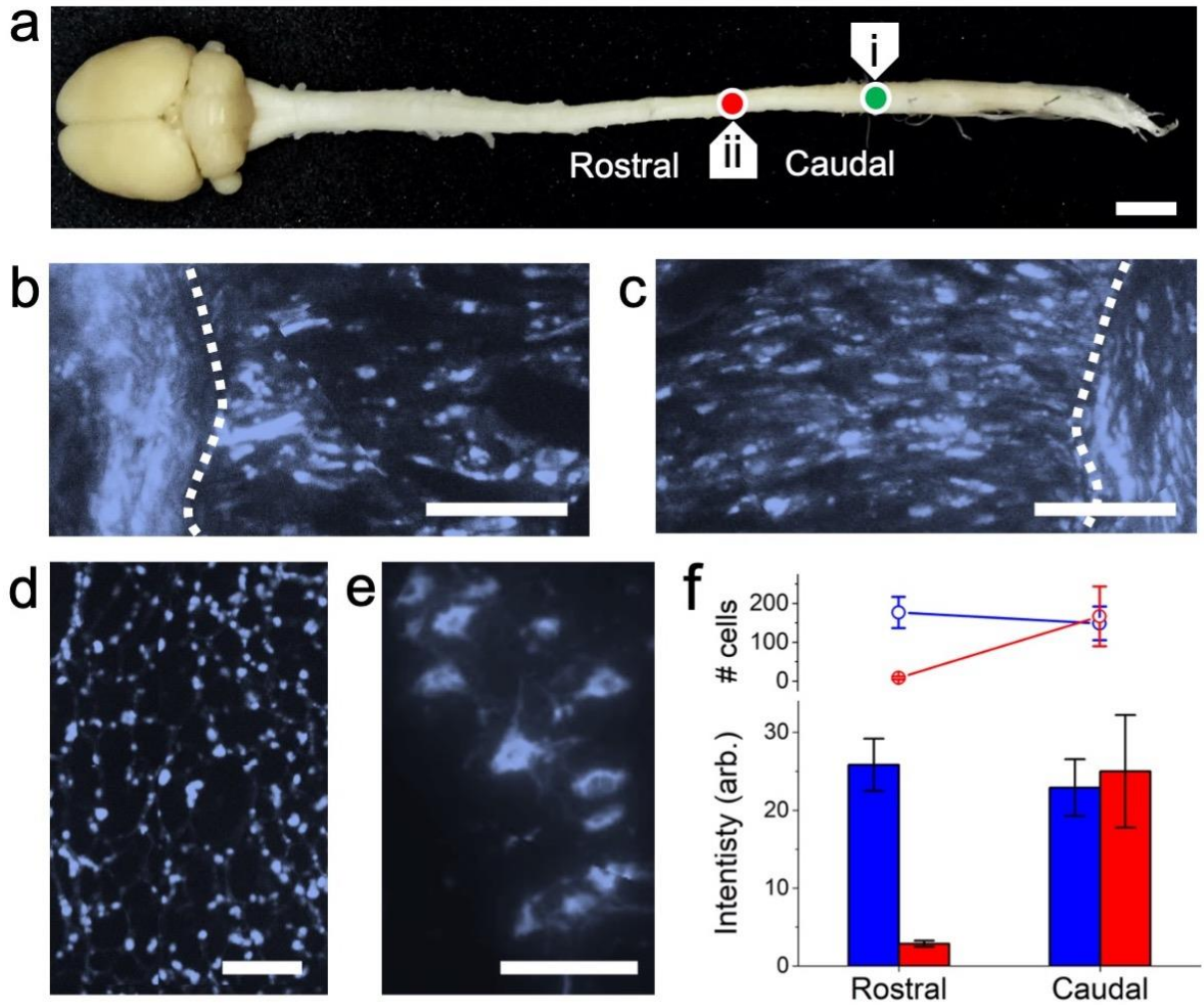

Figure 4.4. Retrograde axonal tracing 14 weeks post injury. a) Animals received a secondary transection (i) at T13 caudal to the original injury (ii) and FG was loaded into the new site (healthy CNS shown for illustration). One week later, sagittal sections of the **b)** rostral and **c)** caudal ends of the scaffold reveal projecting axons at the scaffold-tissue interface (dotted line) (bar=100µm). **d)** Axial section of the scaffold with FG positive axons (bar=100µm). **e)** A magnified view of the rostral spinal cord with FG positive cell bodies and axons (bar=100µm). **f)** The number of FG positive cells and corresponding FG intensity significantly decreases after the injury site in controls (red) ($p=0.01102$ and $p=0.00278$, respectively) as opposed to animals with scaffolds (blue) ($p>0.05$).

There has been significant hope in the treatment of SCI with the development of a multitude of natural and synthetic biomaterials[8,41,97,104,332,348–351]. Scaffolds composed of chitosan, collagen, hyaluronic acid, silk, methacrylate-derived poly-(2-hydroxyethyl) methacrylate and polyethylene glycol (PEG) have all demonstrated promising potential for SCI repair. Recently, researchers were able to create complex CNS structures in 3D printed PEG scaffolds[26]. This innovative approach led to the creation of scaffolds with microscale channels that mimicked the underlying architecture of the spinal cord in a rat model[26]. However, only once loaded with NPCs did these scaffolds result in animals achieving a BBB score of 6.6±0.5 after a complete transection injury. Consistent with our study, the channels in our scaffolds aided the sequestration of astrogliosis allowing for axonal projection[7]. Several previous studies have also demonstrated significantly increased BBB scores but only after scaffolds were loaded with NPCs and complementary agents to aid in neuroregeneration[26,43,124,337,351–353]. A common characteristic of these studies is that NPCs and other therapeutic approaches are required to stimulate any significant motor function recovery. In contrast, we observed an improvement in motor function similar to previous studies, without the necessity of loading scaffolds with therapeutic stem cells or other agents. Furthermore, to our knowledge only a small minority of studies have demonstrated that a non-degradable stable scaffold can lead to a consistent improvement in motor function over the course of six months in a rat model[336,354]. In contrast to many scaffold materials, we have shown that naturally derived plant cellulose scaffolds are biocompatible and become highly vascularized after implantation[73,96]. The low FBR and presence of significant vascularization in our scaffold aided both tissue infiltration/regeneration and also functional recovery without the need for therapeutic factors.

Biodegradability is often thought to be a necessary for implantable biomaterials[39]. However, natural biomaterials such as chitosan have shown some success in SCI while being non-

degradable[104]. Plant-derived cellulose scaffolds are non-resorbable; however, they are highly biocompatible after implantation, structurally stable, and support tissue integration[73,96]. The scaffolds maintained their physical dimensions even after 6 months of implantation due to the lack of degradation. The scaffolds utilized here also do not display signs of chronic FBR and 86% of VBs become vascularized. Taken together, these results decrease the likelihood of the scaffolds being detrimental to motor recovery or require surgical removal. Host cells were able to infiltrate and pass through the full length of the VBs. Interestingly, scar tissue appeared to be sequestered in the largest of the VBs and we speculate that this phenomenon may be beneficial for the observed recovery. Finally, the FG results demonstrated that plant-derived scaffolds support axons from the stumps which are then able to form reconnections across the injury site.

The primary objective of this study was to establish that the microarchitectures found in plant-derived scaffolds can be exploited to repair neuronal tissues in SCI and offer a potential platform for future discovery and innovation. These exciting results demonstrate that such scaffolds are effective in supporting the regeneration of functional neural tissues in the most extreme model of traumatic SCI. In future work, we will explore the impact of loading scaffolds with NPCs as we expect a synergistic effect on improving regeneration and motor skill recovery. Acellular lignocellulosic scaffolds can be seeded with a vast array of cell types, as well as functionalized to include extra-cellular matrix proteins or neural growth factors through hydrogel loading and/or surface functionalization[74,122,177,333,355]. The emergence of plant-derived scaffolds for tissue engineering has opened up many new possibilities to regenerate target tissues of interest including soft tissues, muscle, and bone by exploiting plant microarchitectures[6–8,73,92,96,356]. The results presented here demonstrate that such approaches can be exploited to aid in the regeneration of traumatic SCI, an incredibly complex injury model. The results point to exciting potential patient-

treatment strategies in which plant-derived scaffolds might be deployed in combination with other therapeutics.

4.6 Acknowledgments

We would like to thank Dr Holly Orlando, and the veterinary technicians of the Animal Care and Veterinary Service team of the University of Ottawa; Anne-Renée Desjardins, Catherine Thibault, Roxanne Cote, Caroline Côté, Anik Baillot, Amanda Wells, Melissa Washington, Christine Kitchen, Pascale Beaudry, Catherine Lépine Bisson, and Tami Janveau. The authors would also like to thank Dr. Ana Giassi, Dr. Sharlene Faulkes, Dr. Li Dong, Eric Labelle and Dr. Ziba Jaberansari, for their help with histological processing. We would like to thank Dr. Rafay Axhar and Dr. John Woulfe, for their histopathological analysis. We thank Andrew Ochalski, Dr. Wissam Nakhle and Dr. Gregory Cron for their microscopy and image-processing assistance. The authors wish to thank Dr. Yun Liu for assistance with SEM imaging. We also thank Dr. Sebastian Hadjiantoniou, and Dr. Sophie Chagnon-Lessard for surgical assistance. This work was supported in part by grants to AEP from the National Sciences and Engineering Research Council Discovery Grant, a Canada Research Chair, the Canada Foundation for Innovation, the Li Ka Shing Foundation and the University of Ottawa.

4.7 Supplementary Information

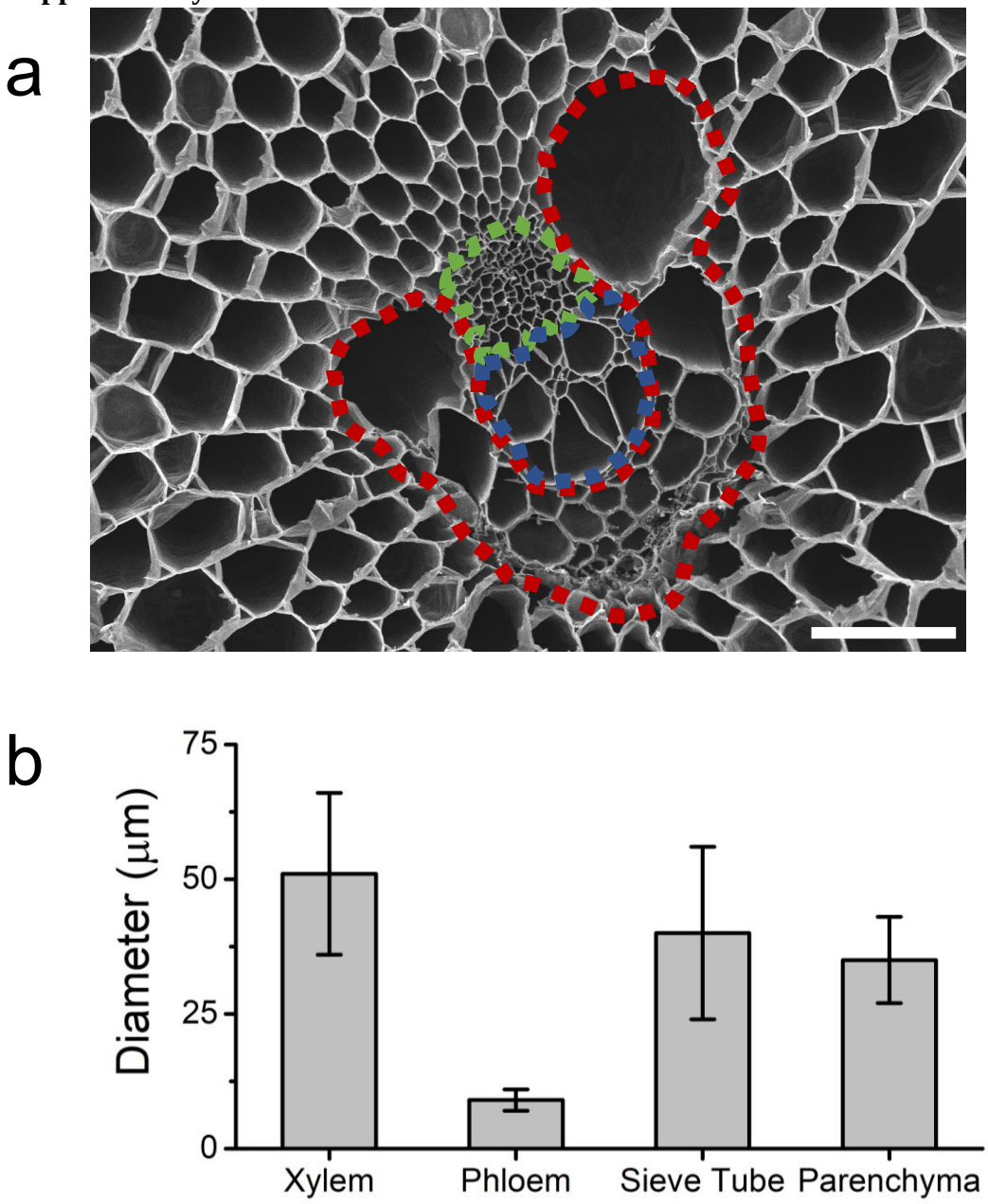

Supplementary Figure. 4.1 Different structures of the vascular bundle. a) A scanning electron microscope image of the surface of a decellularized scaffold revealing a single vascular bundle (VB) and surrounding parenchyma tissue (bar=100µm). The elements of the VB are highlighted to show the distinct channel architectures. The xylem (red) are channels that run the entire length of the asparagus and transport water within the plant. The phloem (blue) transport sugars within the asparagus from photosynthetic cells to non-photosynthetic cells. Phloem structures differ from xylem as they contain highly perforated sieve elements along their length. The sieve tubes are outlined in blue. The sieve tubes contain specialized cells with no nucleus that have roles in transporting carbohydrates/ messaging molecules throughout the plant. **b)** Characteristic diameters of the various elements of the vascular bundle, xylem channels (51±15µm), sieve tubes (40±16µm), parenchyma (35±8µm) and the phloem (9±2µm).

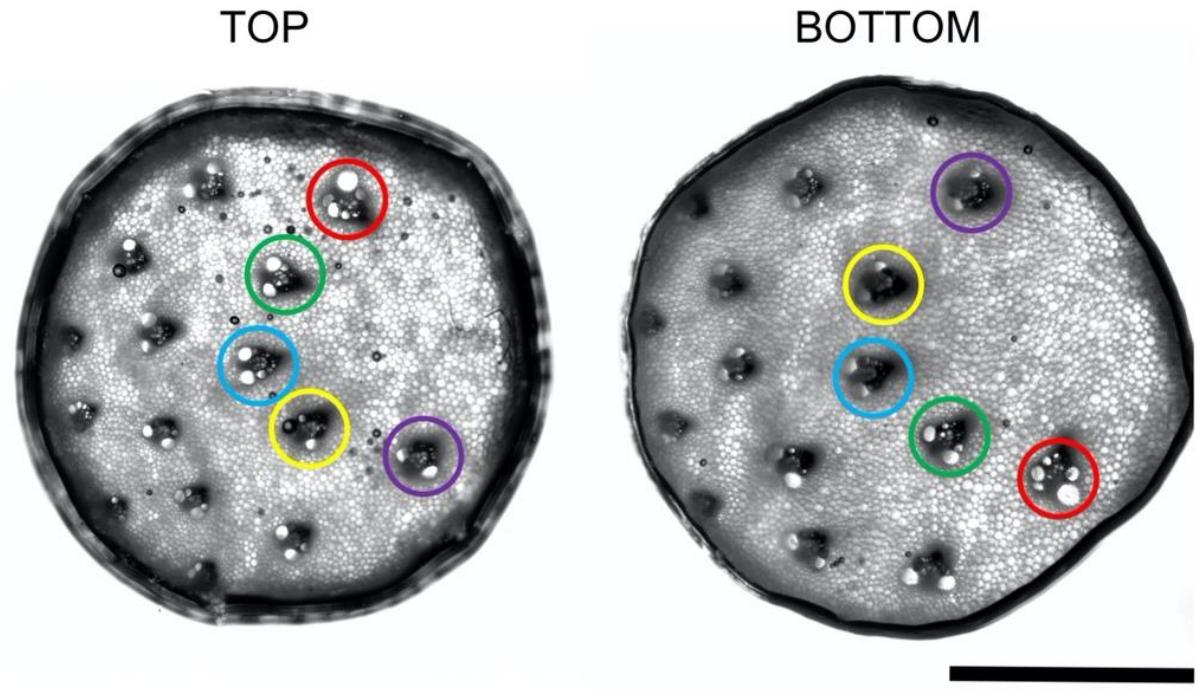

Supplementary Figure 4.2. The two opposite ends of a single decellularized scaffold. Phase contrast image of the entire surface of a typical scaffold reveals the distribution of the VBs. Notably, VBs on the top surface emerge in the nearly the same position in the bottom surface. Individual VBs are circled in different colours. As the scaffold is flipped over to image each side, the VB positions are also flipped (bar=2mm).

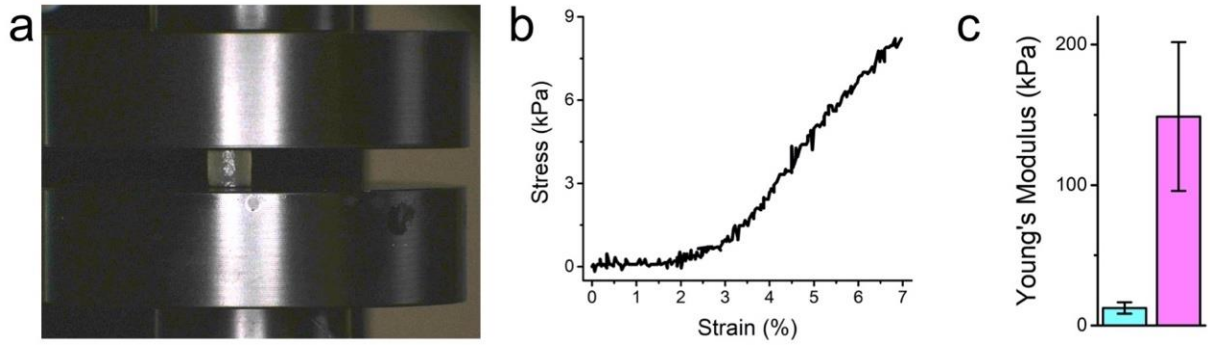

Supplementary Figure 4.3. The Young's modulus of the SCI scaffold prior to implantation. **a)** The SCI scaffold loaded into the CellScale UniVert compression platform. **b)** A typical stress-strain curve measured axially (parallel to the long axis) on a decellularized scaffold. **c)** The average young's modulus when measured axially (cyan, parallel to the long axis) and radially (purple, perpendicular to the long axis) to the long axis of the scaffold. The axial and radial young's modulus of the scaffolds is 148±53kPa (n=10) and 12±4kPa (n=10), respectively.

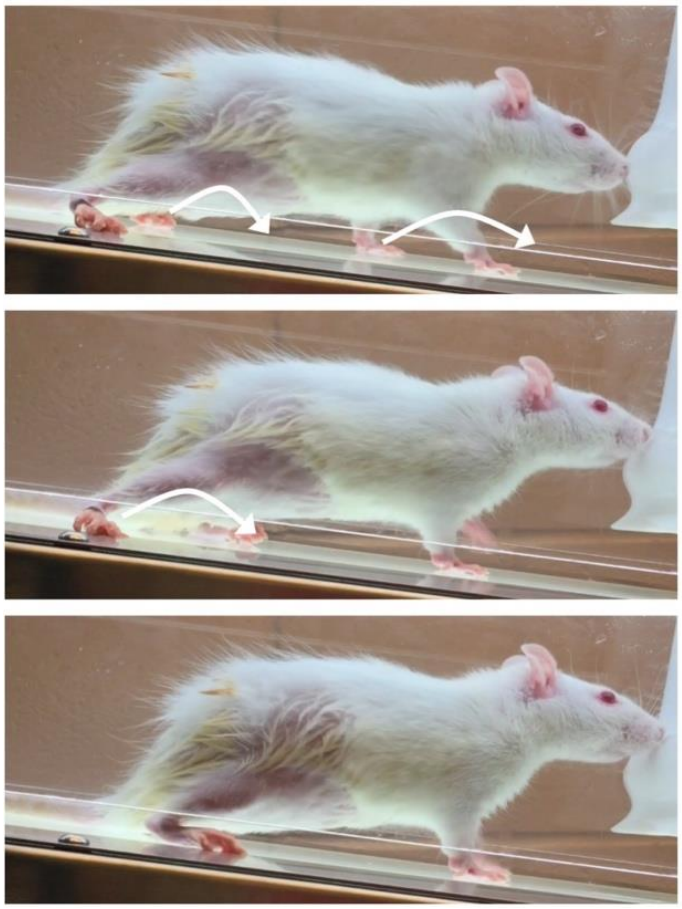

Supplementary Figure. 4.4. Coordinated hind and forelimb load-bearing steps in biomaterial-treated rats. Animals receiving the scaffold demonstrating continuing improved motor skills leading to forelimb-hindlimb coordination and load-bearing steps.

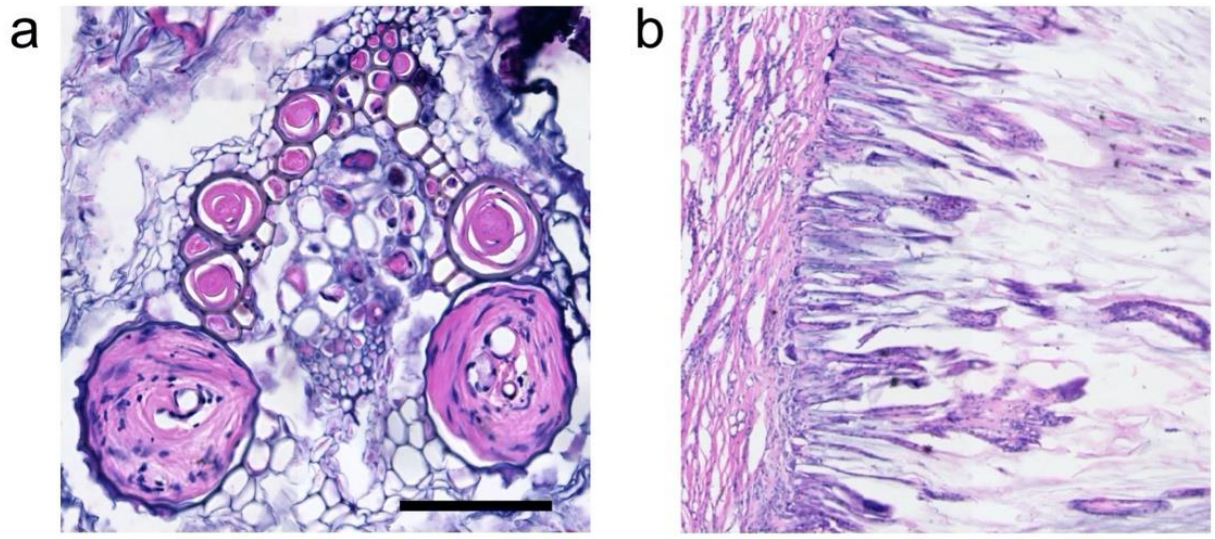

Supplementary Figure. 4.5. Hematoxylin and Eosin (H&E) staining after 28 weeks of implantation. a) Magnified axial view of a VB in the scaffold after 28 weeks of implantation. The majority of the infiltrating host cells are confined to the VBs; however, the parenchyma tissue is not void of cells (bar=200μm and applies to **b**). VBs throughout the scaffold are infiltrated with host cells consistent with Fig. 2. **b)** Magnified sagittal view of the scaffold spine interface. The VBs are also observed to be infiltrated with host cells. After 28 weeks, there is no clear degradation to the scaffold.

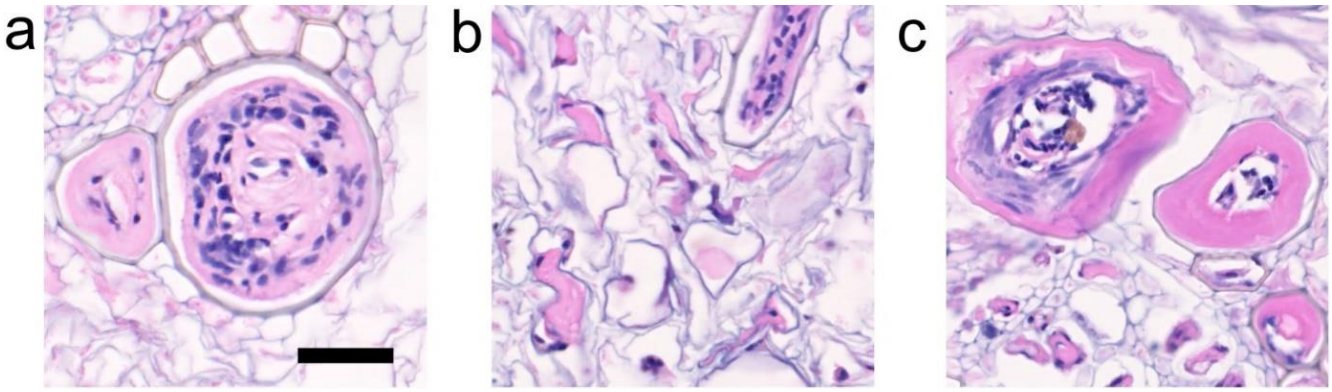

Supplementary Figure. 4.6. High magnifications of Hematoxylin and Eosin (H&E) staining demonstrating specific structures after 14 weeks of implantation. a) Granulation scar tissue can be seen in the xylem channels of the VB. This type of scar tissue typically prevents the extension of axons, however, in the scaffolds used in this study, granulation tissue is observed to be primarily sequestered in the xylem, leaving the rest of the surrounding parenchyma tissue available (bar=50μm and applies to all). **b)** Spindle-shaped nuclei of active fibroblasts can be seen in the surrounding parenchyma tissue. **c)** Blood vessels with thick endothelial linings can be observed throughout the VB and in the parenchyma tissue supplying host cells.

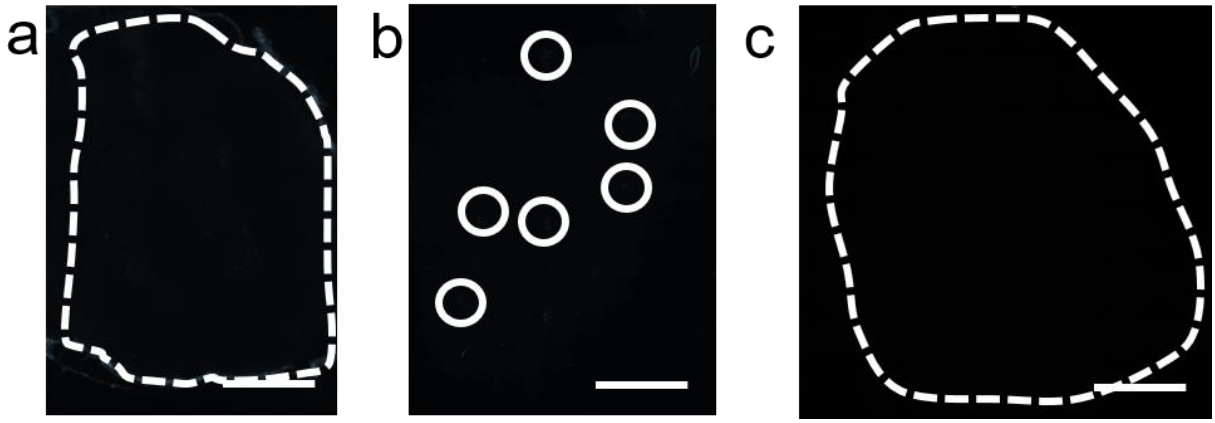

Supplementary Figure. 7. Fluoro-Gold retrograde axonal tracing control experiments 14 weeks post-injury.a) Axial spinal cord sections of the rostral end of the transection in a 14-week animal that did not receive a scaffold. There is a lack of FG signal throughout the spinal cord cross-section, with only a limited nonspecific signal observed in the spinal cord's dura (bar=500μm). The tissue is outlined with a white dotted line. **b)** Axial section of a non-implanted scaffold material directly loaded with 4% FG in a manner similar to the procedure performed at the secondary transection site. The FG does not adhere to the scaffold's cellulose or lignocellulose materials, leading to a lack of signal (bar=1mm). Individual VBs are circled in white. **c)** Axial spinal cord section of an animal that did not receive the FG stain (bar=500μm). All data presented here was acquired and processed with the same settings and parameters as the data presented in Fig. 4. The images primarily appear black due to the lack of signal as expected for these control experiments. The tissue is outlined with a white dotted line.

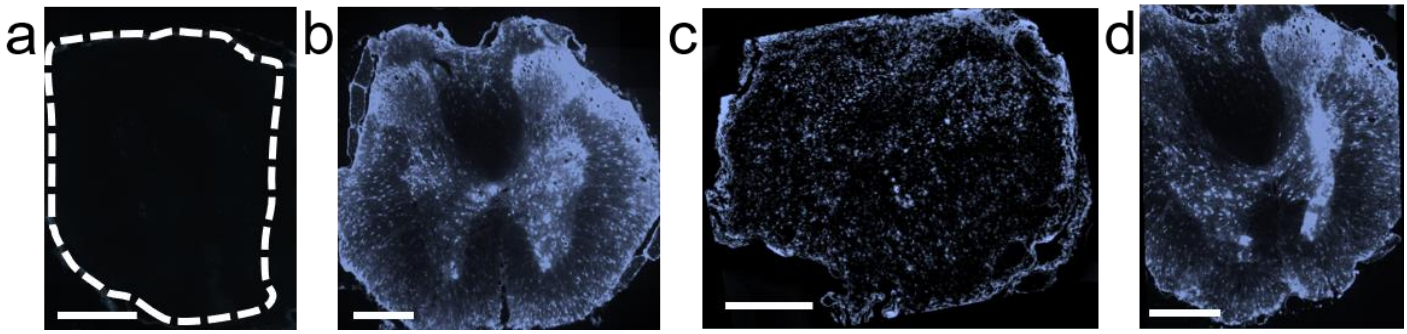

Supplementary Figure. 8. Fluoro-Gold retrograde axonal tracing in the rostral and caudal ends of the spinal cord 14 weeks post injury. a) Axial section of the spinal cord rostral to the injury site in an animal that did not receive scaffold. This is the same image from Supplementary Fig. 7a. Due to the lack of FG transport across the injury site, any observable signal is very low. Due to this, the tissue is outlined with a white dotted line to guide the reader (bar=500μm). **b)** Axial section of the spinal cord caudal to the injury site in an animal that did not receive scaffold. Unlike in **a**, neuron cell bodies labelled with FG are visible in the dorsal and ventral horns of the spinal cord as expected (bar=500μm). **c)** Axial section of the spinal cord rostral to the injury site in an animal that did receive a scaffold. Due to FG transport across the scaffold via projecting axons, some signal is observed in this part of the cord (bar=500μm). Interestingly, the diffuse pattern and distribution of FG positive axons qualitatively matches the distribution of NF200 positive axons that were imaged directly in the scaffold itself (Figure 4.3). **d)** Axial section of the spinal cord caudal to the injury site in an animal that did receive a scaffold, which appears very similar to **b** as expected (bar=500 μm). The results reveal that while axons can project through the scaffold, they do so in a manner that does not preserve the global morphology and architecture of the healthy tissue. However, this does not come at a surprise, given the extensive damage and trauma at the injury site.

FUTURE DIRECTIONS OF CELLULOSE BIOMATERIALS AND THE NEXT GENERATION OF CELLULOSE SCAFFOLDS TO TREAT SPINAL CORD INJURY

Daniel J. Modulevsky

5.1 Future direction of plant-derived scaffold modification

Plant-derived scaffolds face many obstacles that are yet to be solved before they can be effectively used to treat pathologies. Decellularized ECM tissues are held back by the techniques' limitations to recellularize the ECM with various cell types that are present natively. Typically, tissues have various cell types within the tissue, situated in site-specific areas that allow for its function. This is extremely difficult to replicate with current acellular ECM recellularization techniques. Although, several superficial tissues containing few cell types have been recellularized to replace failing tissue in humans, including bladders, veins, heart valves [357]. The Pelling Lab has already approached this issue of cell type interfacing within cellulose scaffolds by loading scaffolds with distinct cell types and layering them to create more complex tissues[96]. Although this is technique is promising and could result in several applications, the number of interfaces within any functional tissue remains too high. Plant scaffolds, similar to acellular ECM, face the same obstacles and can benefit from the adaption of the developed recellularization techniques established for acellular [358].

The vast majority of cells loaded onto cellulose scaffolds are established cell lines that are loaded onto the cellulose scaffold and allowed to passively adhere with our droplet technique (as described in Chapter2). This technique is successful in seeding the plant-derived cellulose scaffold, the efficiency is not sufficient, and as such, the number of cells required to seed an individual scaffold of 0.5 x0.5 cm is as high as $6x10^6$ cells. This approach is adequate when using an

established cell line. However, patient-derived primary cells proliferate much slower, and it may be unreasonable or impossible to proliferate such quantities of primary cells to be employed as a medical therapy[359].

As I describe in Chapter 1, ideal scaffolds (Figure 1.7) must have a surface chemistry that allows for modification and or conjunction of external therapeutic compounds and guidance cues (SCI specific strategies discussed later in this chapter). The work in this thesis has demonstrated that plant-derived cellulose scaffolds are capable of surface modifications. Still, much is left in developing techniques to chemically link external molecules to the cellulose chains while retaining the cell wall architecture. Fortunately, cellulose as a polymer has a broad chemical modifying capacity. With its countless industrial uses, a vast amount of cellulose chemistry research has been done to functionalize and modify the cellulose polymer[74]. That research has focused on using processed extracted cellulose polymers from plant sources. I hypothesize that these established techniques can be adapted to functionalize native cell wall polymers. As described in Chapter 1.5.3, cellulose microfibrils polymers have sequential regions of highly crystallized regions and amorphous regions[74]. These amorphous regions are ideal locations to target for chemical conjugation as they are distributed throughout the cellulose fibrils[74].

The plant, the cell wall surface has a more amorphous structure than the crystalline inner core of the cell wall [74]. The chemical conjugation is critical to the development of plant-derived cellulose scaffolds with functional mammalian cells. Other groups have attempted to load functional cardiomyocytes to observe limited contractile forces possibly attributed to the low adhesion compared to their native ECM counterpart[6]. Furthermore, it has been reported that cells cultured on the plant-derived cellulose scaffolds have a different physiology than when cultured *in vitro*[360].

These differences can be potentially minimized by modifying the cellulose's surface to mimic better the molecules found within the native ECM.

The work in this thesis has shown the functional capacity of the plant cell wall. However, to move plant-derived cellulose scaffolds forward, we must develop techniques that allow for surface conjugation to the degree of current synthetic platforms to allow injury-specific therapies coupled to the plant-derived cellulose scaffolds can be developed.

5.2 Combinatorial Therapies for SCI

It is doubtful that there will be one therapy that will successfully treat SCI pathologies in humans. It is much more likely that a combination of several therapies will be required to treat the myriad of acute and latent pathologies associated with SCI[361]. These combinatorial therapies include using SCI scaffolds loaded with stem cells, growth factors and drugs[26,128,129]. Although each combined therapy has a unique approach, the common theme is that scaffolds in combination display better recovery than the scaffold alone. Our cellulose scaffold showed significant promise for SCI; however, what recovery would be if the cellulose scaffold were loaded with stem cells, growth factors, drugs and or exosomes is still to be determined. In the following, I will discuss several approaches that can be combined with our cellulose scaffold.

5.3 Cell Loading

Stem cells play a critical role post-SCI as they can differentiate into specialized neuroprotective cells that replace injured tissue or recruit other cells by secreting factors[361,362]. Neural stem cells (NSC) are ideal candidates with scaffolds for SCI injuries as they differentiate fates committed to neurons or support glial cells. Oligodendrocytes are a form of glial cells that have been demonstrated to promote axon regeneration and myelination after SCI[362]. Further astrocytes support damaged tissue uptake within the microenvironment by secreting neurotrophic factors that promote NSC differentiation and axon proliferation[128,362]. NSCs without biomaterials have shown promise in SCI treatment; injecting NSC within the injury site resulted in an improved population of excitatory neurons that had projected into the

corticospinal tract [321,363]. In another study within primates, human NSC was shown to differentiate into neurons and glial cells observed to remodel the damaged local microenvironment. The NSC-differentiated neurons were demonstrated to interact between the damaged host axons [321,364]. In rats, after a complete transection, NSC-filled biomaterials recovered the hind limb with a BBB score of 6-7 while void scaffolds only recovered to 2-3[26]. Mesenchymal stem cells (MSC) are also a potential therapy and offer a massive benefit over NSC. MSC can be sourced from several different tissues from patients, adipose, placenta, umbilical, amniotic membrane and bone, thus removing the need to isolate patient-derived NSC [362,365]. As with NSC, MSC have been differentiated into neurons and glial cell types that have demonstrated improved recovery when transplanted into SCI [366]. MSC have long been shown to promote healing when added to the injury sites by secreting factors that regulate immune response, promoting angiogenesis, and anti-apoptotic factors[366]. MSC has shown promise when combined with a 3D biomaterial, the MSC was demonstrated to release neurotrophic factors that protect the injured spinal cord tissue and promote nerve regeneration[361,367]. Embryonic stem cells (ESCs) have unlimited self-renewal properties and differentiate into every cell line within the organism[321,368]. Several studies have shown the clinical potential of ESCs when injected into the SCI site. The ESCs lead to improved neurons' regeneration of axons' remyelination and re-establishing cortical neural circuits [323,366,369,370].

Additionally, ESCs were shown to diminish the injury core surrounded by glial scarring and improved motor recovery[120,128,321]. Induced pluripotent stem cells (iPSCs) have been investigated as they offer an alternative therapy since they remove all immune, ethical and clinical concerns[371]. Studies have found that iPSCs-derived NSCs differentiated into neurons that developed axons stemming from the injury site and formed synapsis with host neurons[372,373]. Olfactory ensheathing cells (OECs) can inhibit the inflammation after SCI injuries, resulting in lower glial scar and cavity formation[374]. Besides, OECs can secrete multiple growth factors that promote angiogenesis, axon projection and activity[375,376].

5.4 Growth Factors

Growth factors (GFs) are a cell-secreted biologically active molecule that can stimulate cell growth, proliferation, and cellular differentiation[377]. They have also shown endogenous roles during SCI in regulating neurons, neurotransmitters' release, and synaptic function recovery and promote the projection and remodelling of established axons[377]. Several GFs have been demonstrated to promote recovery in SCI models and will be in the table below. Each of the GFs can be chemically bonded to cellulose to stabilize latent SCI effects and promote recovery.

Growth Factor	Effect	Reference
• Neurotrophin-3 (NT-3) • Neurotrophin-4 (NT-4) • Neurotrophin-5 (NT-5)	• ↑ NSC differentiation to neuron • ↑ neuron cell growth	361
• Nerve Growth Factor (NGF)	• ↑ NSC differentiation to neuron • ↑ synapse formation of neurons • ↑ motor function recovery • ↑ neural network remodelling	378
• Brain-derived neurotrophic factor (BDNF)	• ↑ neuron cell growth • ↑ the regeneration and sprouting of axons • ↑ the remyelination of axons	377
• Glial cell derived neurotrophic factor (GDNF)	• ↓inflammation at the SCI site • ↓lesion volume of the SCI site • ↑pain management • ↑axon regeneration	379
• Fibroblast growth factors (FGFs) • FGF1 • FGF2 • FGF4 • FGF10	• ↓ latent injury pathologies • ↓ inflammation • ↓ astrocyte activation • ↑ the regeneration and sprouting of axons • ↑ angiogenesis	380
• Insulin-like growth factor 1 (IGF-1)	• Acts as antioxidant • ↑ the differentiation and survival of oligodendrocytes • ↑ the formation of regenerated axonal myelin sheath	381
• Ciliary neurotrophic factor (CNTF)	• ↑ the survival of damaged neurons • ↑ the survival of damaged oligodendrocytes • ↑ axon projection	382

Table 5.1. Growth factors that have demonstrated success in SCI and are potential loading factors with Cellulose scaffolds for SCI

5.5 Intermediate guidance cues to promote the axonal projection

Current SCI growth factors or cell are loaded into the scaffold in a static concentration the entire length. These approaches have shown promise in several animal models and *in vitro* [15,39,120,128,129,143,144,198,321–323,361–376,383,384]. However, several reports have demonstrated the inhibitory effects of axons travelling from the biomaterial (areas of high concentration of guidance) into the target tissue (lower concentration of guidance cues).[123,145,385,386] *In vivo*, the development of the embryo's nervous system is dependent on the innate ability of neurons to coordinate their projection of axons to reach their intended target, forming functional new neural circuits[145]. Depending on the neuron's nature, axons may need to navigate various tissues, and sometimes the entire length of the embryo, to find its exact intended neural circuit target[143]. The precision necessary for axon targeting is highlighted in the extreme adverse neurological disorders during flawed neural circuit development[144]. Similarly, after SCI, the neurons must re-establish their damaged connections by navigating across various scar tissues and biomaterials to repair existing or establish new circuits[321]. Understanding the molecular mechanisms that guide developing axons can inspire new treatments or therapies to treat SCI. (Chapter 1.9 Axonal Guidance Cues) It is essential to consider these intermediate guidance complex as a potential therapy that can be incorporated within SCI biomaterials instead of the current static guidance cues. As with the initial hypothesis of this thesis, I believe nature has already evolved a solution to axons' guidance that, if we better understand, we can adapt to potentially treat SCI in the form of a new SCI therapeutics.

DETAILED PROTOCOLS OF ESTABLISHED TECHNIQUES OF THIS THESIS

Daniel J. Modulevsky

6.1 Spinal cord Injury Surgery

The complete spinal cord transection model is the most severe form of the SCI model, as animals lose all lower-limb function and the ability to do autonomous bladder expression[110]. Nonetheless, the complete transection model is critical for researchers. It allows for obtaining statistically significant results to the biomaterial/pharmaceutical with fewer overall animals as the results can be directly attributed to the scaffold or pharmaceutical instead of animals' neural plasticity. This thesis established The Pelling-Tsai Complete SCI Surgery that was utilized in the last chapter. Because of the degree of invasiveness of the required surgery, every effort was taken to keep the surgical environment sterile to minimize any surgical infections. All the surgical procedures were done in adherence and approved by the University of Ottawa Animal Care and Veterinary Services ethical review committee. The attention to detail within the surgery and post-operative care did not affect the natural results, but I believe that extremely low mortality is attributed to our stringent protocols. Together with my team, I performed the surgery on 46 rats, not including the 30+ non-recovery rats practiced. The surgeries were completed by a team of 7+ individuals in several cohorts. Within the surgical room, there were 3 stations to form an assembly line allowing. The rat was removed from the animal housing room and brought to the operating room. At station 1 (Prep station), the technician weighed and placed the animal into the induction chamber. The animal was allowed to relax within the induction chamber prior to the start of the anesthesia (Isoflurane, Pharmaceutical partners of Canada). The oxygen flow rate was set to 2L/min with 4%

Isoflurane. The animal was observed until the animal was at stage II of the surgical anesthetic plane, at which point the isoflurane was reduced to 2.5%. When the rat demonstrated the onset of automatic breathing, and the animal did recover body position, the rat was moved from the induction chamber to a heated procedural table of the first station. The rat was fitted into the head-isoflurane cone with tear gel applied to both eyes. The animal was left for several moments (under supervision) before a toe pinch was done to confirm that the rat is under stage III of the anesthetic plane. The technician then shaved the rat's dorsal surface from the cervical-6 to thoracic-13 vertebrae against the grain. The fur was cleared with a handheld vacuum prior to cleaning the exposed skin with distilled water and soap (Endure 400). After the skin was cleaned from larger impurities, the skin was sterilized using chlorhexidine 4% W/V. The technician then prepared two separate injections for the rat, including enrofloxacin (Baytril) (10mg/kg) and saline (Baxter) 0.9% NaCl (5mL/kg), which were injected into three distant injection sites that did not overlap the T8-T9 vertebrae. The locations of the sites were recorded and monitored for any symptoms of necrosis. At this point, the animal was transferred to Station 2 where the laminectomy and transection were performed. At station 2, the rat was placed into a stereotactic apparatus with the head was secured by securing the earpieces. The fore, back limbs, and tail of the rat were stretched and taped to stabilize and to ensure no slippage during the surgical procedure. The animal's breathing was continuously monitored to ensure the animal maintained stage III of the anesthetic plane. The two surgeons situated on opposite sides of the rats wore sterile gowns and maintained a sterile environment. The surgeon performed a final toe pinch to confirm the anesthetic plane of the animal. The surgical site was again sterilized with chlorhexidine 4% before the first incision. The second thoracic vertebra (T2) was located by running a finger down the spine and locating the most prominent vertebrae. The finger was moved caudally, counting the individual spinal process

until reaching the T8-T9 vertebrae. The vertebrae location was marked to note the site of the incision. A 1-2 cm incision was made with a scalpel over the marked T8-T9 vertebrae to cut through the epidermis, dermis, and subcutaneous fat layers to expose the underlying dorsal muscles. The vertebrae's muscle tissue was cut away from the spinal processes until all four lamina lobes were uncovered. The laminectomy was performed by securely holding the spinal process with rat forceps and sliding the flat side of malleus nipples under the 8^{th} lamina from the rat's caudal end. Carefully, the lamina was sniped and slowly lifted to minimize vertebrae shards applying pressure to the spinal cord. The removal of the spinal processes will result in bleeding that has to be controlled prior to proceeding to the exposed spinal cord. Blood was continually removed from the surgical plane to maintain a proper visual of the spinal cord. The rat's breathing should be monitored throughout the procedure, adjusting the oxygen flow rate and isoflurane. A surgical microscope was used to cut the pia mater, arachnoid and dura mater with micro-scissors without cutting the spinal cord. The exposed spinal cord was lifted with a modified dental hook surgical tool to lift the cord from the vertebral foramen and cut in a single motion with the micro scissors. It was common for the rat to have a reflex kick when the spinal cord was lifted or cut. The process of cutting the spinal cord resulted in significant bleeding between the spinal cord stumps, Surgifoam (Ethicon) was placed between the stumps to control the bleeding. Once the bleeding was stabilized and the surgifoam removed, the intra-gap distance was measured. The stumps were lifted to ensure full transection with the sensory and motor fibres of T8-T9 were cut. The animal was randomly assigned to the biomaterial or control group after the transection. Biomaterial animals received a scaffold that best matched the stumps' intragap distance, and 0.2 mL of Fibrin glue (Tisseel) was used to stabilize the scaffold's dorsal surface. Control animals just received the fibrin glue with no biomaterial. When the fibrin has stabilized, the incision was closed

in several steps. The muscle and subcutaneous fat layers were closed with 3-0 Vicryl suture material with a surgeon's knot going into a simple continuous suture pattern ending with another surgeon's knot. The animals were given a dose of slow-release buprenorphine (0.05mg/kg). then taken to station 3. The animals were taken off isoflurane while closing the epidermis and dermis layers with 9 mm Michel clips. A numbing agent of 2% Bupivicane (Chiron) was applied to the surrounding skin in contact with the Michel clips. The rats were returned to their cages with a soft paper bedding with DietGel (ClearH20) and cheerios. 4 hours later, additional buprenorphine (1mg/kg) was administered to ensure no pain sensation during recovery. The animals were monitored for 72 hours for any symptoms of pain.

6.2 Retrograde Tracer Surgery

The retrograde surgery required a second complete transection at the T13 vertebrae. The surgery followed the same protocol as the initial SCI. Except for that, no biomaterial or fibrin glue was applied, and the laminectomy/transection was at the T12-T13 vertebrae. Rats from the biomaterial and controls were randomly selected at both time points (14 and 28 weeks) to undergo a retrograde tracer. After the laminectomy and transection of the spinal cord, surgifoam (Ethicon) soaked in 10 µL of 4% FluoroGold (Fluorochrome) in saline was placed onto the rostral end of the spinal cord stump. Petroleum jelly (Sherwood Medical) was then applied (in place of the fibrin glue) to stabilize the surgifoam into place and prevent nonspecific labelling before the muscles were then closed with 3-0 Vicryl. The rats were monitored for a week to allow the FG to travel through the spinal cord's full length.

6.3 Animal Care

The complete transections SCI is intrusive on the animals, and as such, post-operative animal care becomes critical to restoring the health of the animals following the surgery. The attention to detail in animal care was to reduce animal suffering and the overall number of animals for the study. After the surgery, the animals are at their most vulnerable. Post-surgery, the animals may have difficulty masticating the 2018 Rodent pellets. The pellets were dissolved in water to form a semi-stable paste that could be easily formed into a puck shape to mediate this. The pellet puck was left in the cage, allowing the animal easy access to the food instead of the food rack on the cages' top.

Additionally, bite marks are readily observable on the pucks' polished surface to observe food consumption. Dietary supplements of Cheerios and Diet Gel were also provided to the animals to supplement weight gain after the surgeries. The animals were placed in low-hanging rodent cages with modified lids and angled water drip bottles. Altogether, these gave the animals enough clearance space to move around the cage with access to food pellets at the cage's top and the water drip spigot. Animals were monitored at 3-time points every day at 6 am, 2 pm, and 10 pm. Each of the daily check-ups followed the same flow chart and are outlined below. At each time point, all the rats were quickly checked for any significant issues. One at a time, an individual cage was removed from the rack and placed onto the procedure table; the water bottle was checked for consumption. The lid was then removed from the cage, and the rat was assessed for a pain/grimace score. The weight of the rat was recorded at the morning inspection to monitor weight gain. A 5% weight loss overnight would result in diet supplements in cheerios or diet gel. The rat was then carefully picked up with both hands and closely inspected for any autophagia. The bladder of the rats was massaged with two fingers until the bladder of the rat was expressed. The urine's colour and clarity were observed and recorded if any blood or cloudy particles were observed. If the

symptoms persisted, the animals were flagged for vet inspection for potential UTI. Following the initial surgery, the bladder was difficult to manually express as the muscle surrounding the bladder had not atrophied. When a bladder could not be expressed with gentle massaging, the rat was placed in a warm bath until the bladder was finally expressed. Rats could not express themselves after the surgery, so it was critical to express the bladder at every check so as to prevent any chance of bladder rupture that would ultimately lead to euthanizing the animal. The animal's dehydration was assessed by pinching the rat's skin and observing how the skin returned to its original position. Following the inspection, the animal was returned to the cage, and the cage spoiled bedding was replaced. The cage's lid was returned, and the cage with the rat was placed back onto the rack. At the end of each check, a line was drawn on the water bottle at the current water level to assess the water consumption at the next inspection. All relevant information was recorded in the animal's daily charts for review at the next check. The animals had their cages and bottles' exchanged weekly. If the animal requires a subcutaneous injection of antibiotics or extreme dehydration, it was handled with the burrito technique. The animal was wrapped fabric, like a burrito, to support the spinal cord during the injection procedure. A skin tent was created on the dorsal side with the index and middle finger. The needle was inserted through the skin with the bevel up at a 45^{o}. The location of the needle was recorded in the case of any skin tissue necrosis. After the surgery, the rats could not groom themselves; as such, animals that required grooming were gently washed in a warm water bath and dried before returning to the cage. The nails were clipped while the animal was under general anesthetic. All the animals had their BBB scores assessed every week after the afternoon expression. The animals were transported to the BBB room, where they were individually placed in a 1-meter diameter BBB arena and allowed to explore for 5 minutes. The rats were recorded from two viewpoints to be scored.

6.4 Perfusion and Tissue Harvesting

At the end of the study, the animals had to be euthanized and perfused prior to tissue harvesting. The euthanization was done in adherence and approved by the University of Ottawa Animal Care and Veterinary Services ethical review committee. Animals were euthanized in their cages with an intraperitoneal injection (IP) of euthanyl based on the rat's final weight (750 mg/kg). The rats were carefully lifted from the cage using the burrito method, and an IP injection was given to the right side of the umbilicus's animal midline. After the injection, the animal was returned to their cage and was monitored for the euthanyl effects. Typically, the rat was ready in 20 minutes, but this time could vary depending on the rat's condition. A toe pinch (done on the forelimb instead of the back limb) confirms the animal was under deeply enough while the heart was still beating. It was critical to perform the perfusion while the heart was still beating to ensure the PFA's proper flow throughout the cardiovascular system. The rat was then transferred to the necropsy room with the perfusion equipment set up in the ventilated hood. A perfusion pump was set up with 4% PFA reservoirs, and heparinized saline (20 units /mL) solution was kept on ice. The pump was run to bleed the tubing with saline and checked for any bubbles anywhere in the system. If a bubble was observed, it was immediately agitated until removed from the perfusion line. The pump was adjusted so that the flow rate was 20 mL/min. On the necropsy table, a final toe pinch was done to confirm the animal was non-responsive. Quickly, the abdomen's skin was pulled to create a tent with a hemostat tweezer followed by a cut through the abdominal musculature from the sternum to expose the diaphragm. Scissors were used to cut along both sides of the abdomen along the surface of the rib cage. It was critical not to cut any of the visceral organs or any tissue to ensure uninterrupted perfusion. The diaphragm from the ribs to the shoulder was cut and folded back with another hemostatic tweezer. The pericardial membrane around the heart was cut away. The perfusion pump exit line-linked with a 10 gauge surgical needle was inserted into the left ventricle

just enough to pass through one side of the ventricle muscle wall and held in place with hemostatic tweezers without pinching the tip of the needle to ensure proper flow. The pump was activated and set to a flow rate of 20 mL/min; once the saline was confirmed to be flowing through the left ventricle, scissors were used to cut the right atrium. Blood should immediately start pooling within the thoracic cavity. Within a couple of minutes, the liver should become clear of blood and turn to a dull brown colour. The pump should run for 13 minutes or until 250 mL of heparinized saline has run through the animal. When switching to 4% PFA solution, the pump was turned off, and the inflow line was clamped before switching to the PFA beaker to ensure no air bubbles in the perfusion line. The pump was then turned once again and let run for 13 minutes now with 4 % PFA. The tissue should be twitching due to the muscle fibres' PFA contraction. The twitching confirms that the PFA solution is correctly perfused throughout the tissue. The animal should be completely stiff at this point. When complete, the pump was turned off, and the 10 gauge needle was removed. The animal is moved from the vented hood to a necropsy table where the dissection was performed. The system was purged with water through the pump system for 10 minutes before the next animal. The skin of the animal is removed by pulling the skin from the tissue and cutting it with scissors. The lower end of the animal is cut away at the hips through the spinal column. The spinal column and the skull of the animal were then cut away from the remaining tissue. The remaining spinal column and skull had as much musculature tissue removed. The bone snappers are carefully inserted into the vertebral foramen to snip the spinal column's entire posterior process from the rostral end. The spinal column's dorsal surface was lifted up to reveal the caudal vertebra required to cut next. With great care, a laminectomy was performed over the entire spinal column. Once reaching the T8-T9, the surgeon was informed if the animal received a biomaterial or not. The control spinal cords were much less adhered to and could easily fall apart than the biomaterial

animals with spinal cord stumps fused to the biomaterial. When the cervical 1 vertebra was reached, the spinal columns were cut away. Ronguers were carefully slipped into the foramen magnum, and the skull was carefully snapped away in small pieces working over the dorsal surface to the bone case's frontal bone. Be sure to use the rongeurs to crack the bone above the olfactory bulbs to take them out. The brain dura was removed, and the bony tissue connecting the cerebrum to the cerebellum was cut from the olfactory bulbs. The brain was then removed from the seat of the skull with the spinal cord. The spinal cord was then carefully lifted from the remaining spinal column's rostral end, and the peripheral nerves were cut away. After cutting away the peripheral nerves or any tissue holding the spinal cord, the cord was lifted slightly to remove the peripheral nerves. Once reaching the brain, the entire CNS can be removed and placed into a 50 mL falcon tube with 4 % PFA. The tissue was kept at 4^0C in PFA for 48 hours before switching to 20% sucrose solution with 0.1% sodium azide overnight at 4ºC. The tissue should be buoyant at this point and should be left for another 12 hours if not. Cut out the section of the spinal cord containing the biomaterial or the injury for freezing and sectioning. Animals receiving the retrograde fluorogold had the entire spinal cord frozen in sections labelled Brain, A, B, C, D, E, and F.

6.5 Microscopy and Linear Unmixing

Hematoxylin and eosin-stained slides were scanned with the Zeiss AxioScan Z1 slide Scanner (Zeiss) equipped with 10x objective at the Ottawa Cancer Research center. The slides were loaded into the scanner with the contrast/gamma adjusted so an initial web-camera scan could pick that tissue to locate the tissue within the slides. Once an appropriate contrast and gamma level were identified that allowed tissue to be automatically detected, a simple macro was written to locate tissue on each of the 5 slides loaded into the microscope. The slides were then scanned and stitched

with Zeiss AxioScan Z1 with a 10X objective. The files were analyzed using ZenBlue (Zeiss, Canada) and ImageJ software. Fluorescence imaging of tissue sections stained with NF200 and GFAP antibodies was carried out on a Nikon A1RsiMP Confocal Workstation with a 32-detector array for spectral imaging with 6 nm resolution detectors (Nikon). Multiple ROI was taken from each of the slides. Every ROI from the slide was a Z-stack with both discrete DAPI channels (405 Excitation, 450/50 Filter Cube) and Alx568(561 excitations, 595/50 Filter cube) and with spectral imaging 32-detector array for spectral imaging with 6 nm resolution detectors (545 – 731 nm) done separately. As lignocellulose can be autofluorescent, imaging negative control scaffolds can achieve spectral linear unmixing to obtain autofluorescence spectra. The lignocellulose was identified using both the discrete channel and spectral image with multiple ROI that were selected on the spectral image. The autofluorescence spectra were stored on the Nikon Elements store spectrum setting. The spectrum of the autofluorescence was easily distinguished from the bell-shaped spectra of an Alexa568 fluorescent probe. The spectral profile of the 568 antibodies was then unmixed from any scaffold autofluorescence, and the resulting unmixed z-stack was 3D deconvolved to create a max projection. The DAPI channel was max projected separately and overlaid over the unmixed spectrum. Although both antibodies have the same 568nm wavelength fluorophore, NF200 data is presented as false-colour green images to distinguish false-colour red GFAP data for clarity. FG slides samples were imaged with a Nikon Ni-U Ratiometric Fluorescence Microscope with a 340/380 filter set. All image processing was carried out with Nikon Elements software (Nikon).

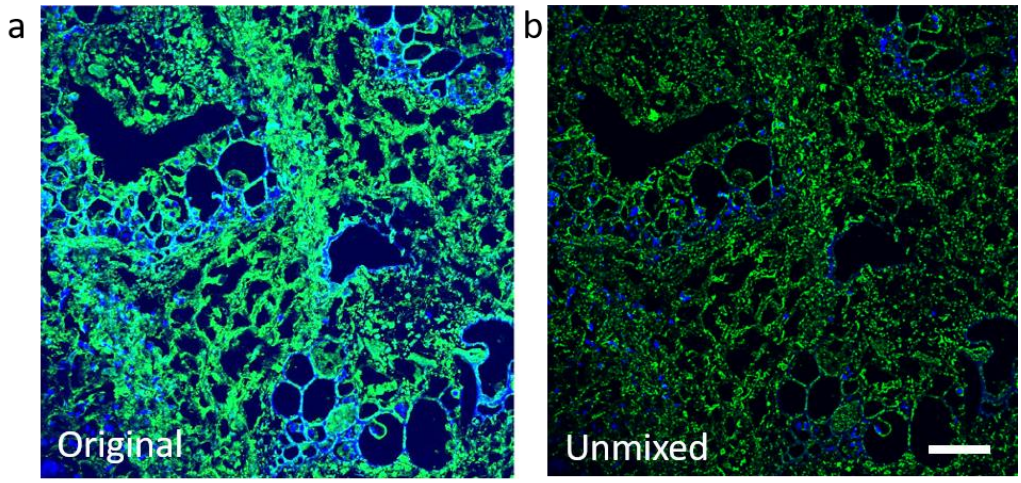

Figure 6.1 The SCI scaffold stained with NF200 (green) and Dapi (blue) captured with discrete channels and spectral imaging to remove the natural SCI scaffolds autofluorescence. a) Fluorescence imaging of tissue sections stained with NF200 and GFAP antibodies was carried out on a Nikon A1RsiMP Confocal. As lignocellulose can be autofluorescent, imaging negative control scaffolds can achieve spectral linear unmixing to obtain autofluorescence spectra. a) The original before any unmixing, **b)** The spectral profile of the 568 antibodies was then unmixed from any scaffold autofluorescence, and the resulting unmixed z-stack was 3D deconvolved to create a projection. The lignocellulose scaffolds are not present in the unmixed version, confirming the presence of axons positive for NF200. (Scale bar =100 µm)

Chapter 7|References

1. Cavalier-Smith, T. A revised six-kingdom system of life. *Medicine Biology* (1998) doi:10.1111/j.1469-185X.1998.tb00030.x.

2. Hudecki, A., Kiryczyn, G. & Łos, M. J. Biomaterials Definition,. in *Stem Cells and Biomaterials for Regenerative Medicine* 85–98 (Elsevier, 2019). doi:10.1016/B978-0-12-812258-7.00007-1.

3. Ott, H. C. *et al.* Perfusion-decellularized matrix: using nature's platform to engineer a bioartificial heart. *Nat. Med.* **14**, 213–221 (2008).

4. Lu, T. Y. *et al.* Repopulation of decellularized mouse heart with human induced pluripotent stem cell-derived cardiovascular progenitor cells. *Nat. Commun.* **4**, 1–11 (2013).

5. Liu, H., SLAMOVICH, E. & Webster, T. J. Less harmful acidic degradation of poly (lactic- co-glycolic acid) bone tissue engineering scaffolds through titania nanoparticle addition. *Int. J. Nanomedicine* **1**, 541–545 (2006).

6. Gershlak, J. R. *et al.* Crossing kingdoms: Using decellularized plants as perfusable tissue engineering scaffolds. *Biomaterials* **125**, 13–22 (2017).

7. Lee, J., Jung, H., Park, N., Park, S. H. & Ju, J. H. Induced Osteogenesis in Plants Decellularized Scaffolds. *Sci. Rep.* **9**, 1–10 (2019).

8. Fontana, G. *et al.* Biofunctionalized Plants as Diverse Biomaterials for Human Cell Culture. *Adv. Healthc. Mater.* **6**, 1601225 (2017).

9. Adamski, M. *et al.* Two Methods for Decellularization of Plant Tissues for Tissue Engineering Applications. *J. Vis. Exp.* e57586 (2018) doi:10.3791/57586.

10. Cheng, Y.-W., Shiwarski, D. J., Ball, R. L., Whitehead, K. A. & Feinberg, A. W. Engineering Aligned Skeletal Muscle Tissue Using Decellularized Plant-Derived Scaffolds. *ACS Biomater. Sci. Eng.* **6**, 3046–3054 (2020).

11. Phan, N. V., Wright, T., Rahman, M. M., Xu, J. & Coburn, J. M. In Vitro Biocompatibility of Decellularized Cultured Plant Cell-Derived Matrices. *ACS Biomater. Sci. Eng.* **6**, 822–832 (2020).

12. Contessi Negrini, N., Toffoletto, N., Farè, S. & Altomare, L. Plant Tissues as 3D Natural Scaffolds for Adipose, Bone and Tendon Tissue Regeneration. *Front. Bioeng. Biotechnol.* **8**, 1–15 (2020).

13. Toker, M. *et al.* Decellularization and characterization of leek: a potential cellulose-based biomaterial. *Cellulose* **27**, 7331–7348 (2020).

14. Ratner, B. D., Hoffman, A. S., Schoen, F. J. & Lemons, J. E. *Biomaterials science: an introduction to materials in medicine*. *Chemical Engineering* (2004).

15. Wiley, J. *et al.* History of Biomaterials. *Biomaterials* 1–10 (2014) doi:10.1002/9781119043553.ch1.

16. Hildebrand, H. F. Biomaterials - a history of 7000 years. *BioNanoMaterials* **14**, 119–133 (2013).

17. Sarwar, H. & Modi, N. Sir Harold Ridley: Innovator of cataract surgery. *J. Perioper. Pract.* **24**, 210–212 (2014).

18. Moore, D. B., Harris, A. & Siesky, B. The world through a lens: The vision of Sir Harold Ridley. *Br. J. Ophthalmol.* **94**, 1277–1280 (2010).

19. Patel, A. S. *Intraocular Lens Implants: A Scientific Perspective*. *Biomaterials Science: An Introduction to Materials: Third Edition* vol. 34 (Elsevier, 2013).

20. Hench, L. L. & Thompson, I. Twenty-first century challenges for biomaterials Subject collections Twenty-first century challenges for biomaterials. *J. R. Soc. Interface* **7**, S379–S391 (2010).

21. Major, M. R., Wong, V. W., Nelson, E. R., Longaker, M. T. & Gurtner, G. C. The Foreign Body Response: At the Interface of Surgery and Bioengineering. *Plast. Reconstr. Surg.* **135**, 1489–1498 (2015).

22. Kattula S, JR, B. & Wolberg AS. Fibrinogen and fibrin in hemostasis and thrombosis. *Arterioscler. Thromb. Vasc. Biol.* **37**, e13–e21 (2017).

23. Chen, F.-M., Liu, X., Polym, P. & Author, S. Advancing biomaterials of human origin for tissue engineering HHS Public Access Author manuscript. *Prog Polym Sci* **53**, 86–168 (2016).

24. Saini, M. Implant biomaterials: A comprehensive review. *World J. Clin. Cases* **3**, 52 (2015).

25. Colas, A. & Curtis, J. Silicones. *Biomater. Sci. An Introd. to Mater. Third Ed.* 82–91 (2013) doi:10.1016/B978-0-08-087780-8.00010-3.

26. Koffler, J. *et al.* Biomimetic 3D-printed scaffolds for spinal cord injury repair. *Nat. Med.* (2019) doi:10.1038/s41591-018-0296-z.

27. Cartilage-like hydrogel promises 3D-printable knee implants. https://newatlas.com/3d-printed-hydrogel-knee-implants/49161/.

28. Heath, D. E. & Cooper, S. L. Polyurethanes. *Biomater. Sci. An Introd. to Mater. Third Ed.* 79–82 (2013) doi:10.1016/B978-0-08-087780-8.00009-7.

29. Ratner, B. D. A History of Biomaterials. *Biomater. Sci. An Introd. to Mater. Third Ed.* xli–liii (2013) doi:10.1016/B978-0-08-087780-8.00154-6.

30. Ratner, B. D. *Introduction: The Body Fights Back - Degradation of Materials in the Biological Environment*. *Biomaterials Science: An Introduction to Materials: Third Edition* (Elsevier, 2013). doi:10.1016/B978-0-08-087780-8.00059-0.

31. Bahram, M., Mohseni, N. & Moghtader, M. An Introduction to Hydrogels and Some Recent Applications. in *Emerging Concepts in Analysis and Applications of Hydrogels* (InTech, 2016). doi:10.5772/64301.

32. Hoffman, A. S. The early days of PEG and PEGylation (1970s–1990s). *Acta Biomater.* **40**, 1–5 (2016).

33. Kar, M., Vernon Shih, Y.-R., Velez, D. O., Cabrales, P. & Varghese, S. Poly(ethylene glycol) hydrogels with cell cleavable groups for autonomous cell delivery. *Biomaterials* **77**, 186–97 (2016).

34. Hoffman, A. S. & Hubbell, J. A. *Surface-Immobilized Biomolecules*. *Biomaterials Science: An Introduction to Materials: Third Edition* (Elsevier, 2013). doi:10.1016/B978-0-08-087780-8.00032-2.

35. Kubinová, Š. Biomaterials and Magnetic Stem Cell Delivery in the Treatment of Spinal Cord Injury. *Neurochem. Res.* **45**, 171–179 (2020).

36. Novikova, L. N., Novikov, L. N. & Kellerth, J. Biopolymers and biodegradable smart implants for tissue regeneration after spinal cord injury. *Curr. Opin. Neurol.* 711–715 (2003)

doi:10.1097/01.wco.0000102620.38669.3e.

37. Peng, R., Yao, X., Cao, B., Tang, J. & Ding, J. The effect of culture conditions on the adipogenic and osteogenic inductions of mesenchymal stem cells on micropatterned surfaces. *Biomaterials* **33**, 6008–19 (2012).

38. Ratner, B. D. *Surface Properties and Surface Characterization of Biomaterials*. *Biomaterials Science: An Introduction to Materials: Third Edition* (Elsevier, 2013). doi:10.1016/B978-0-08-087780-8.00005-X.

39. Straley, K. S. *et al.* Biomaterial Design Strategies for the Treatment of Spinal Cord Injuries. *J. Neurotrauma* **27**, 1–19 (2010).

40. Pontes Soares, C. *et al.* 2D and 3D-organized cardiac cells shows differences in cellular morphology, adhesion junctions, presence of myofibrils and protein expression. *PLoS One* **7**, e38147 (2012).

41. Boni, R., Ali, A., Shavandi, A. & Clarkson, A. N. Current and novel polymeric biomaterials for neural tissue engineering. *J. Biomed. Sci.* **25**, 1–21 (2018).

42. Lin, C. C. & Anseth, K. S. *The Biodegradation of Biodegradable Polymeric Biomaterials*. *Biomaterials Science: An Introduction to Materials: Third Edition* (Elsevier, 2013). doi:10.1016/B978-0-08-087780-8.00061-9.

43. Li, X. *et al.* Scaffold-facilitated locomotor improvement post complete spinal cord injury: Motor axon regeneration versus endogenous neuronal relay formation. *Biomaterials* **197**, 20–31 (2019).

44. Almany, L. & Seliktar, D. Biosynthetic hydrogel scaffolds made from fibrinogen and polyethylene glycol for 3D cell cultures. *Biomaterials* **26**, 2467–77 (2005).

45. Liao, J., Joyce, E. M. & Sacks, M. S. Effects of decellularization on the mechanical and structural properties of the porcine aortic valve leaflet. *Biomaterials* **29**, 1065–1074 (2008).

46. Cavalcanti-Adam, E. A. *et al.* Cell Spreading and Focal Adhesion Dynamics Are Regulated by Spacing of Integrin Ligands. *Biophys. J.* **92**, 2964–2974 (2007).

47. Nelson, C. M., VanDuijn, M. M., Inman, J. L., Fletcher, D. A. & Bissell, M. J. Tissue Geometry Determines Sites of Mammary Branching Morphogenesis in Organotypic Cultures. *Science (80-.).* **314**, 298–300 (2006).

48. McBane, J. E., Sharifpoor, S., Cai, K., Labow, R. S. & Santerre, J. P. Biodegradation and in vivo biocompatibility of a degradable, polar/hydrophobic/ionic polyurethane for tissue engineering applications. *Biomaterials* **32**, 6034–44 (2011).

49. Tong, X. & Yang, F. Engineering interpenetrating network hydrogels as biomimetic cell niche with independently tunable biochemical and mechanical properties. *Biomaterials* **35**, 1807–15 (2014).

50. Trensz, F., Scimè, A. & Grenier, G. Skeletal Muscle Engineering: The Need for a Suitable Niche Frédéric. in *Tissue Engineering in Regenerative Medicine, Stem Cell Biology* (ed. Bernstein, H. S.) 197–209 (Humana Press, 2011). doi:10.1007/978-1-61779-322-6.

51. Ratner, B. D. & Horbett, T. A. *Evaluation of Blood-Materials Interactions. Biomaterials Science: An Introduction to Materials: Third Edition* (Elsevier, 2013). doi:10.1016/B978-0-08-087780-8.00055-3.

52. Zhu, W. *et al.* 3D printing of functional biomaterials for tissue engineering. *Curr. Opin.*

Biotechnol. **40**, 103–112 (2016).

53. Liu, S., Schackel, T., Weidner, N. & Puttagunta, R. Biomaterial-Supported Cell Transplantation Treatments for Spinal Cord Injury: Challenges and Perspectives. *Front. Cell. Neurosci.* **11**, 430 (2018).

54. Narayan, R. J. The next generation of biomaterial development. *Philos. Trans. R. Soc. A Math. Phys. Eng. Sci.* **368**, 1831–1837 (2010).

55. Haycock, J. W. 3D Cell Culture: A Review of Current Approaches and Techniques. *Methods Mol. Biol.* **695**, 1–15 (2011).

56. RK, K., KC, P., C, N. & F, L. Polylactic acid for surgical implants. *Arch. Surg.* **93**, (1966).

57. Lü, J.-M. *et al.* Current advances in research and clinical applications of PLGA-based nanotechnology. *Expert Rev. Mol. Diagn.* **9**, 325 (2009).

58. Siddiqui, H. A., Pickering, K. L. & Mucalo, M. R. A Review on the Use of Hydroxyapatite-Carbonaceous Structure Composites in Bone Replacement Materials for Strengthening Purposes. *Materials (Basel).* **11**, (2018).

59. Heath, D. E. & Cooper, S. L. *Polymers: Basic Principles*. *Biomaterials Science: An Introduction to Materials: Third Edition* (Elsevier, 2013). doi:10.1016/B978-0-08-087780-8.00008-5.

60. Wells, C. M. *et al.* Stimuli-Responsive Drug Release from Smart Polymers. *J. Funct. Biomater.* **10**, (2019).

61. Prestwich, G. D. & Atzet, S. *Engineered Natural Materials*. *Biomaterials Science: An Introduction to Materials: Third Edition* (Elsevier, 2013). doi:10.1016/B978-0-08-087780-8.00022-X.

62. Viljanto, J., Hurme, T., Laippala, P. & Saukko, P. Is cellulose sponge degradable or stable as implantation material ? An in vivo subcutaneous study in the rat. *Biomaterials* **20**, 1989–1995 (1999).

63. Dugan, J. M., Gough, J. E. & Eichhorn, S. J. Bacterial cellulose scaffolds and cellulose nanowhiskers for tissue engineering James M Dugan, Julie E Gough and Stephen J Eichhorn. *Nanomedicine* **2**, 1–15 (2013).

64. Zhou, X. *et al.* Polycaprolactone electrospun fiber scaffold loaded with iPSCs-NSCs and ASCs as a novel tissue engineering scaffold for the treatment of spinal cord injury. *Int. J. Nanomedicine* **13**, 6265 (2018).

65. Yokota, S., Kitaoka, T. & Wariishi, H. Biofunctionality of self-assembled nanolayers composed of cellulosic polymers. *Carbohydr. Polym.* **74**, 666–672 (2008).

66. Pértile, R., Moreira, S., Andrade, F., Domingues, L. & Gama, M. Bacterial cellulose modified using recombinant proteins to improve neuronal and mesenchymal cell adhesion. *Biotechnol. Prog.* **28**, 526–532 (2012).

67. Klemm, D., Schumann, D., Udhardt, U. & Marsch, S. Bacterial synthesized cellulose artificial blood vessels for microsurgery. *Prog. Polym. Sci.* **26**, 1561–1603 (2001).

68. Hickey, R. J. & Pelling, A. E. Cellulose biomaterials for tissue engineering. *Front. Bioeng. Biotechnol.* **7**, 1–15 (2019).

69. Jarvis, M. C. Structure of native cellulose microfibrils, the starting point for nanocellulose

manufacture. *Philos. Trans. R. Soc. A Math. Phys. Eng. Sci.* **376**, (2017).

70. Brown, M., Saxena, I. & Kudlicka, K. Cellulose biosynthesis in higher plants. *Trends Plant Sci.* **1**, (1996).

71. Biomateriais, D. & Engenharia, F. De. Cellulose phosphates as biomaterials . Mineralization of chemically modified regenerated cellulose hydrogels. **6**, 2163–2172 (2001).

72. Bäckdahl, H. *et al.* Mechanical properties of bacterial cellulose and interactions with smooth muscle cells. *Biomaterials* **27**, 2141–9 (2006).

73. Modulevsky, D. J., Cuerrier, C. M. & Pelling, A. E. Biocompatibility of Subcutaneously Implanted Plant-Derived Cellulose Biomaterials. *PLoS One* **11**, 1–19 (2016).

74. Klemm, D., Heublein, B., Fink, H. P. & Bohn, A. Cellulose: fascinating biopolymer and sustainable raw material. *Angew. Chem. Int. Ed. Engl.* **44**, 3358–93 (2005).

75. *Cellulose Market Size, Share&Industry Analysis, By Derivative Type (Commodity Cellulose Pulp, Fibers, ether, esters, microcrystaline, nanocellulose). Fortune Business Insights* https://www.fortunebusinessinsights.com/cellulose-market-102062 (2020).

76. Ng, H. M. *et al.* Extraction of cellulose nanocrystals from plant sources for application as reinforcing agent in polymers. *Compos. Part B Eng.* **75**, 176–200 (2015).

77. Terry, R. A., Tilley, J. M. A. & Outen, G. E. Effect of pH on Cellulose Digestion Under In Vitro Conditions. *J. Sci. Food Agric.* **20**, (1969).

78. Gardner, K. H. & Blackwell, J. The structure of native cellulose. *Biopolymers* **13**, 1975–2001 (1974).

79. Matthews, J. F., Himmel, M. E. & Crowley, M. F. Conversion of cellulose Iα to Iβ via a high temperature intermediate (I-HT) and other cellulose phase transformations. *Cellulose* **19**, 297–306 (2012).

80. Rosso, F., Giordano, A., Barbarisi, M. & Barbarisi, A. From Cell – ECM Interactions to Tissue Engineering. *J. Cell. Physiol.* **180**, 174–180 (2004).

81. Wozniak, M. A., Modzelewska, K., Kwong, L. & Keely, P. J. Focal adhesion regulation of cell behavior. *Biochim. Biophys. Acta - Mol. Cell Res.* **1692**, 103–119 (2004).

82. Yue, B. Biology of the extracellular matrix: an overview. *J. Glaucoma* **23**, S20-3 (2014).

83. Levy, I. & Shoseyov, O. Cellulose-binding domains: Biotechnological applications. *Biotechnol. Adv.* **20**, 191–213 (2002).

84. Martino, F., Perestrelo, A. R., Vinarský, V., Pagliari, S. & Forte, G. Cellular mechanotransduction: From tension to function. *Front. Physiol.* **9**, 1–21 (2018).

85. Oria, R. *et al.* Force loading explains spatial sensing of ligands by cells. *Nature* **552**, 219–224 (2017).

86. Strohmeyer, N., Bharadwaj, M., Costell, M., Fässler, R. & Müller, D. J. Fibronectin-bound α5β1 integrins sense load and signal to reinforce adhesion in less than a second. *Nat. Mater.* **16**, 1262–1270 (2017).

87. Geiger, B., Bershadsky, A., Pankov, R. & Yamada, K. M. Transmembrane crosstalk between the extracellular matrix and the cytoskeleton. *Nat. Rev. Mol. Cell Biol.* **2**, 793–805 (2001).

88. Evans, N. D. *et al.* Substrate stiffness affects early differentiation events in embryonic stem cells. *Eur. Cell. Mater.* **18**, 1–13; discussion 13-4 (2009).

89. Michael, K. E., Dumbauld, D. W., Burns, K. L., Hanks, S. K. & García, A. J. Focal Adhesion Kinase Modulates Cell Adhesion Strengthening via Integrin Activation. *Mol. Biol. Cell* **20**, 2508–2519 (2009).

90. Schiller, H. B. & Fässler, R. Mechanosensitivity and compositional dynamics of cell-matrix adhesions. *EMBO Rep.* **14**, 509–19 (2013).

91. B, A., A, J. & Lewis J. *Molecular Biology of the Cell*. (Garland Science, 2002).

92. Modulevsky, D. J., Lefebvre, C., Haase, K., Al-Rekabi, Z. & Pelling, A. E. Apple Derived Cellulose Scaffolds for 3D Mammalian Cell Culture. *PLoS One* **9**, e97835 (2014).

93. Canadian Institute for Health Information. Annual Statistics on Organ Replacement in Canada: Dialysis, Transplantation and Donation, 2009 to 2018. 1–9 (2018).

94. Scarritt, M. E., Pashos, N. C. & Bunnell, B. A. A review of cellularization strategies for tissue engineering of whole organs. *Front. Bioeng. Biotechnol.* **3**, 1–17 (2015).

95. Williams, D. F. & Williams, D. F. Challenges With the Development of Biomaterials for Sustainable Tissue Engineering. **7**, 1–10 (2019).

96. Hickey, R. J., Modulevsky, D. J., Cuerrier, C. M. & Pelling, A. E. Customizing the Shape and Microenvironment Biochemistry of Biocompatible Macroscopic Plant-Derived Cellulose Scaffolds. *ACS Biomater. Sci. Eng.* **4**, 3726–3736 (2018).

97. Tsai, E. C., Dalton, P. D., Shoichet, M. S. & Tator, C. H. Matrix inclusion within synthetic hydrogel guidance channels improves specific supraspinal and local axonal regeneration after complete spinal cord transection. *Biomaterials* **27**, 519–533 (2006).

98. Yang, Y. *et al.* Neurotrophin releasing single and multiple lumen nerve conduits. *J. Control. Release* **104**, 433–446 (2005).

99. Xiong, Y. *et al.* Coseeded Schwann cells myelinate neurites from differentiated neural stem cells in neurotrophin-3-loaded PLGA carriers. *Int. J. Nanomedicine* **7**, 1977–1989 (2012).

100. Teng, Y. D. *et al.* Functional recovery following traumatic spinal cord injury mediated by a unique polymer scaffold seeded with neural stem cells. *Proc. Natl. Acad. Sci. U. S. A.* **99**, 3024–3029 (2002).

101. Wen, Y. *et al.* Spinal cord injury repair by implantation of structured hyaluronic acid scaffold with PLGA microspheres in the rat. *Cell Tissue Res.* **364**, 17–28 (2016).

102. Wong, D. Y. *et al.* Macro-architectures in spinal cord scaffold implants influence regeneration. *J. Neurotrauma* **25**, 1027–1037 (2008).

103. Patist, C. M. *et al.* Freeze-dried poly(D,L-lactic acid) macroporous guidance scaffolds impregnated with brain-derived neurotrophic factor in the transected adult rat thoracic spinal cord. *Biomaterials* **25**, 1569–1582 (2004).

104. Kim, H., Tator, C. H. & Shoichet, M. S. Chitosan implants in the rat spinal cord: Biocompatibility and biodegradation. *J. Biomed. Mater. Res. - Part A* **97 A**, 395–404 (2011).

105. VandeVord, P. J. *et al.* Evaluation of the biocompatibility of a chitosan scaffold in mice. *J. Biomed. Mater. Res.* **59**, 585–90 (2002).

106. Zhang, Q. *et al.* Polymer scaffolds facilitate spinal cord injury repair. *Acta Biomater.* **88**, 57–77 (2019).

107. Grahn, P. J. *et al.* Implantation of cauda equina nerve roots through a biodegradable scaffold at the conus medullaris in rat. *Spine J.* **14**, 2172–2177 (2014).

108. Krych, A. J. *et al.* Relationship between scaffold channel diameter and number of regenerating axons in the transected rat spinal cord. *Acta Biomater.* **5**, 2551–2559 (2009).

109. Shrestha, B. *et al.* Repair of injured spinal cord using biomaterial scaffolds and stem cells. *Stem Cell Res. Ther.* **5**, 1–11 (2014).

110. Norenberg, M. D., Smith, J. O. N. & Marcillo, A. The Pathology of Human Spinal Cord Injury : Defining the Problems. *J. Neurotrauma* **21**, 429–440 (2004).

111. Huang, H. J., Tsai, Y. L., Lin, S. H. & Hsu, S. H. Smart polymers for cell therapy and precision medicine. *J. Biomed. Sci.* **26**, 1–11 (2019).

112. Li, X., Yang, Z., Zhang, A., Wang, T. & Chen, W. Repair of thoracic spinal cord injury by chitosan tube implantation in adult rats. *Biomaterials* **30**, 1121–1132 (2009).

113. Houle, J. D. *et al.* Combining an Autologous Peripheral Nervous System 'Bridge' and Matrix Modification by Chondroitinase Allows Robust, Functional Regeneration beyond a Hemisection Lesion of the Adult Rat Spinal Cord. *J. Neurosci.* **26**, 7405–7415 (2006).

114. Chen, X. *et al.* Functional Multichannel Poly(Propylene Fumarate)-Collagen Scaffold with Collagen-Binding Neurotrophic Factor 3 Promotes Neural Regeneration After Transected Spinal Cord Injury. *Adv. Healthc. Mater.* **7**, 1800315 (2018).

115. Bradbury, E. J. *et al.* Chondroitinase ABC promotes functional recovery after spinal cord injury. *Nature* **416**, 636–640 (2002).

116. Haggerty, A. E. & Oudega, M. Biomaterials for spinal cord repair. *Neurosci. Bull.* **29**, 445–459 (2013).

117. Khaing, Z. Z. *et al.* High molecular weight hyaluronic acid limits astrocyte activation and scar formation after spinal cord injury. *J. Neural Eng.* **8**, (2011).

118. Xudong, C. & Shoichet, M. S. Delivering neuroactive molecules from biodegradable microspheres for application in central nervous system disorders. *Biomaterials* **20**, 329–339 (1999).

119. Guy, A. *et al.* Glycerophospholipid regulation of modality-specific sensory axon guidance in the spinal cord. *Neuronal Dev.* **349**, (2015).

120. Zarei-Kheirabadi, M. *et al.* Human embryonic stem cell-derived neural stem cells encapsulated in hyaluronic acid promotes regeneration in a contusion spinal cord injured rat. *Int. J. Biol. Macromol.* **148**, 1118–1129 (2020).

121. Tsai, E. C. & Tator, C. H. Neuroprotection and regeneration strategies for spinal cord repair. *Curr. Pharm. Des.* **11**, 1211–22 (2005).

122. Gupta, D., Tator, C. H. & Shoichet, M. S. Fast-gelling injectable blend of hyaluronan and methylcellulose for intrathecal, localized delivery to the injured spinal cord. *Biomaterials* **27**, 2370–2379 (2006).

123. Rosner, J., Avalos, P., Acosta, F., Liu, J. & Drazin, D. The Potential for Cellular Therapy Combined with Growth Factors in Spinal Cord Injury. *Stem Cells Int.* **2012**, 1–11 (2012).

124. Li, X. *et al.* A collagen microchannel scaffold carrying paclitaxel-liposomes induces neuronal differentiation of neural stem cells through Wnt/β-catenin signaling for spinal cord injury repair. *Biomaterials* **183**, 114–127 (2018).

125. Higuchi, A. *et al.* Biomaterials used in stem cell therapy for spinal cord injury. *Prog. Mater. Sci.* **103**, 374–424 (2019).

126. Soares, S., von Boxberg, Y. & Nothias, F. Repair strategies for traumatic spinal cord injury, with special emphasis on novel biomaterial-based approaches. *Rev. Neurol. (Paris).* 1–9 (2020) doi:10.1016/j.neurol.2019.07.029.

127. Ghane, N., Beigi, M., Labbaf, S., Nasr-Esfrahani, M. & Kiani, A. Design of hydrogel-based scaffolds for the treatment of spinal cord injuries. *J. Mater. Chem. B* (2020) doi:10.1001/archsurg.1954.01270040044008.

128. White, R. & Lyn, J. Don't fence me in: Harnessing the beneficial roles of astrocytes for spinal cord repair. *Restor Neurol Neurosci* **26**, 197–214 (2008).

129. Hutson, T. H. & Di Giovanni, S. The translational landscape in spinal cord injury: focus on neuroplasticity and regeneration. *Nat. Rev. Neurol.* **15**, 732–745 (2019).

130. Lowery, L. A. & Van Vactor, D. The trip of the tip: understanding the growth cone machinery. *Nat. Rev. Mol. Cell Biol.* **10**, 332–43 (2009).

131. What types of forces do cells encounter? https://www.mechanobio.info/what-is-mechanobiology/what-types-of-forces-do-cells-encounter/.

132. Dharani, K. Physiology of the Neuron. in *The Biology of Thought* 31–52 (2015). doi:10.1016/b978-0-12-800900-0.00002-6.

133. Burnette, D. T. *et al.* Myosin II Activity Facilitates Microtubule Bundling in the Neuronal Growth Cone Neck. *Dev. Cell* **15**, 163–169 (2008).

134. Sydor, A. M., Su, A. L., Wang, F. S., Xu, A. & Jay, D. G. Talin and vinculin play distinct roles in filopodial motility in the neuronal growth cone. *J. Cell Biol.* **134**, 1197–1207 (1996).

135. Tosney, K. W. & Landmesser, L. T. Growth cone morphology and trajectory in the lumbosacral region of the chick embryo. *J. Neurosci.* **5**, 2345–58 (1985).

136. Debanne, D., Campanac, E., Bialowas, A., Carlier, E. & Alcaraz, G. Axon Physiology. *Physiol. Rev.* **91**, 555–602 (2019).

137. Ikeda, M. & Oka, Y. The relationship between nerve conduction velocity and fiber morphology during peripheral nerve regeneration. *Brain Behav.* **2**, 382–390 (2012).

138. Westrum, L. E. & Blackstad, T. W. An electron microscopic study of the stratum radiatum of the rat hippocampus (regio superior, CA 1) with particular emphasis on synaptology. *J. Comp. Neurol.* **119**, 281–309 (1962).

139. Nguyen, A. T., Sathe, S. R. & Yim, E. K. F. F. From nano to micro: Topographical scale and its impact on cell adhesion, morphology and contact guidance. *J. Phys. Condens. Matter* **28**, 183001 (2016).

140. Kerstein, P. C., Nichol, R. H., Gomez, T. M. & Gomez, T. M. Mechanochemical regulation of growth cone motility. *Front. Cell. Neurosci.* **9**, 244 (2015).

141. Sawada, Y. *et al.* Force Sensing by Mechanical Extension of the Src Family Kinase Substrate

p130Cas. *Cell* **127**, 1015–1026 (2006).

142. Moore, S. W., Zhang, X., Lynch, C. D. & Sheetz, M. P. Netrin-1 Attracts Axons through FAK-Dependent Mechanotransduction. *J. Neurosci.* **32**, 11574–11585 (2012).

143. Sperry, R. W. *et al.* CHEMOAFFINITY IN THE ORDERLY GROWTH OF NERVE FIBER PATTERNS AND CONNECTIONS. *Proc. Natl. Acad. Sci.* **50**, 703–710 (1963).

144. Nugent, A. A., Kolpak, A. L. & Engle, E. C. Human disorders of axon guidance. *Curr. Opin. Neurobiol.* **22**, 837–843 (2012).

145. Stoeckli, E. T. Understanding axon guidance: Are we nearly there yet? *Development* **145**, 1–10 (2018).

146. de Ramon Francàs, G., Zuñiga, N. R. & Stoeckli, E. T. The spinal cord shows the way – How axons navigate intermediate targets. *Dev. Biol.* **432**, 43–52 (2017).

147. Blockus, H. & Chédotal, A. Slit-robo signaling. *Dev.* **143**, 3037–3044 (2016).

148. Parra, L. M. & Zou, Y. Sonic hedgehog induces response of commissural axons to Semaphorin repulsion during midline crossing. *Nat. Neurosci.* **13**, 29–35 (2010).

149. Kerstein, P. C., Nichol IV, R. H. & Gomez, T. M. Mechanochemical regulation of growth cone motility. *Front. Cell. Neurosci.* **9**, 244 (2015).

150. Kostic, A., Sap, J., Sheetz, M. P., Wood, M. R. & Pfenninger, K. H. RPTPalpha is required for rigidity-dependent inhibition of extension and differentiation of hippocampal neurons. *J. Cell Sci.* **120**, 3895–904 (2007).

151. Bunge, R., Pickett, W. R., Becerra, L., Marcillo, A. & Quencer, R. M. Observations on the pathology of human spinal cord injury. A review and classification of 22 new cases with details from a case of chronic cord compression with extensive focal demyelination. *Adv. Neurol.* **59**, 75–89 (1993).

152. Crowe, M. J., Bresnahan, J. C., Shuman, S. L., Masters, J. N. & Beattie, M. S. Apoptosis and delayed degeneration after spinal cord injury in rats and monkeys. *Nat Med* **3**, 73–76 (1997).

153. MCDONALD, W. I. & SEARS, T. A. The effects of experimental demyelination on conduction in the central nervous system. *Brain* **93**, 583–598 (1970).

154. Buss, A. *et al.* Sequential loss of myelin proteins during Wallerian degeneration in the human spinal cord. *Brain* **128**, 356–364 (2005).

155. Adams, K. L. & Gallo, V. The diversity and disparity of the glial scar. *Nat. Neurosci.* **21**, 9–15 (2018).

156. Sofroniew, M. V. Molecular dissection of reactive astrogliosis and glial scar formation. *Trends Neurosci.* **32**, 638–47 (2009).

157. Anderson, M. A., Ao, Y. & Sofroniew, M. V. Heterogeneity of reactive astrocytes. *Neurosci. Lett.* **565**, 23–29 (2014).

158. Cregg, J. M. *et al.* Functional regeneration beyond the glial scar. *Exp. Neurol.* **253**, 197–207 (2014).

159. Yamada, K. M. & Cukierman, E. Modeling tissue morphogenesis and cancer in 3D. *Cell* **130**, 601–10 (2007).

160. Derda, R. *et al.* Paper-supported 3D cell culture for tissue-based bioassays. *PNAS* **106**, 18457–62 (2009).

161. Puschmann, T. B. *et al.* Bioactive 3D cell culture system minimizes cellular stress and maintains the in vivo-like morphological complexity of astroglial cells. *Glia* **61**, 432–40 (2013).

162. Fennema, E., Rivron, N., Rouwkema, J., VanBlitterswijk, C. & DeBoer, J. Spheroid culture as a tool for creating 3D complex tissues. *Trends Biotechnol.* **31**, 108–15 (2013).

163. Griffith, L. G. & Swartz, M. A. Capturing complex 3D tissue physiology in vitro. *Nat. Rev. Mol. Cell Biol.* **7**, 211–24 (2006).

164. Baker, B. M. & Chen, C. S. Deconstructing the third dimension: how 3D culture microenvironments alter cellular cues. *J. Cell Sci.* **125**, 3015–24 (2012).

165. Petersen, O. W., Rønnov-Jessen, L., Howlett, A. R. & Bissell, M. J. Interaction with basement membrane serves to rapidly distinguish growth and differentiation pattern of normal and malignant human breast epithelial cells. *Proc. Natl. Acad. Sci. U. S. A.* **89**, 9064–8 (1992).

166. VonDerMark, K., Gauss, V., VonDerMark, H. & Muller, P. Releationship Between cell shape and type of collagen synthesised as chrondrocytes lose their cartilage phenotype in culture. *Nature* **267**, 531–532 (1977).

167. Benya, P. D. & Shaffer, J. D. Dedifferentiated chondrocytes reexpress the differentiated collagen phenotype when cultured in agarose gels. *Cell* **30**, 215–24 (1982).

168. Owen, S. C. & Shoichet, M. S. Design of three-dimensional biomimetic scaffolds. *J. Biomed. Mater. Res. A* **94**, 1321–31 (2010).

169. Svensson, a *et al.* Bacterial cellulose as a potential scaffold for tissue engineering of cartilage. *Biomaterials* **26**, 419–31 (2005).

170. Czaja, W. K., Young, D. J., Kawecki, M. & Brown, R. M. The future prospects of microbial cellulose in biomedical applications. *Biomacromolecules* **8**, 1–12 (2007).

171. Andrade, F. K. *et al.* Studies on the hemocompatibility of bacterial cellulose. *J. Biomed. Mater. Res.* **98**, 554–66 (2011).

172. Hirayama, K. *et al.* Cellular building unit integrated with microstrand-shaped bacterial cellulose. *Biomaterials* **34**, 2421–7 (2013).

173. Schumann, D. A. *et al.* Artificial vascular implants from bacterial cellulose: preliminary results of small arterial substitutes. *Cellulose* **16**, 877–885 (2008).

174. Derda, R. *et al.* Multizone paper platform for 3D cell cultures. *PLoS One* **6**, e18940 (2011).

175. Ishihara, K., Miyazaki, H., Kurosaki, T. & Nakabayashi, N. Improvement of blood compatibility on cellulose dialysis membrane. 111. Synthesis and performance of water-soluble cellulose grafted with phospholipid polymer as coating material on cellulose dialysis membrane. *J. Biomed. Mater. Res.* **29**, 181–188 (1995).

176. Watanabe, K. *et al.* A new bacterial cellulose substrate for mammalian cell culture. *Cytotechnology* **13**, 107–114 (1993).

177. Pértile, R. A. N., Moreira, S., Gil, R. M., Correia, A. & Guãrdao, L. Bacterial Cellulose : Long-Term Biocompatibility Studies. *J. Biomater. Sci. Polym. Ed.* **23**, 1339–1354 (2012).

178. Entcheva, E. *et al.* Functional cardiac cell constructs on cellulose-based scaffolding. *Biomaterials* **25**, 5753–62 (2004).

179. Bancroft, G. N., Sikavitsas, V. I. & Mikos, A. G. Design of a Flow Perfusion Bioreactor System for Bone Tissue-Engineering Applications. *Tissue Eng.* **9**, (2003).

180. Bourgine, P. E., Pippenger, B. E., Todorov, A., Tchang, L. & Martin, I. Tissue decellularization by activation of programmed cell death. *Biomaterials* **34**, 6099–6108 (2013).

181. Gratzer, P. F., Harrison, R. D. & Woods, T. Matrix alteration and not residual sodium dodecyl sulfate cytotoxicity affects the cellular repopulation of a decellularized matrix. *Tissue Eng.* **12**, 2975–83 (2006).

182. Gillies, A. R., Smith, L. R., Leiber, R. L. & Varghese, S. Method for Decellularizing Skeletal Muscle Without Detergents or Proteolytic Enzymes. *Tissue Eng. Part C. Methods* **17**, 383–389 (2011).

183. Orlando, G. *et al.* Regenerative medicine and organ transplantation: past, present, and future. *Transplantation* **91**, 1310–7 (2011).

184. Arenas-Herrera, J. E., Ko, I. K., Atala, A. & Yoo, J. J. Decellularization for whole organ bioengineering. *Biomed. Mater.* **8**, 014106 (2013).

185. Gilbert, T. W., Sellaro, T. L. & Badylak, S. F. Decellularization of tissues and organs. *Biomaterials* **27**, 3675–83 (2006).

186. Rieder, E. *et al.* Decellularization protocols of porcine heart valves differ importantly in efficiency of cell removal and susceptibility of the matrix to recellularization with human vascular cells. *J. Thorac. Cardiovasc. Surg.* **127**, 399–405 (2004).

187. Kasimir, M. T. *et al.* Comparison of different decellularization procedures of porcine heart valves. *Int. J. Artif. Organs* **26**, 421–7 (2003).

188. Song, J. J. & Ott, H. C. Organ engineering based on decellularized matrix scaffolds. *Trends Mol. Med.* **17**, 424–32 (2011).

189. Schaner, P. J. *et al.* Decellularized vein as a potential scaffold for vascular tissue engineering. *J. Vasc. Surg.* **40**, 146–53 (2004).

190. Nakayama, K. H., Batchelder, C. A., Lee, C. I. & Tarantal, A. F. Decellularized Rhesus Monkey Kidney as a Three-Dimensional Scaffold for Renal Tissue Engineering. *Tissue Eng. Part A* **16**, (2010).

191. Ross, E. *et al.* Embryonic stem cells proliferate and differentiate when seeded into kidney scaffolds. *J. Am. Soc. Nephrol.* **20**, 2338–47 (2009).

192. Atala, A., Bauer, S. B., Soker, S., Yoo, J. J. & Retik, A. B. Tissue-engineered autologous bladders for patients needing cystoplasty. *Lancet* **367**, 1241–6 (2006).

193. Ott, H. C. *et al.* Regeneration and orthotopic transplantation of a bioartificial lung. *Nat. Med.* **16**, 927–33 (2010).

194. Guolla, L., Bertrand, M., Haase, K. & Pelling, A. E. Force transduction and strain dynamics in actin stress fibres in response to nanonewton forces. *J. Cell Sci.* **125**, 603–13 (2012).

195. Modulevsky, D. J., Tremblay, D., Gullekson, C., Bukoresthliev, N. V & Pelling, A. E. The Physical Interaction of Myoblasts with the Microenvironment during Remodeling of the

Cytoarchitecture. *PLoS One* **7**, e45329 (2012).

196. Truernit, E. *et al.* High-resolution whole-mount imaging of three-dimensional tissue organization and gene expression enables the study of Phloem development and structure in Arabidopsis. *Plant Cell* **20**, 1494–503 (2008).

197. Hutter, J. L. & Bechhoefer, J. Calibration of atomic-force microscope tips. *Rev. Sci. Instrum.* **64**, 1868 (1993).

198. Levy, R., Maaloum, M., Sadron-universit, I. C., Levy, R. & Maaloum, M. Measuring the spring constant of atomic force microscope cantilevers : thermal fluctuations and other methods. *Nanotechnology* **33**, 0–5 (2002).

199. Carl, P., Kwok, C. H., Manderson, G., Speicher, D. W. & Discher, D. E. Forced unfolding modulated by disulfide bonds in the Ig domains of a cell adhesion molecule. *PNAS* **98**, 1565–70 (2001).

200. Hulbary, R. L. The Influence of Air Spaces on the Three-Dimensional Shapes of Cells in Elodea Stems, and a Comparison with Pith Cells of Ailanthus. *Am. J. Bot.* **31**, 561–580 (1944).

201. Esau, K. *Plant Anantomy*. (Wiley, 1965).

202. Manduca, A. *et al.* Magnetic resonance elastography : Non-invasive mapping of tissue elasticity. *Med. Image Anal.* **5**, 237–254 (2001).

203. Levental, I., Georges, P. C. & Janmey, P. Soft biological materials and their impact on cell function. *Soft Matter* **3**, 299 (2007).

204. Rai, R., Keshavarz, T., Roether, J., Boccaccini, A. & Roy, I. Medium chain length polyhydroxyalkanoates, promising new biomedical materials for the future. *Mater. Sci. Eng.* **72**, 29–47 (2011).

205. Fong, E. L. S. *et al.* Modeling Ewing sarcoma tumors in vitro with 3D scaffolds. *PNAS* **110**, 6500–5 (2013).

206. Pelling, A. E., Veraitch, F. S., Chu, C. P. K., Mason, C. & Horton, M. Mechanical dynamics of single cells during early apoptosis. *Cell Motil. Cytoskeleton* **66**, 409–22 (2009).

207. Tee, S. Y., Fu, J., Chen, C. & Janmey, P. Cell shape and substrate rigidity both regulate cell stiffness. *Biophys. J.* **100**, L25-7 (2011).

208. Versaevel, M., Grevesse, T. & Gabriele, S. Spatial coordination between cell and nuclear shape within micropatterned endothelial cells. *Nat. Commun.* **3**, 671 (2012).

209. Freed, L. E. *et al.* Joint resurfacing using allograft chondrocytes and synthetic biodegradable polymer scaffolds. *J. Biomed. Mater. Res.* **28**, 891–9 (1994).

210. Tibbitt, M. W. & Anseth, K. S. Hydrogels as extracellular matrix mimics for 3D cell culture. *Biotechnol. Bioeng.* **103**, 655–63 (2009).

211. Lutolf, M. P. & Hubbell, J. A. Synthetic biomaterials as instructive extracellular microenvironments for morphogenesis in tissue engineering. *Nat. Biotechnol.* **23**, 47–55 (2005).

212. Atala, A. *et al.* Formation of urothelial structures in vivo from dissociated cells attached to biodegradable polymer scaffolds in vitro. *J. Urol.* **148**, 658–62 (1992).

213. Freed, L. E. *et al.* Neocartilage formation in vitro and in vivo using cells cultured on synthetic

biodegradable polymers. *J. Biomed. Mater. Res.* **27**, 11–23 (1993).

214. Schaffner, J. H. A General System of Floral Diagrams. *Ohio J. Sci.* **16**, 360–366 (1916).

215. Brett, C. & Hillman, J. *Biochemistry of Plant Cell Walls*. (Cambridge University Press, 1985).

216. Hansen, P. *et al.* Glutaraldehyde cross-linking of tendon--mechanical effects at the level of the tendon fascicle and fibril. *Connect. Tissue Res.* **50**, 211–22 (2009).

217. Hutter, J. L. *et al.* Atomic force microscopy investigation of the dependence of cellular elastic moduli on glutaraldehyde fixation. *J. Microsc.* **219**, 61–8 (2005).

218. Ou, K. L. *et al.* Effect of collagen on the mechanical properties of hydroxyapatite coatings. *J. Mech. Behav. Biomed. Mater.* **4**, 618–24 (2011).

219. Grotte, M., Duprat, F., Piétri, E. & Loonis, D. Young'S Modulus, Poisson's Ratio, and Lame'S Coefficients of Golden Delicious Apple. *Int. J. Food Prop.* **5**, 333–349 (2002).

220. Masoudi, H., Tabatabaeefar, A. & Borghaee, A. M. Determination of storage effect on mechanical properties of apples using the uniaxial compression test. *Can. Biosyst. Eng.* **49**, 29–33 (2007).

221. Kozlova, L., Petrova, A., Ananchenko, B. & Gorshkova, T. Assessment of Primary Cell Wall Nanomechanical. *Plants* **8**, (2019).

222. Calderwood, D., Shattil, S. & Ginsberg, M. Integrins and actin filaments: reciprocal regulation of cell adhesion and signaling. *J. Biol. Chem.* **275**, 22607–10 (2000).

223. Haase, K. & Pelling, A. E. Resiliency of the plasma membrane and actin cortex to large-scale deformation. *Cytoskeleton* 494–515 (2013) doi:: 10.1002/cm.21129.

224. Chang, H. & Wang, Y. Cell Responses to Surface and Architecture of Tissue Engineering Scaffolds. in *Regenerative Medicine and Tissue Engineering- Cells and Biomaterials* (ed. Eberli, D.) (2011).

225. McBane, J. E., Ebadi, D., Sharifpoor, S., Labow, R. S. & Santerre, J. P. Differentiation of monocytes on a degradable, polar, hydrophobic, ionic polyurethane: Two-dimensional films vs. three-dimensional scaffolds. *Acta Biomater.* **7**, 115–22 (2011).

226. Todaro, G. & Green, H. Quantitative Studies of the growth of Moyse Enbryo cells in culture and their development into estalblished lines. *J. Cell Biol.* **17**, 299–313 (1963).

227. Nilsen, T. W. Preparation of Nuclear Extracts from HeLa cells. *Cold Spring Harb. Protoc.* **2013**, 579–83 (2013).

228. Milotti, E. & Chignola, R. Emergent properties of tumor microenvironment in a real-life model of multicell tumor spheroids. *PLoS One* **5**, e13942 (2010).

229. Uygun, B. E. *et al.* Organ reengineering through development of a transplantable recellularized liver graft using decellularized liver matrix. *Nat. Med.* **16**, 814–820 (2010).

230. Pashuck, E. T. & Stevens, M. M. STATE OF THE ART REVIEW Designing Regenerative Biomaterial Therapies for the Clinic. *Sci. Transl. Med.* **4**, (2012).

231. Athanasiou, K. A. *et al.* Special section. **338**, 921–927 (2012).

232. Gu, L. & Mooney, D. J. Biomaterials and emerging anticancer therapeutics: engineering the microenvironment. *Nat. Rev. Cancer* **16**, 56–66 (2015).

233. Maurer, M., Röhrnbauer, B., Feola, A., Deprest, J. & Mazza, E. Prosthetic Meshes for Repair of Hernia and Pelvic Organ Prolapse: Comparison of Biomechanical Properties. *Materials (Basel).* **8**, 2794–2808 (2015).

234. Mao, A. S. & Mooney, D. J. Regenerative medicine: Current therapies and future directions. *Proc. Natl. Acad. Sci.* **112**, 201508520 (2015).

235. Hsu, S.-H. & Hsieh, P.-S. Self-assembled adult adipose-derived stem cell spheroids combined with biomaterials promote wound healing in a rat skin repair model. *Wound Repair Regen.* **23**, 57–64.

236. Guillaume, O. *et al.* Fabrication of silk mesh with enhanced cytocompatibility: preliminary in vitro investigation toward cell-based therapy for hernia repair. *J. Mater. Sci. Mater. Med.* **27**, 37 (2016).

237. Soto-Gutierrez, A. *et al.* A whole-organ regenerative medicine approach for liver replacement. *Tissue Eng. Part C,* **17**, 677–686 (2011).

238. Badylak, S. F., Taylor, D. & Uygun, K. Whole-Organ Tissue Engineering: Decellularization and Recellularization of Three-Dimensional Matrix Scaffolds. (2011).

239. Baptista, P. M. *et al.* Whole organ decellularization - a tool for bioscaffold fabrication and organ bioengineering. *Conf. Proc. ... Annu. Int. Conf. IEEE Eng. Med. Biol. Soc. IEEE Eng. Med. Biol. Soc. Annu. Conf.* **2009**, 6526–9 (2009).

240. Baptista, P. M. *et al.* The use of whole organ decellularization for the generation of a vascularized liver organoid. *Hepatology* **53**, 604–617 (2011).

241. Badylak, S. F. The extracellular matrix as a biologic scaffold material. *Biomaterials* **28**, 3587–3593 (2007).

242. Lv, S. *et al.* Designed biomaterials to mimic the mechanical properties of muscles. *Nature* **465**, 69–73 (2010).

243. Campoli, G. *et al.* Mechanical properties of open-cell metallic biomaterials manufactured using additive manufacturing. *Mater. Des.* **49**, 957–965 (2013).

244. Anseth, K. S., Bowman, C. N. & Brannon-Peppas, L. Mechanical properties of hydrogels and their experimental determination. *Biomaterials* **17**, 1647–1657 (1996).

245. Zhao, R., Sider, K. L. & Simmons, C. a. Measurement of layer-specific mechanical properties in multilayered biomaterials by micropipette aspiration. *Acta Biomater.* **7**, 1220–1227 (2011).

246. Chen, Q., Liang, S. & Thouas, G. a. Elastomeric biomaterials for tissue engineering. *Prog. Polym. Sci.* **38**, 584–671 (2013).

247. Guzman, R. C. de *et al.* Mechanical and biological properties of keratose biomaterials. *Biomaterials* **32**, 8205–17 (2011).

248. Staiger, M. P., Pietak, A. M., Huadmai, J. & Dias, G. Magnesium and its alloys as orthopedic biomaterials: A review. *Biomaterials* **27**, 1728–1734 (2006).

249. Bagno, A. & Di Bello, C. Surface treatments and roughness properties of Ti-based biomaterials. *J. Mater. Sci. Mater. Med.* **15**, 935–49 (2004).

250. Tibbitt, M. W. & Anseth, K. S. Dynamic Microenvironments : The Fourth Dimension. **4**, 1–5 (2012).

251. Lemons, J. E. & Lucas, L. C. Properties of biomaterials. *J. Arthroplasty* **1**, 143–147 (1986).

252. Why Organ, Eye and Tissue Donation? *U.S. Department of Health and Human Services* http://www.organdonor.gov/index.html.

253. Sterling, J. A. & Guelcher, S. A. Biomaterial scaffolds for treating osteoporotic bone. *Curr. Osteoporos. Rep.* **12**, 48–54 (2014).

254. Abou Neel, E. A., Chrzanowski, W., Salih, V. M., Kim, H.-W. & Knowles, J. C. Tissue engineering in dentistry. *J. Dent.* **42**, 915–28 (2014).

255. Shue, L., Yufeng, Z. & Mony, U. Biomaterials for periodontal regeneration A review of ceramics and polymers. *Biomatter* **2**, 271–7 (2012).

256. O'Brien, F. J. Biomaterials & scaffolds for tissue engineering. *Mater. Today* **14**, 88–95 (2011).

257. Bhardwaj, N., Devi, D. & Mandal, B. B. Tissue-engineered cartilage: the crossroads of biomaterials, cells and stimulating factors. *Macromol. Biosci.* **15**, 153–82 (2015).

258. Metcalfe, A. D. & Ferguson, M. W. J. Tissue engineering of replacement skin: the crossroads of biomaterials, wound healing, embryonic development, stem cells and regeneration. *J. R. Soc. Interface* **4**, 413–37 (2007).

259. Takebe, T. *et al.* Vascularized and functional human liver from an iPSC-derived organ bud transplant. *Nature* **499**, 481–4 (2013).

260. Mannoor, M. S. *et al.* 3D printed bionic ears. *Nano Lett.* **13**, 2634–9 (2013).

261. Raya-Rivera, A. M. *et al.* Tissue-engineered autologous vaginal organs in patients: a pilot cohort study. *Lancet (London, England)* **384**, 329–36 (2014).

262. Salzberg, C. A. Nonexpansive immediate breast reconstruction using human acellular tissue matrix graft (AlloDerm). *Ann. Plast. Surg.* **57**, 1–5 (2006).

263. Lee, D. K. Achilles Tendon Repair with Acellular Tissue Graft Augmentation in Neglected Ruptures. *J. Foot Ankle Surg.* **46**, 451–455 (2007).

264. Cornwell, K. G., Landsman, A. & James, K. S. Extracellular Matrix Biomaterials for Soft Tissue Repair. *Clin. Podiatr. Med. Surg.* **26**, 507–523 (2009).

265. Ren, X. *et al.* Engineering pulmonary vasculature in decellularized rat and human lungs. *Nat. Biotechnol.* **33**, 1097–102 (2015).

266. Guyette, J. P. *et al.* Bioengineering Human Myocardium on Native Extracellular Matrix. *Circ. Res.* **118**, 118–56 (2016).

267. Raya-Rivera, A. *et al.* Tissue-engineered autologous urethras for patients who need reconstruction: an observational study. *Lancet (London, England)* **377**, 1175–82 (2011).

268. Hattori, N. Cerebral organoids model human brain development and microcephaly. *Mov. Disord.* **29**, 185–185 (2014).

269. Gottenbos, B., Busscher, H. J., Van Der Mei, H. C. & Nieuwenhuis, P. Pathogenesis and prevention of biomaterial centered infections. *J. Mater. Sci. Mater. Med.* **13**, 717–722 (2002).

270. Bohner, M. Resorbable biomaterials as bone graft substitutes. *Mater. Today* **13**, 24–30 (2010).

271. Bae, H. *et al.* Building Vascular Networks. *Tissue Eng.* **4**, 1–6 (2012).

272. Dong, W. *et al.* A Dual Role of Graphene Oxide Sheet Deposition on Titanate Nanowire Scaffolds for Osteo-implantation: Mechanical Hardener and Surface Activity Regulator. *Sci. Rep.* **5**, 18266 (2015).

273. Zhou, L. *et al.* Engineering ear constructs with a composite scaffold to maintain dimensions. *Tissue Eng. Part A* **17**, 1573–1581 (2011).

274. Temenoff, J. S. & Mikos, A. G. Injectable biodegradable materials for orthopedic tissue engineering. *Biomaterials* **21**, 2405–2412 (2000).

275. Bao, G. & Suresh, S. Cell and molecular mechanics of biological materials. *Nat. Mater.* **2**, 715–25 (2003).

276. Place, E. S., Evans, N. D. & Stevens, M. M. Complexity in biomaterials for tissue engineering. *Nat. Mater.* **8**, 457–470 (2009).

277. Pomerantseva, I. *et al.* Ear-Shaped Stable Auricular Cartilage Engineered from Extensively Expanded Chondrocytes in an Immunocompetent Experimental Animal Model. *Tissue Eng. Part A* **22**, ten.tea.2015.0173 (2015).

278. Xu, J.-W. *et al.* Tissue-engineered flexible ear-shaped cartilage. *Plast. Reconstr. Surg.* **115**, 1633–41 (2005).

279. Shieh, S.-J., Terada, S. & Vacanti, J. P. Tissue engineering auricular reconstruction: in vitro and in vivo studies. *Biomaterials* **25**, 1545–57 (2004).

280. Neumeister, M. W., Wu, T. & Chambers, C. Vascularized tissue-engineered ears. *Plast. Reconstr. Surg.* **117**, 116–22 (2006).

281. Isogai, N. *et al.* Tissue engineering of an auricular cartilage model utilizing cultured chondrocyte-poly(L-lactide-epsilon-caprolactone) scaffolds. *Tissue Eng.* **10**, 673–87.

282. Cervantes, T. M. *et al.* Design of composite scaffolds and three-dimensional shape analysis for tissue-engineered ear. *J. R. Soc. Interface* **10**, 20130413 (2013).

283. Liao, H. T. *et al.* Prefabricated, Ear-Shaped Cartilage Tissue Engineering by Scaffold-Free Porcine Chondrocyte Membrane. *Plast. Reconstr. Surg.* **135**, 313–321 (2015).

284. Lee, J.-S. 3D printing of composite tissue with complex shape applied to ear regeneration. *Biofabrication* **6**, (2014).

285. Helenius, G. *et al.* In vivo biocompatibility of bacterial cellulose. *J. Biomed. Mater. Res. Part A* **76A**, 431–438 (2006).

286. Tischer, P. C. S. F., Sierakowski, M. R., Westfahl, H. & Tischer, C. A. Nanostructural reorganization of bacterial cellulose by ultrasonic treatment. *Biomacromolecules* **11**, 1217–24 (2010).

287. Ishihara K, Nakabayashi N, Fukumoto K, A. J. Improvement of blood compatibility on cellulose dialysis membrane. *Biomaterials* **13**, 145–149 (1992).

288. Gibson, L. J. The hierarchical structure and mechanics of plant materials. *J. R. Soc. Interface* **9**, 2749–2766 (2012).

289. Bhattacharya, M. *et al.* Nanofibrillar cellulose hydrogel promotes three-dimensional liver cell culture. *J. Control. Release* **164**, 291–298 (2012).

290. Brown, E. E., Hu, D., Abu Lail, N. & Zhang, X. Potential of Nanocrystalline Cellulose–Fibrin Nanocomposites for Artificial Vascular Graft Applications. *Biomacromolecules* **14**, 1063–1071 (2013).

291. Dugan, J. M., Collins, R. F., Gough, J. E. & Eichhorn, S. J. Oriented surfaces of adsorbed cellulose nanowhiskers promote skeletal muscle myogenesis. *Acta Biomater.* **9**, 4707–15 (2013).

292. Lin, N. & Dufresne, A. Nanocellulose in biomedicine: Current status and future prospect. *Eur. Polym. J.* **59**, 302–325 (2014).

293. Nimeskern, L. *et al.* Mechanical evaluation of bacterial nanocellulose as an implant material for ear cartilage replacement. *J. Mech. Behav. Biomed. Mater.* **22**, 12–21 (2013).

294. Lu, Y. *et al.* Nanocellulose in polymer composites and biomedical applications. *TAPPI J.* **13**, 47–54 (2014).

295. Trindade, R., Albrektsson, T., Tengvall, P. & Wennerberg, A. Foreign Body Reaction to Biomaterials: On Mechanisms for Buildup and Breakdown of Osseointegration. *Clin. Implant Dent. Relat. Res.* **18**, 1–12 (2014).

296. Onuki, Y., Bhardwaj, U., Papadimitrakopoulos, F. & Burgess, D. J. A review of the biocompatibility of implantable devices: current challenges to overcome foreign body response. *J. diabetes Sci. Technol.* **2**, 1003–1015 (2008).

297. Anderson, J. M., Rodriguez, A. & Chang, D. T. Foreign body reaction to biomaterials. *Semin. Immunol.* **20**, 86–100 (2008).

298. Jones, K. S. Effects of biomaterial-induced inflammation on fibrosis and rejection. *Semin. Immunol.* **20**, 130–136 (2008).

299. Nilsson, B., Ekdahl, K. N., Mollnes, T. E. & Lambris, J. D. The role of complement in biomaterial-induced inflammation. *Mol. Immunol.* **44**, 82–94 (2007).

300. Motegi, K., Nakano, Y. & Namikawa, A. Relation between cleavage lines and scar tissues. *J. Maxillofac. Surg.* **12**, 21–8 (1984).

301. Rickert, D., Moses, M. A., Lendlein, A., Kelch, S. & Franke, R.-P. The importance of angiogenesis in the interaction between polymeric biomaterials and surrounding tissue. *Clin. Hemorheol. Microcirc.* **28**, 175–81 (2003).

302. Beguin, P. The biological degradation of cellulose. *FEMS Microbiol. Rev.* **13**, 25–58 (1994).

303. Miyamoto, T., Takahashi, S., Ito, H., Inagaki, H. & Noishiki, Y. Tissue biocompatibility of cellulose and its derivatives. *J. Biomed. Mater. Res.* **23**, 125–133 (1989).

304. Dugan, J. M., Gough, J. E. & Eichhorn, S. J. Bacterial Cellulose Scaffolds and Cellulose Nanowhiskers for Tissue Engineering. *Nanomedicine* **8**, 297–298 (2013).

305. Page, H., Flood, P. & Reynaud, E. G. Three-dimensional tissue cultures: current trends and beyond. *Cell Tissue Res.* **352**, 123–31 (2013).

306. Behravesh, E., Yasko, a. W., Engel, P. S. & Mikos, a. G. Synthetic Biodegradable Polymers for Orthopaedic Applications. *Clin. Orthop. Relat. Res.* **367**, S118–S129 (1999).

307. Wang, X. Overview on Biocompatibilities of Implantable Biomaterials. in *Advances in Biomaterials Science and Applications in Biomedicine* 112–154 (2013). doi:http://dx.doi.org/10.5772/53461.

308. Sittinger, M. *et al.* Tissue engineering and autologous transplant formation: practical approaches with resorbable biomaterials and new cell culture techniques. *Biomaterials* **17**, 237–242 (1996).

309. Meinel, L. *et al.* The inflammatory responses to silk films in vitro and in vivo. *Biomaterials* **26**, 147–155 (2005).

310. Torres, F. G., Commeaux, S. & Troncoso, O. P. Biocompatibility of bacterial cellulose based biomaterials. *J. Funct. Biomater.* **3**, 864–78 (2012).

311. Xiao, X. *et al.* The promotion of angiogenesis induced by three-dimensional porous beta-tricalcium phosphate scaffold with different interconnection sizes via activation of PI3K/Akt pathways. *Sci. Rep.* **5**, 9409 (2015).

312. Cancedda, R., Giannoni, P. & Mastrogiacomo, M. A tissue engineering approach to bone repair in large animal models and in clinical practice. *Biomaterials* **28**, 4240–50 (2007).

313. Feng, B. *et al.* The effect of pore size on tissue ingrowth and neovascularization in porous bioceramics of controlled architecture *in vivo*. *Biomed. Mater.* **6**, 015007 (2011).

314. Santerre, J. P., Woodhouse, K., Laroche, G. & Labow, R. S. Understanding the biodegradation of polyurethanes: From classical implants to tissue engineering materials. *Biomaterials* **26**, 7457–7470 (2005).

315. Kim, M. S. *et al.* An in vivo study of the host tissue response to subcutaneous implantation of PLGA- and/or porcine small intestinal submucosa-based scaffolds. *Biomaterials* **28**, 5137–43 (2007).

316. Andrade, F. *et al.* Studies on the biocompatibility of bacterial cellulose. *J. Bioact. Compat. Polym.* **28**, 97–112 (2012).

317. Straley, K. S., Foo, C. W. P. & Heilshorn, S. C. Biomaterial Design Strategies for the Treatment of Spinal Cord Injuries. *J. Neurotrauma* **27**, 1–19 (2009).

318. Dowell-Mesfin, N. M. *et al.* Topographically modified surfaces affect orientation and growth of hippocampal neurons. *J. Neural Eng.* **1**, 78–90 (2004).

319. Kim, M.-H. H., Park, M., Kang, K. & Choi, I. S. Neurons on nanometric topographies: insights into neuronal behaviors in vitro. *Biomater. Sci.* **2**, 148–155 (2014).

320. Theodore, N. *et al.* First human implantation of a bioresorbable polymer scaffold for acute traumatic spinal cord injury: A clinical pilot study for safety and feasibility. *Neurosurgery* **79**, E305–E312 (2016).

321. Yang, B. *et al.* Strategies and prospects of effective neural circuits reconstruction after spinal cord injury. *Cell Death Dis.* **15**, 1–14 (2020).

322. Ashammakhi, N. *et al.* Regenerative Therapies for Spinal Cord Injury. **25**, 471–491 (2019).

323. Zhou, P. *et al.* Cell Therapeutic Strategies for Spinal Cord Injury. *Adv. Wound Care* **8**, 585–605 (2019).

324. Moore, M. J. *et al.* Multiple-channel scaffolds to promote spinal cord axon regeneration. *Biomaterials* **27**, 419–429 (2006).

325. Stokols, S. & Tuszynski, M. H. Freeze-dried agarose scaffolds with uniaxial channels stimulate and guide linear axonal growth following spinal cord injury. *Biomaterials* **27**, 443–451 (2006).

326. Jiang, J. P. *et al.* Three-dimensional bioprinting collagen/silk fibroin scaffold combined with neural stem cells promotes nerve regeneration after spinal cord injury. *Neural Regen. Res.* **15**, 959–968 (2020).

327. Waldron, K. W. & Selvendran, R. R. Composition of the cell walls of different asparagus (Asparagus officinalis) tissues. *Physiol. Plant.* **80**, 568–575 (1990).

328. Lenehan, B. *et al.* Demographics of acute admissions to a National Spinal Injuries Unit. *Eur. Spine J.* **18**, 938–942 (2009).

329. McDonald, J. W., Becker, D. & Huettner, J. *Spinal Cord Injury*. *Handbook of Stem Cells* vol. 2 (Elsevier Inc., 2013).

330. Partyka, P. P. *et al.* Harnessing neurovascular interaction to guide axon growth. *Sci. Rep.* **9**, 1–10 (2019).

331. De Laporte, L., Lei Yan, A. & Shea, L. D. Local gene delivery from ECM-coated poly(lactide-co-glycolide) multiple channel bridges after spinal cord injury. *Biomaterials* **30**, 2361–2368 (2009).

332. Tsintou, M., Dalamagkas, K., Seifalian, A. M. & Seifalian, M. A. Advances in regenerative therapies for spinal cord injury: a biomaterials approach. *Neural Regen. Res.* **10**, 726–742 (2015).

333. Mothe, A. J., Tam, R. Y., Zahir, T., Tator, C. H. & Shoichet, M. S. Repair of the injured spinal cord by transplantation of neural stem cells in a hyaluronan-based hydrogel. *Biomaterials* **34**, 3775–3783 (2013).

334. Slotkin, J. R. *et al.* Biodegradable scaffolds promote tissue remodeling and functional improvement in non-human primates with acute spinal cord injury. *Biomaterials* **123**, 63–76 (2017).

335. Warburton, A., Girdler, S. J., Mikhail, C. M., Ahn, A. & Cho, S. K. Biomaterials in Spinal Implants: A Review. *Neurospine* **13**, 1–10 (2019).

336. Ruzicka, J. *et al.* The Effect of iPS-Derived Neural Progenitors Seeded on Laminin-Coated pHEMA-MOETACl Hydrogel with Dual Porosity in a Rat Model of Chronic Spinal Cord Injury. *Cell Transplant.* **28**, 400–412 (2019).

337. S, H. *et al.* Human Placenta-Derived Mesenchymal Stem Cells Loaded on Linear Ordered Collagen Scaffold Improves Functional Recovery After Completely Transected Spinal Cord Injury in Canine. *Sci. China. Life Sci.* **61**, (2018).

338. W, Y. *et al.* Taxol-modified Collagen Scaffold Implantation Promotes Functional Recovery After Long-Distance Spinal Cord Complete Transection in Canines. *Biomater. Sci.* **6**, (2018).

339. Basso, D. M., Beattie, M. S. & Bresnahan, J. C. A Sensitive and Reliable Locomotor Rating Scale for Open Field Testing in Rats. *J. Neurotrauma* **12**, 1–21 (1995).

340. Saxena, T., Gilbert, J., Stelzner, D. & Hasenwinkel, J. Mechanical characterization of the injured spinal cord after lateral spinal hemisection injury in the rat. *J. Neurotrauma* **29**, 1747–1757 (2012).

341. Silva, N. A., Sousa, N., Reis, R. L. & Salgdo, A. From basics to clinical : A comprehensive review on spinal cord injury. *Prog. Neurobiol.* **114**, 25–57 (2014).

342. Cripps, R. A. *et al.* A global map for traumatic spinal cord injury epidemiology: Towards a living data repository for injury prevention. *Spinal Cord* **49**, 493–501 (2011).

343. Anderson, M. A. *et al.* Astrocyte scar formation aids CNS axon regeneration. *Nature* **532**, 195–200 (2016).

344. Hackett, A. R. & Lee, J. K. Understanding the NG2 glial scar after spinal cord injury. *Front. Neurol.* **7**, 1–10 (2016).

345. Yang, T., Dai, Y. J., Chen, G. & Cui, S. Sen. Dissecting the Dual Role of the Glial Scar and Scar-Forming Astrocytes in Spinal Cord Injury. *Front. Cell. Neurosci.* **14**, 1–14 (2020).

346. Hoffman-Kim, D., Mitchel, J. A. & Bellamkonda, R. V. Topography, cell response, and nerve regeneration. *Annu. Rev. Biomed. Eng.* **12**, 203–31 (2010).

347. Tsai, E. C., van Bendegem, R. L., Hwang, S. W. & Tator, C. H. A novel method for simultaneous anterograde and retrograde labeling of spinal cord motor tracts in the same animal. *J. Histochem. Cytochem.* **49**, 1111–1122 (2001).

348. Pakulska, M. M., Tator, C. H. & Shoichet, M. S. Local delivery of chondroitinase ABC with or without stromal cell-derived factor 1α promotes functional repair in the injured rat spinal cord. *Biomaterials* **134**, 13–21 (2017).

349. Pravincumar, P., Bader, D. L. & Knight, M. M. Viscoelastic cell mechanics and actin remodelling are dependent on the rate of applied pressure. *PLoS One* **7**, e43938 (2012).

350. Ziemba, A. M. & Gilbert, R. J. Biomaterials for local, controlled drug delivery to the injured spinal cord. *Front. Pharmacol.* **8**, 1–20 (2017).

351. Badhiwala, J. H., Ahuja, C. S. & Fehlings, M. G. Time is spine: A review of translational advances in spinal cord injury. *J. Neurosurg. Spine* **30**, 1–18 (2019).

352. Ganz, J. *et al.* Implantation of 3D Constructs Embedded with Oral Mucosa-Derived Cells Induces Functional Recovery in Rats with Complete Spinal Cord Transection. *Front. Neurosci.* **11**, 589 (2017).

353. B, X. *et al.* A Dual Functional Scaffold Tethered With EGFR Antibody Promotes Neural Stem Cell Retention and Neuronal Differentiation for Spinal Cord Injury Repair. *Adv. Healthc. Mater.* **6**, (2017).

354. Tamosaityte, S. *et al.* Biochemical Monitoring of Spinal Cord Injury by FT-IR Spectroscopy—Effects of Therapeutic Alginate Implant in Rat Models. *PLoS One* **10**, e0142660 (2015).

355. Pakulska, M. M., Vulic, K. & Shoichet, M. S. Affinity-based release of chondroitinase ABC from a modified methylcellulose hydrogel. *J. Control. Release* **171**, 11–16 (2013).

356. Wang, Y., Dominko, T. & Weathers, P. J. Using decellularized grafted leaves as tissue engineering scaffolds for mammalian cells. *Vitr. Cell. Dev. Biol. - Plant 2020* 1–10 (2020) doi:10.1007/S11627-020-10077-W.

357. Porzionato, A. *et al.* Tissue-engineered grafts from human decellularized extracellular matrices: A systematic review and future perspectives. *Int. J. Mol. Sci.* **19**, (2018).

358. Gilpin, A. & Yang, Y. Decellularization Strategies for Regenerative Medicine: From Processing Techniques to Applications. *Biomed Res. Int.* **2017**, (2017).

359. Oraiopoulou, M. E. *et al.* In Vitro/In silico study on the role of doubling time heterogeneity among primary glioblastoma cell lines. *Biomed Res. Int.* **2017**, (2017).

360. Lacombe, J., Harris, A. F., Zenhausern, R., Karsunsky, S. & Zenhausern, F. Plant-Based Scaffolds

Modify Cellular Response to Drug and Radiation Exposure Compared to Standard Cell Culture Models. *Front. Bioeng. Biotechnol.* **8**, 1–15 (2020).

361. Veneruso, V. *et al.* Stem cell paracrine effect and delivery strategies for spinal cord injury regeneration. *J. Control. Release* **300**, 141–153 (2019).

362. Vismara, I., Papa, S., Rossi, F., Forloni, G. & Veglianese, P. Current Options for Cell Therapy in Spinal Cord Injury. *Trends Mol. Med.* **23**, 831–849 (2017).

363. Kumamaru, H. *et al.* Generation and post-injury integration of human spinal cord neural stem cells. *Nat. Methods* **15**, 723–731 (2018).

364. Rosenzweig, E. S. *et al.* Restorative effects of human neural stem cell grafts on the primate spinal cord. *Nat. Med.* **24**, 484–490 (2018).

365. Gong, Z. *et al.* Stem Cell Transplantation: A Promising Therapy for Spinal Cord Injury. *Curr. Stem Cell Res. Ther.* **15**, 321–331 (2019).

366. Shao, A., Tu, S., Lu, J. & Zhang, J. Crosstalk between stem cell and spinal cord injury: Pathophysiology and treatment strategies. *Stem Cell Res. Ther.* **10**, 1–13 (2019).

367. Gao, F. *et al.* Mesenchymal stem cells and immunomodulation: Current status and future prospects. *Cell Death Dis.* **7**, (2016).

368. Hassani, S. N., Moradi, S., Taleahmad, S., Braun, T. & Baharvand, H. Transition of inner cell mass to embryonic stem cells: mechanisms, facts, and hypotheses. *Cell. Mol. Life Sci.* **76**, 873–892 (2019).

369. Deng, J., Zhang, Y., Xie, Y., Zhang, L. & Tang, P. Cell Transplantation for Spinal Cord Injury: Tumorigenicity of Induced Pluripotent Stem Cell-Derived Neural Stem/Progenitor Cells. *Stem Cells Int.* **2018**, (2018).

370. Michelsen, K. A. *et al.* Area-specific reestablishment of damaged circuits in the adult cerebral cortex by cortical neurons derived from mouse embryonic stem cells. *Neuron* **85**, 982–997 (2015).

371. Trawczynski, M., Liu, G., David, B. T. & Fessler, R. G. Restoring Motor Neurons in Spinal Cord Injury With Induced Pluripotent Stem Cells. *Front. Cell. Neurosci.* **13**, (2019).

372. Lu, P. *et al.* Long-Distance Axonal Growth from Human Induced Pluripotent Stem Cells after Spinal Cord Injury. *Neuron* **83**, 789–796 (2014).

373. Fan, L. *et al.* Directing Induced Pluripotent Stem Cell Derived Neural Stem Cell Fate with a Three-Dimensional Biomimetic Hydrogel for Spinal Cord Injury Repair. *ACS Appl. Mater. Interfaces* **10**, 17742–17755 (2018).

374. Yao, R. *et al.* Olfactory Ensheathing Cells for Spinal Cord Injury: Sniffing Out the Issues. *Cell Transplant.* **27**, 879–889 (2018).

375. Delarue, Q. *et al.* Inhibition of ADAMTS-4 Expression in Olfactory Ensheathing Cells Enhances Recovery after Transplantation within Spinal Cord Injury. *J. Neurotrauma* **37**, 507–516 (2020).

376. Wright, A. A. *et al.* Enhancing the Therapeutic Potential of Olfactory Ensheathing Cells in Spinal Cord Repair Using Neurotrophins. *Cell Transplant.* **27**, 867–878 (2018).

377. Keefe, K. M., Sheikh, I. S. & Smith, G. M. Targeting neurotrophins to specific populations of neurons: NGF, BDNF, and NT-3 and their relevance for treatment of spinal cord injury. *Int. J. Mol. Sci.* **18**, 1–17 (2017).

378. Xu, D. *et al.* Efficient Delivery of Nerve Growth Factors to the Central Nervous System for Neural Regeneration. *Adv. Mater.* **31**, 1–8 (2019).

379. Rosich, K., Hanna, B. F., Ibrahim, R. K., Hellenbrand, D. J. & Hanna, A. The Effects of Glial Cell Line-Derived Neurotrophic Factor after Spinal Cord Injury. *J. Neurotrauma* **34**, 3311–3325 (2017).

380. Zhou, Y., Wang, Z., Li, J., Li, X. & Xiao, J. Fibroblast growth factors in the management of spinal cord injury. *J. Cell. Mol. Med.* **22**, 25–37 (2018).

381. Allahdadi, K. J. *et al.* IGF-1 overexpression improves mesenchymal stem cell survival and promotes neurological recovery after spinal cord injury. *Stem Cell Res. Ther.* **10**, 1–14 (2019).

382. Ong, W., Pinese, C. & Chew, S. Y. Scaffold-mediated sequential drug/gene delivery to promote nerve regeneration and remyelination following traumatic nerve injuries. *Adv. Drug Deliv. Rev.* **149**–**150**, 19–48 (2019).

383. Nathan, M., PRIEST, Cate., Denham, J., D. Wirth III, E. & Lebkowski, J. Human Embryonic Stem Cell-Derived Oligodendrocyte Progenitor Cells: Preclinical Efficacy and Safety in Cervical Spinal Cord Injury. *Stem Cells Transl. Med.* (2017) doi:http://dx.doi.org/ 10.1002/sctm.17-0065 This.

384. David, G. *et al.* Traumatic and nontraumatic spinal cord injury: pathological insights from neuroimaging. *Nat. Rev. Neurol.* **15**, 718–731 (2019).

385. Blesch, A. & Tuszynski, M. H. Cellular GDNF delivery promotes growth of motor and dorsal column sensory axons after partial and complete spinal cord transections and induces remyelination. *J. Comp. Neurol.* **467**, 403–417 (2003).

386. Zhao, L.-R. *et al.* Human Bone Marrow Stem Cells Exhibit Neural Phenotypes and Ameliorate Neurological Deficits after Grafting into the Ischemic Brain of Rats. *Exp. Neurol.* **174**, 11–20 (2002).